A Structural Study of $BiFeO_3$ – $PbTiO_3$ Thin Films Deposited by Pulsed Laser Deposition

Faye Bygrave

Submitted in accordance with the requirements for the degree of
Doctor of Philosophy

The University of Leeds
Institute for Materials Research
School of Process, Environmental and Materials Engineering

September, 2011

The candidate confirms that the work submitted is her own and that appropriate credit has been given where reference has been made to the work of others.

To my four ladies

In memory of my Granny

“If it was easy everyone would do it”

Mum

Acknowledgements

Firstly I would like to express my deepest thanks to Prof. Andrew Bell for all the support, guidance and advice in all aspects of this project over the past four years. He has been invaluable throughout this whole endeavour, without him this work could never have been realised or have been such fun.

I would also like to thank Dr. Tim Comyn for all his support and encouraging words. This work would not have been possible if it were not for his technical expertise and efforts in the x-ray diffraction facility for the entire department. I have been very fortunate to work with the supervision of such outstanding and inspiring people.

I gratefully acknowledge Mr. John Harrington, Dr Richard Walshaw and Dr Michael Ward (LEMAS) for their guidance in performing electron microscopy. I would also like to thank EPSRC for their financial assistance, without this I would never have been able to carry out this research.

I would also like to acknowledge all the staff and students of the department. Whether they have fixed things at the drop of a hat, kept me on my toes, advised me or simply made me smile, it has been a pleasure to work with such great people. To mention a few who come to mind; Joy (and her warming smile), Mike, Craig and Gareth (for all the laughs and Tea Club), Tim and Adam (for keeping me on my toes from day one) and finally Diane and Rob (for finding things seemingly impossible to find and yet still smiling at the end of the day).

On a more personal note, I would like to thank Zeki for selflessly supporting me in this past year with constant encouragement and the patience of a saint while putting up with my never ending one-way conversations…..you were brilliant.

Finally I must acknowledge those who have been there from the very beginning, through all the ups and downs, without whose love and friendship this would never have been possible or anywhere near as enjoyable. Mum, Lauren and Barry you have been fabulous and words cannot possibly describe my gratitude (but don't think this means the end of the 8am phone calls Mum). I truly appreciate and thank you for all your love and support in so many ways.

To all of you, thank you.

Abstract

In recent years ferroelectric thin films have received an enormous amount of attention due to their potential use in electronic device applications. Bismuth ferrite lead titanate ($xBiFeO_3 – (1-x)PbTiO_3$) thin films are of special interest due to their multiferroic nature, exceptionally high tetragonality and high switchable polarization close to the morphotropic phase boundary.

This work encompasses an initial structural investigation into $xBiFeO_3 – (1-x)PbTiO_3$ thin films deposited onto $Pt/TiO_x/SiO_2/Si$ substrates by pulsed laser deposition. The effect of substrate orientation, film composition and film thickness are described as well as the growth mechanisms and interactions at the substrate – film interface.

The pulsed laser deposition conditions were optimized to produce crystalline stoichiometric films of tetragonal and mixed phase tetragonal – rhombohedral phases. The films structure and growth mechanisms were studied using x-ray diffraction, scanning electron microscopy and atomic force microscopy. It was found that the substrate orientation, film composition and film thickness determine the structural properties of the deposited film.

A critical film thickness of 290 nm was identified as the minimum for a piezoelectric response to be observed. The piezoelectric nature of the films was confirmed by piezoforce microscopy.

Transmission electron microscopy analysis revealed the occurrence of interdiffusion at the substrate – film interface between the platinum bottom electrode and bismuth from within the deposited film. A strontium ruthanate buffer layer was deposited by pulsed laser deposition which prevented the interdiffusion, however local diffusion with the $xBiFeO_3 – (1-x)PbTiO_3$ deposited film was still present.

Table of Content

List of Tables

List of Figures

List of Symbols and Abbreviations

PZT	Lead Zirconate Titanate
MPB	Morphotropic Phase Boundary
PLD	Pulsed Laser deposition
P	Polarization
σ	Surface Charge Density
ε_r	Relative Permittivity of a Dielectric
ε_o	Permittivity of Free Space
χ	Dielectric Susceptibility
E	Electric Field
C	Capacitance
ω	Angular Frequency
I	Current
I_c	In-phase Current
I_l	Loss Current
ε'	Real Permittivity
ε''	Imaginary Permittivity
T_c	Curie Point
P_r	Remnant Polarization
P_s	Saturation Polarization

E_c	Coercive Field
e	Strain
k	Electromechanical Coupling Factor
MO - CVD	Metal Organic Chemical Vapour Deposition
IPA	iso-propan-2-ol
SEM	Scanning Electron Microscopy
TEM	Transmission Electron Microscopy
FIB	Focussed Ion Beam
AFM	Atomic Force Microscopy
PFM	Piezoresponse Force microscopy

Chapter 1

Introduction

1.1. Background and Motivation

In recent years, ferroelectric thin films have received an enormous amount of attention due to their potential applications such as memory devices, sensors and signal processing. Memory device technology has so far focussed its attention on the commercially used lead zirconate titanate (PZT), however the levels of polarization achievable in PZT presents a problem in device scalability where further miniaturization is desired (Fujisaki, 2010). Over the past decade, materials that offer a higher switchable polarization compared to PZT have received interest due to their potential use as a scalable high density memory device (Dearaujo, 1995), (Wang, 2004).

Thin film multiferroic materials form another research area that has stimulated much scientific and technological interest in recent years, particularly those of the ferroelectric - ferromagnetic variety, which due to the somewhat mutually exclusive electronic state requirements for the two phenomenon, are rather rare (Fiebig, 2005), (Hill, 2000). Identifying materials in which the polarization and magnetization are strongly coupled at room temperature (whereby they can be strongly influenced by an applied field or the polarization by a magnetic field) would lead to developments in spintronic devices for sensing, data storage and signal processing.

One of the rare examples of a multiferroic material is bismuth ferrite ($BiFeO_3$), which has been studied extensively over the past decade as it is one of the most promising multiferroic materials showing both ferroelectricity and antiferromagnetic ordering at room temperature (Fedulov, 1964). In addition, $BiFeO_3$ has been reported to exhibit achievable polarization values a factor of two higher than PZT, which presents the potential for use in scalable memory devices to replace PZT (Wang, 2004).

Unfortunately bismuth ferrite has some disadvantages such as low resistivity, weak magnetoelectric effect and high coercive field, with the low resistivity of $BiFeO_3$ making the observation of the ferroelectric polarisation - electric field

hysteresis loop difficult (Cheng, 2003). In attempt to solve these problems, doping with various ions on both the B-site and A-site of the bismuth ferrite structure has been employed (Cheng, 2003b), (Zhu, 2006). Other perovskites have been introduced to bismuth ferrite to form solid solutions. Among these, lead titanate ($PbTiO_3$) appears to be a promising solution (Woodward, 2003), (Chen, 2010).

The solid solution of $BiFeO_3$ with $PbTiO_3$ is known as bismuth ferrite lead titanate ($xBiFeO_3$ – $((1-x)PbTiO_3$) which exhibits a morphotropic phase boundary between the rhombohedral R3c and tetragonal P4mm phase that forms at $x \sim 0.7$. $xBiFeO_3$ – $(1-x)PbTiO_3$ is of special interest due to its multiferroic nature and exceptionally high tetragonality (c/a ratio) of approximately 1.17 close to the morphotropic phase boundary (Zhu, 2008), (Bhattacharjee, 2007), (Sai Sunder, 1995), (Fedulov, 1964).

Switching across this morphotropic phase boundary (MPB) is of relevant interest as it offers the opportunity to exploit three different ferroic order parameters, with the rhombohedral form being antiferromagnetic, the tetragonal form being paramagnetic and both forms ferroelectric, all at room temperature.

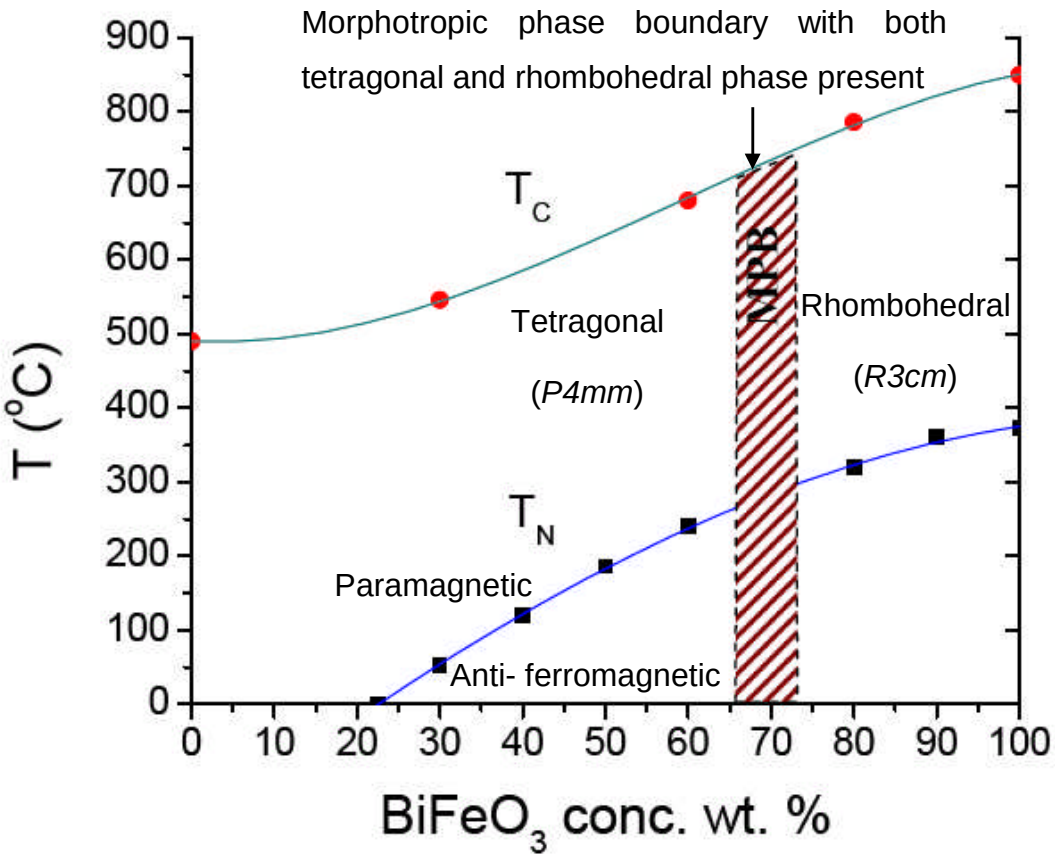

Figure. 1.1. Phase diagram for $xBiFeO_3$ – $(1-x)PbTiO_3$ sintered ceramic (Khan, 2008) presented by (Fedulov, 1964). (The width of the MPB is debatable; refer to page 39 for discussion).

At this phase boundary there is potential to electrically switch between the paramagnetic and antiferromagnetic forms via a field enforced transition between the tetragonal and rhombohedral phases. It is this potential phase switching across the rhombohedral - tetragonal phase boundary that cannot be achieved in pure $BiFeO_3$ and makes $xBiFeO_3$ – $(1-x)PbTiO_3$ compositions of great interest for research and device development.

$xBiFeO_3$ – $(1-x)PbTiO_3$ thin film research to date has centred around compositions lying within or close the MPB, due to the enhanced electrical properties shown in their bulk counterparts (Stevenson, 2010). Reported processing techniques include chemical solution deposition (Sakamoto, 2006), sol-gel synthesis (Lui, 2008) and pulsed laser deposition (Khan, 2007), (Chen, 2011). Of all the processing techniques, pulsed laser

deposition produces films with significant improvements in electrical properties with saturated polarization - electric field hysteresis loops for the $0.6BiFeO_3 – 0.4PbTiO_3$ compositions, exhibiting switchable polarizations up to 80 μCcm^{-2} in weakly textured films (Khan, 2007b). These values are comparable to epitaxial $BiFeO_3$ thin films which suggest the possibility of higher switchable polarization for highly orientated or epitaxial $BiFeO_3 – PbTiO_3$ films.

To exploit the multiferroic properties and high switchable polarization (required for memory device applications) that are seen in pulsed laser deposited $BiFeO_3 – PbTiO_3$ thin films, a greater understanding of film orientation and structure development is required, as the electrical and magnetic properties of ferroelectric thin films are directly linked to the degree of film orientation and overall structural properties.

1.2. Aims and Objectives

To investigate:

- Growth mechanisms of $BiFeO_3$ – $PbTiO_3$ thin films on $Pt/TiO_x/SiO_2/Si$ substrates.
- The effect of substrate orientation on structural and resulting electrical properties of $BiFeO_3$ – $PbTiO_3$ thin films.
- The effect of composition on the structural properties of $BiFeO_3$ – $PbTiO_3$ thin films.
- The effect of film thickness on structural and resulting electrical properties of $BiFeO_3$ – $PbTiO_3$ thin films.
- Any possible interactions at the film - substrate interface.

This work reports on the pulsed laser deposition of $xBiFeO_3$ – $(1-x)PbTiO_3$, where x = 0.7 and 0.6, thin films either side of the reported MPB (due to their enhanced electrically properties shown in their bulk counterpart). The films are deposited on preferentially oriented as well as (111) orientated $Pt/TiO_x/SiO_2/Si$ substrates due to their potential use in commercial memory storage devices. This allows the structural relationship between substrate and deposited film to be explored in greater depth with a view to tailoring electrical properties through controlled structure.

1.3. Structure of Thesis

This thesis is divided into eight chapters:

1. Introduction

2. Basic Concepts -
   An overview of basic concepts that are used throughout the thesis including crystal structure, electrical properties, thin film preparation techniques and ferroelectric materials (including a detailed description of $BiFeO_3$ – $PbTiO_3$).

3. Experimental Procedures -
   A detailed description of all processing techniques used throught the thesis including pulsed laser deposition, substrate preparation and target processing. All characterisation and sample preparation techniques are discussed in detail.

4. Optimisation of Pulsed Laser Deposition Conditions for $BiFeO_3$ – $PbTiO_3$ Thin Films on PtSi Substrates -
   Literature relating to $BiFeO_3$ – $PbTiO_3$ thin films as well as film structure as a result of varied pulsed laser deposition conditions are reviewed. The chapter also analyses the effect of varying pulsed laser deposition conditions on film structure and morphology, with a description of the optimum pulsed laser deposition processing conditions for $BiFeO_3$ – $PbTiO_3$ thin films on PtSi substrates.

5. Characterisation as a Function of Film Thickness, Substrate Type and Composition of $BiFeO_3$ – $PbTiO_3$ Films on Polycrystalline and (111) Orientated PtSi Substrates –
   Literature relating to the effect of varying film thickness, film composition and substrate type is described for different ferroelectric materials. Analysis is carried out to determine the film properties as a function of film thickness, substrate type and composition of $BiFeO_3$ –

$PbTiO_3$ thin films on polycrystalline and (111) orientated PtSi substrates.

6. $SrRuO_3$ Interdiffusion Barrier Layer –
   This chapter is a result of interdiffusion that was found to occur at the substrate – film interface of $BiFeO_3$ – $PbTiO_3$ thin films on PtSi substrates.
   The chapter describes literature relating to strontium ruthenate buffer layers in ferroelectric thin film systems. Analysis is carried out to analyse the use of strontium ruthenate buffer layers to prevent the interdiffusion that occurs at the substrate – film interface of $BiFeO_3$ – $PbTiO_3$ thin films on PtSi substrates.

7. Summary and Conclusions

8. Future Work

1.4. References

BHATTACHARJEE, S., S. TRIPATHI, D. PANDEY. (2007). Morphotropic phase boundary in (1-x)BiFeO3 – xPbTiO3: phase coexistanence region and unusually large tetragonality. *Appl. Phys. Lett*. **91**, pp.042903-1

CHEN, L., W. REN, W. ZHU, Z. G. YE, P. SHI, et al. (2010). Improved dielectric and ferroelectric properties in Ti-doped $BiFeO_3$-$PbTiO_3$ thin films prepared by pulsed laser deposition. *Thin. Solid. Films.* **518**(6), pp.1637-1640.

CHEN, L., W. REN, W. ZHU, Z. G. YE, P. SHI, et al. (2011). Structural, dielectric and ferroelectric properties of Ti-modified $0.72BiFeO_3$ - $0.28PbTiO_3$ thin films prepared by pulsed laser deposition. *Ferroelectrics.* **410**(1), pp.42-49.

CHENG, J., N. LI, L .E. CROSS. (2003). Structural and dielectric properties of Ga-modified BiFeO3 – PbTiO3 crystalline solutions. *J. Appl. Phys*. **94**(8), pp. 5153-5157.

CHENG, J., L .E. CROSS. (2003b). Effects of La substitution on ferroelectric rhombohedral/tetragonal morphotropic phase boundary in (1-x)(Bi,La)$(Ga_{0.05}Fe_{0.95})O_3$ – $xPbTiO_3$ piezoelectric ceramics. *J. Appl. Phys*. **94**(8), pp. 5188-5191.

DEARAUJO, C. A. P., J. D. CUCHIARO, L. D. MCMILLAN, M. C. SCOTT, J. F. SCOTT. (1995). Fatigue-free ferroelectric capacitors with platinum electrodes. *Nature.* **347**(13), pp.627-629.

FEDULOV, S. A., P. B. LADYZHINSKII, I. L. PYATGORSKAYA, Y. N. VENEVTSEV. (1964). Complete phase diagram of the PbTiO3 – BiFeO3 system. *Sov. Phys. Solid State*. 6, pp.375-378.

FIEBIG. M. (2005). Review of the magnetoelectric effect. *J. Phys. D: Phys.* **38**, pp.R123-R152.

FUJISAKI, Y. (2010). Current status of non-volatile semiconductor memory technology. *Jpn. J. Appl. Phys.* **49**, pp.100001-100014.

HILL, N. A., (2000). Why are there so few magnetic ferroelectrics?. *J. Phys. Chem. B.* **104**, pp.6694-6709.

KHAN, M. A. (2008). *Preparation and properties of bismuth ferrite lead titanate thin films prepared by pulsed laser deposition*. PhD thesis, University of Leeds.

KHAN, M. A., T. P. COMYN, A. J. BELL. (2007). Ferroelectric $BiFeO_3$-$PbTiO_3$ thin films on Pt/Si substrates. *Ultrasonics, Ferroelectrics and Frequency Control, IEEE Transactions.* **54**, pp.2583.

KHAN, M.A., T. P. COMYN, A. J. BELL. (2007b). Large remanent polarization in ferroelectric $BiFeO_3$-$PbTiO_3$ thin films on Pt/Si substrates. *Appl. Phys. Lett.* **91**(3), pp.032901.

LUI, H., Y. SUN, X. WANG. (2008). Study of the electrical properties of $PbTiO_3$- $BiFeO_3$ multilayer film structure. *J. Phys. D.* **41**, pp.095302-095307

SAI SUNDER, V. V. S. S., D. HALLIYAL, A. M. UMARJI. (1995). Investigation of tetragonal distortion in the $BiFeO_3$ – $PbTiO_3$ system by high temperature X-ray diffraction. *J. Mater. Res*. **10**(5), pp. 1301-1306.

SAKAMOTO, W., A. IWATA, T. YOGO. (2009). Electrical and magnetic properties of Mn-doped $0.7BiFeO_3$ – $0.3PbTiO_3$ thin films prepared under various heating atmospheres. *Mater. Chem. Phys.* **116**(2-3), pp.536-541.

STEVENSON, T. J. (2010). *Magnetic and electric properties of bismuth ferrite lead titanate ceramics*. PhD thesis, University of Leeds, (White Rose eThesis).

WANG, J., H. ZHENG, Z. MA, S. PRASERTCHOUNG, M. WUTTIG, R. DROOPAD, J. YU, K. EISENBEISER, R. RAMESH. (2004). Epitaxial $BiFeO_3$ thin films on Si. *Appl. Phys. Lett.* **85**(13), pp.2574-2576.

WOODWARD, D. I., I. M. REANEY, R .E. EITEL, C. A. RANDALL. (1995). Crystal and domain structure of the BiFeO3 – PbTiO3 solid solution. *J. Appl. Phys*. **94**(5), pp. 3313-3318.

ZHU, W. M., Z .G. YE. (2006). Improved dielectric and ferroelectric properties of high Curie temperature (1-x)BiFeO3 – xPbTiO3 ceramics by aliovalent ionic substitution. *Appl. Phys. Lett*. **89**(23), pp. 232904-/1-3.

Chapter 2

Basic Concepts

This chapter provides an overview of the basic concepts relating to ferroelectric thin film materials. This includes a description of crystal structure, electrical properties, thin film preparation techniques as well as ferroelectric materials (including a detailed description of the bismuth ferrite lead titanate solid solution). The literature relating to specific areas of research covered in this thesis (for example the effect of varying film thickness of ferroelectric thin films) is not discussed in this chapter, instead it can be found at the beginning of the relevant chapters.

2.1. Crystal Structures

A crystalline solid is a solid material where the atoms, molecules or ions are arranged in an orderly repeating pattern which exhibit long range order and symmetry. Patterns are identified from points within a lattice which are repeated. The points can be thought of as the corner points of vectors of prisms known as unit cells (Hammond, 2009). The dimensions and angles of these prisms and are known as lattice parameters, all of which can be described in terms of its unit cell.

2.1.1. Unit Cells

It is the crystal structure and symmetry that play an important role in determining the physical properties of a material, both of which can be described in terms of its unit cell. The unit cell contains one or more atoms arranged within the box structure with a three dimensional shape. All crystal structures (orderly repeating unit cells) can be divided into 7 lattice symmetries according to their cell dimensions or lattice vectors a, b, c and the angles between them α, β, γ:

- Triclinic
- Monoclinic
- Orthorhombic
- Rhombohedral
- Tetragonal
- Hexagonal
- Cubic

However the lattice points inside the unit cell vary for different structures and these atomic positions are measured from the corner lattice point *x, y, z*. which involve a body-centred atom, face-centred atom or base centred atom. (Hammond, 2009)

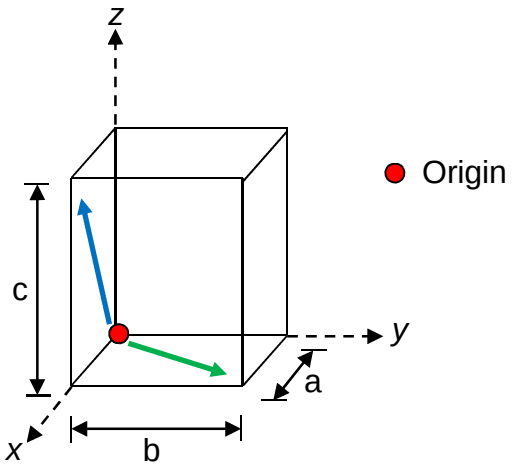

Figure. 2.1. Schematic of the unit cell with cell dimensions (a, b, c), origin point and the directions (*x, y, z)*. When the 7 crystal systems are combined with the various atomic positions all crystal structures can be catagorised as one of the 14 Bravais Lattices. (Ladd, 2003) (Hammond, 2009)

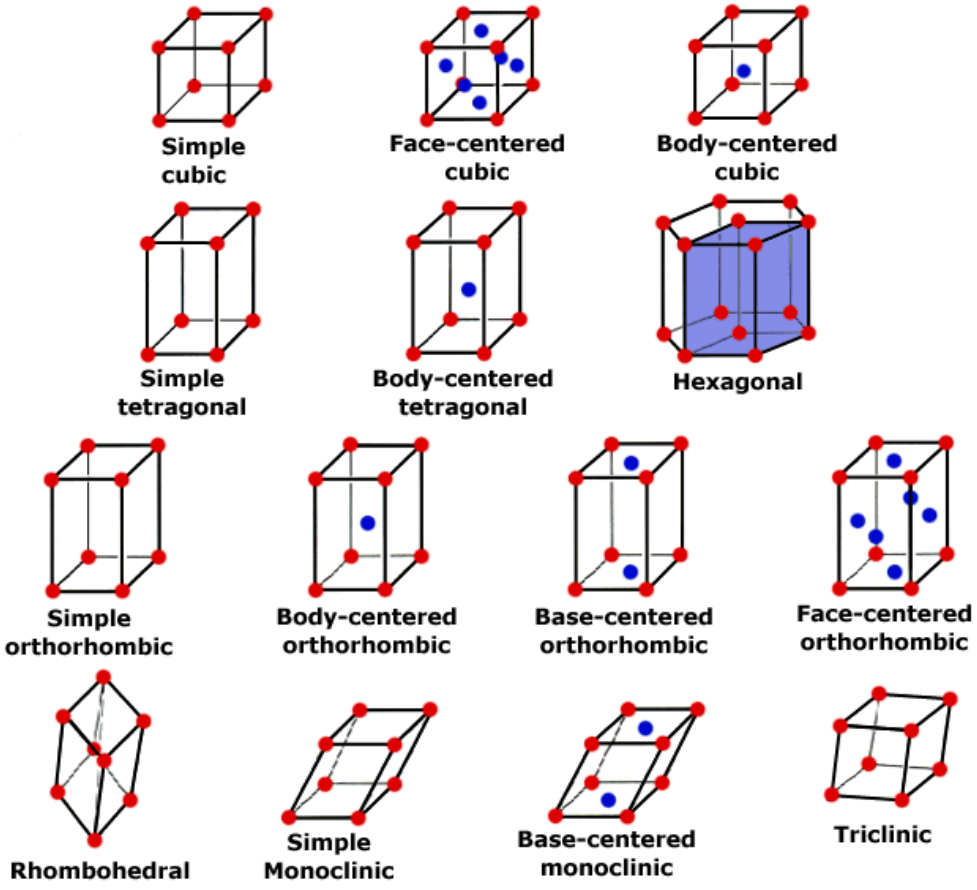

Figure. 2.2. The 14 Bravais Lattices (taken from Penn Engineering, 2011)

2.1.2. Space Groups

A crystal may have symmetries in the form of point symmetries which includes:

- Reflection
- Rotation
- Inversion
- Improper rotations

or a translation symmetry which includes:

- Pure translation
- Screw axis
- Glide Planes

Combining the possible symmetries and lattice parameters, all crystals can be described as one of the 230 possible space groups which provides a full description of the crystal structure (Hammond, 2009). To represent the symmetry elements in point groups the Hermann-Mauguin notation is commonly used (Hammond, 2009). The Herman-Maugin notation usually consists of four symbols describing the lattice type and the symmetry such as P4mm.

The first upper case letter describes the lattice type (Bravais Lattice in 3D)

P	Primitive
I	Body-centered
F	Face-centered
C	Base-centered
R	Rhombohedral

The screw axis is described by a number *n* where the angle of rotation is 360˚ / *n*. For example 180˚ (two-fold symmetry), *n* = 2.

The final symbols describes the crystal symmetry in more details.

R3c: Rhombohedral cell with three-fold rotation and a glide plane in the c-axis.

P4mm: Primitive cell with four-fold rotation and two mirror planes.

2.1.3. Crystallographic Planes and Directions

Materials properties and processes vary with direction within a crystal therefore it is useful to specify certain directions and planes within the crystal. This is especially true in thin films that may exhibit texture (refer to Section 2.1.4).

Figure. 2.3. A plane (left) and a direction (right) within the unit cell.

Directions and planes can be thought of as fictitious lines or planes linking points within the unit cell. They are described using three integers known as the Miller Indices expressed as planes (hkl) and directions [hkl]. The Miller Indices first require a defined point position specified in terms of it's coordinates as fractional multiples of a unit cell edge length and the reciprocal is then used.

In a cubic unit cell the [101] direction and the [110] direction are equivalent, however in tetragonal systems these would be different due to the c-axis and a-axis being different. A family of directions is described <hkl> for example:

<123> = [123], [213], [312], [132], [231], [321]

(hkl) describes a crystallographic plane and {hkl} is used to describe a family of crystallographic planes for example;

{hlk} = (hkl), (lhk), (hlk)

Firstly the intersection of the plane with the axis in terms of a, b and c needs to be determined and the reciprocal of that, defines the plane. (Cullity, 2001)

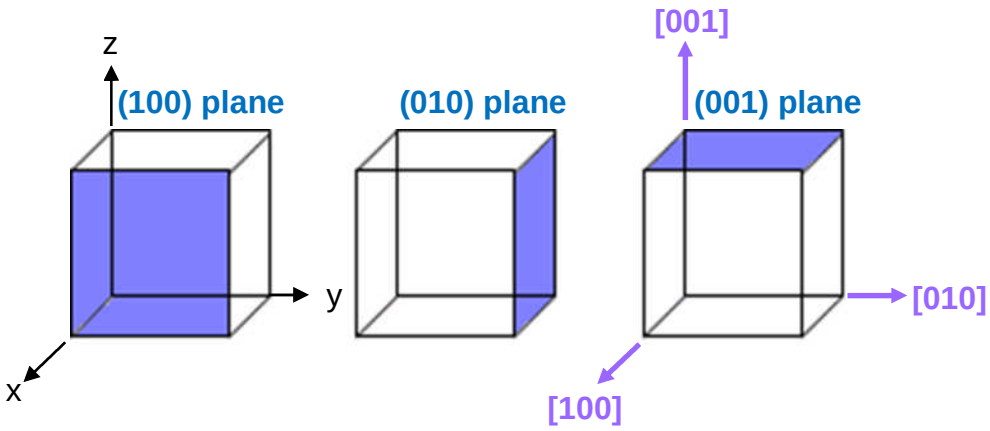

Figure. 2.4. {100} planes and <100> directions in a unit cell.

2.1.4. Orientation and Texture

An understanding of orientation and texture are important in the field of thin films to understand the structure of the deposited film and substrate as well as the structural relationship between the two.

Polycrystalline solids are composed of a collection of many small crystals (or grains). For many polycrystalline materials the crystallographic orientation of the individual grains are isotropic (Figure. 2.5) however in thin films this is rare, with the crystallographic direction [hkl] often found to be preferentially orientated with respect to the sample reference frame (Figure. 2.6). The anisotropy of crystalline orientation is known as texture or preferred orientation.

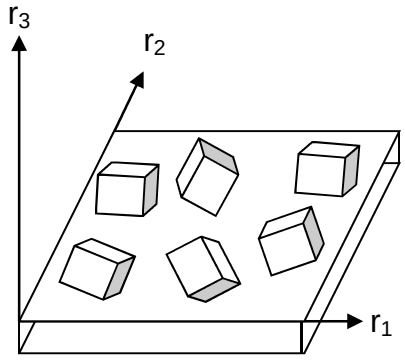

Figure. 2.5. Sample reference frame {r} and randomly distributed crystalline orientations (adapted from Birkholz, 2006).

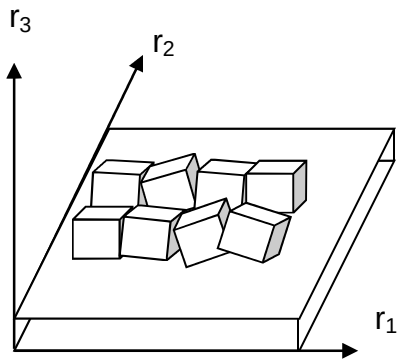

Figure. 2.6. Sample reference frame {r} and preferentially oriented grains.

However if all of the crystallites are orientated in the same direction, where the crystal lattice is continuous with no defects or grain boundaries it is described as a single crystal or epitaxial film.

For example if the (001) plane of each unit cell within the deposited film is perfectly parallel to the surface of the substrate, the deposited film is referred to as (001) orientated single crystal or (001) epitaxial (Figure. 2.7).

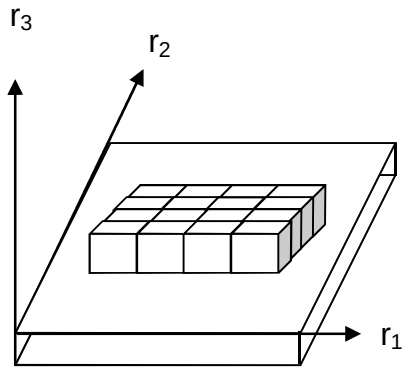

Figure. 2.7. Sample reference frame {r} and epitaxially oriented grains.

However if the (001) plane within each of the unit cells within the deposited film is *nearly* parallel to the surface of the substrate the film is referred to as (001) preferentially orientated (shown in Figure 2.6.)

Preferential orientation or epitaxy in films is usually achieved through controlled deposition conditions and / or hetroepitaxial growth whereby the atomic positions of the deposited film align with the underlying atomic positions of the substrates.

2.1.5. Perovskite Structure

The term perovskite was first used in the 19th century to describe the naturally occurring mineral $CaTiO_3$ (Mitchell, 2002). The term has subsequently been used to describe materials having the general formula ABX_3, where A and B are cations and X anions. In the perovskite structure the A cation and X anion form a close packed array of AX and XX rows. The B cations are located in the octahedral voids created by the X anions in the adjacent layers. Because this forms a cubic close packed structure within the layers, the structure can also be described as corner sharing BX_6 octahedra, with the A cation located in interstitial sites surrounded by eight octahedral. In an ideal case the perovskite structure crystallises with cubic symmetry in space group Pm_3m.

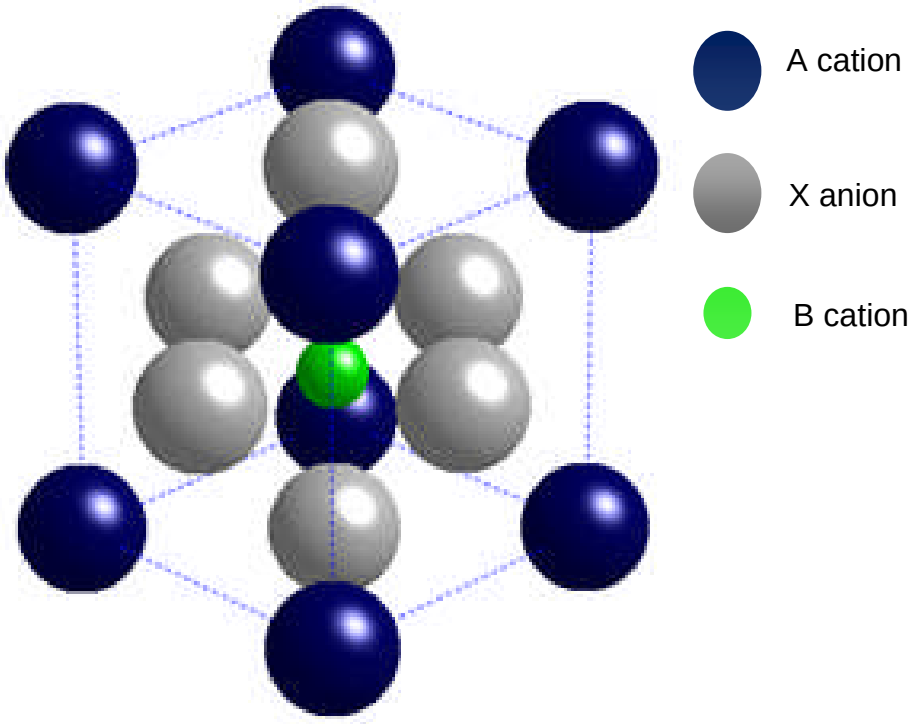

Figure. 2.7. The ideal cubic ABX_3 perovskite structure.

In the case of ferroelectrics (see section 2.2.3.) X is generally O^{2-} and is often quoted as ABO_3 however not all ABO_3 compounds crystallise as a perovskite structure.

There are several conditions which the ABO_3 perovskite must follow (Shannon, 1976):

- The negative charge of the anion must equal the sum of positive charge of the cations.
- O and A must be of similar ionic radii in order to fit into the close packed atomic array, such as bismuth and lead.
- The radius of the B ion = 0.414 of the radius of O ion. This will ensure the B ion fits into the octahedral voids.

Therefore it is usually the transitions metals that form the perovskite structure. $SrTiO_3$ is known as an ideal perovskite structure as it has cubic symmetry. In this ideal perovskite the a-axis of the unit cell can be related to the ionic radii (Mitchell, 2002):

$$\mathrm{a} = \sqrt{2}[R_A + R_O] = 2[R_B + R_O] \qquad \textit{Equation. 2.1.}$$

The ratio of the two expressions is referred to as the tolerance factor *t*.

$$t = \frac{[R_A + R_O]}{\sqrt{2}[R_B + R_O]} \qquad \textit{Equation. 2.2.}$$

The tolerance factor was proposed by Goldschmidt to determine the stability of a perovskite and should be equal to 1 for a specific assembly of ions where the ideal perovskite structure may form. However most perovskite structures are distorted and do not have cubic symmetry. Common distortions include the displacement of the cation and the tilting of the octahedra. These distortions have an effect on the symmetry and space group of a crystal lattice and therefore change the physical properties of the structure. If the B cation assumes a non-centrosymmetric position in relation to the A cation it often results in an electric dipole (polarization).

There are 32 crystal point groups (crystal classes), which are based on orientation repetition or symmetry within the crystal. Of these 32 crystal point

groups, 11 are centrosymmetric which are perfectly symmetrical and therefore non-polar. The remaining 21 crystal point groups are non-centrosymmetric and do not have a centre of symmetry. Of the 21 non-centrosymmetric crystal point groups, 10 posses a unique polar axis which exhibit spontaneous polarization in the direction of the polar axis (Moulson, 2003) (Hammond, 2009).

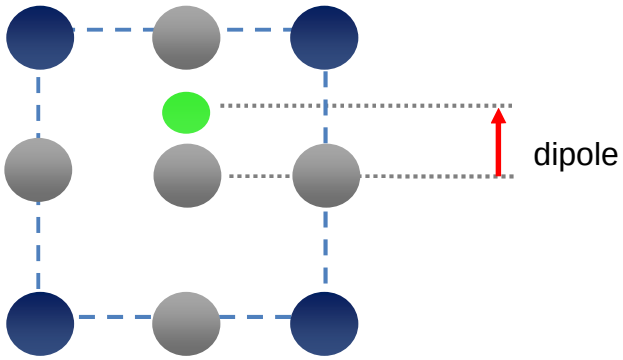

Figure. 2.8. [100] of the perovskite with B cation displacement resulting in an electric dipole.

An electric dipole within the perovskite structure is a property that is essential to ferroelectricity (refer to section 2.2.3).

Differing ionic radii of the ions within the perovskite structure can cause distortions in the form of octahedral tilting. For example the volume of the interstice will reduce to improve the structural stability when the A cation becomes too small.

The degree of distortion in a perovskite structure can be estimated from the tolerance factor. Goldschmidt calculated that a perovskite structure is stable between t = 0.77 ~ 0.99 (Goldschmidt, 1927). However Jaffe et al reports that the cubic perovskite structure is stable between t = 0.95 ~ 1.0, when t < 0.95 the perovskite structure is slightly distorted and not ferroelectric and when t > 1.0 the perovskite structure tends to become tetragonal (Jaffe, 1971).

When $t < 1.0$ the A cation is smaller than its cavity or the B cation is larger than its cavity, which generally results in a rhombohedral or monoclinic unit cell as a result of octahedral tilting. When $t > 1.0$ the A cation is larger than its atomic position or the B cation is smaller than its atomic position resulting in the elongation of the oxygen tetrahedra hence a tetragonally distorted unit cell. (Megaw, 1957)

2.2. Electrical Properties of Materials

2.2.1. Dielectrics

A polar structure or dipole moment is induced when the centre of the negative charge in a material is displaced relative to the centre of the positive charge. A structure may exhibit such displacements spontaneously (for example the perovskite structure) or may be induced by an applied electric field. A dielectric material can be described as a non-conductive material that exhibits or can be made to exhibit a polar state when subject to an applied electric field. In an ideal dielectric the polarization is linearly dependent on the applied field and is independent of temperature. Therefore on the removal of an applied electric field the polarization returns to zero.

There are four main polarization mechanisms by which a polar structure or dipole moment exists within a dielectric material: electronic, ionic, dipolar and space charge.

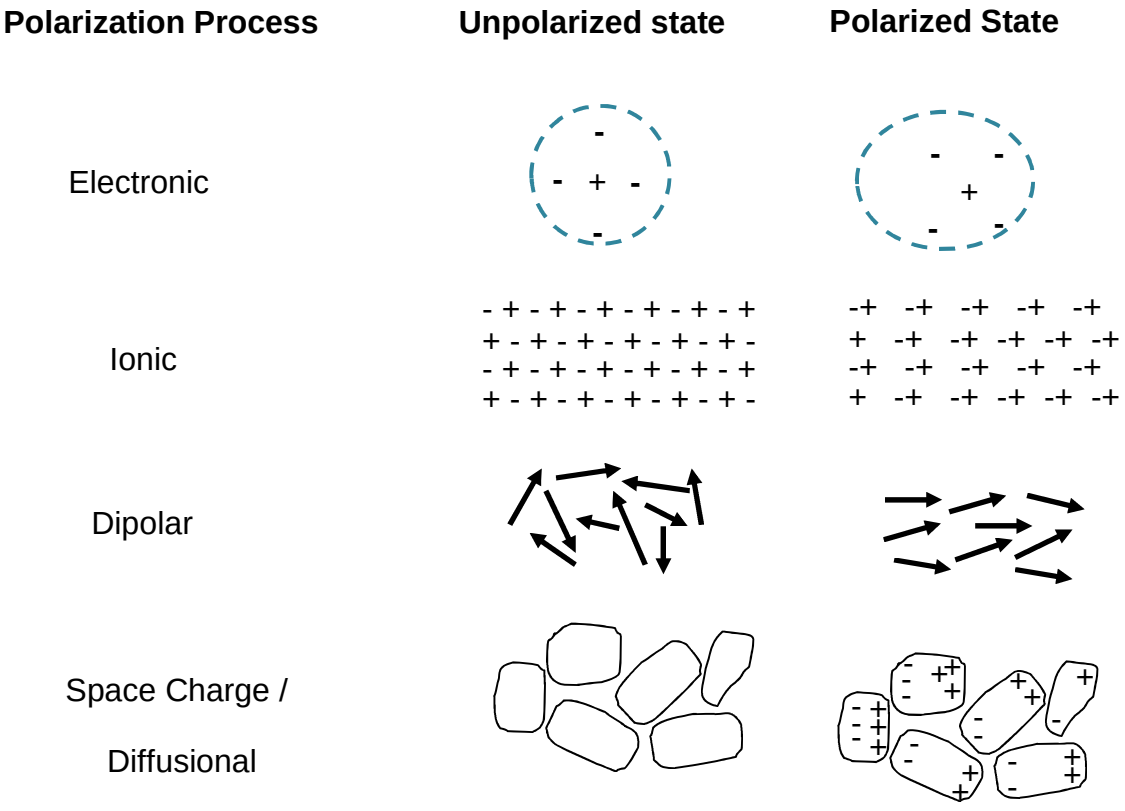

Figure. 2.9. Schematic of four different types of polarization, electronic, ionic and dipolar and space charge (adapted from Moulson, 2003).

Atomic polarization occurs in all materials whereby the electrons exhibit a small displacement within the atom relative to the nucleus on an applied electric field.

Ionic materials generate an additional polarization which involves the relative displacement of cations and anions. Again this is in the presence of an applied electric field (Moulson, 2003).

Dipolar polarization occurs when permanent dipoles are present in the material, however the permanent dipoles present no net charge. Once an electric field is applied, the dipole moments align, resulting in a polarized material (Moulson, 2003).

The polarization developed by a dielectric material in response to an applied electric field is referred to as dielectric behaviour.

Dielectrics are used extensively in capacitors, as their polarization behaviour enhances the charge storage capabilities when placed between the plates of a parallel plate capacitor. Faraday has shown that by placing a dielectric material in a field between two conducting layers, the dielectric material develops a dipole moment in response to the field. This induces a buildup of charge on the surface of the dielectric material. With the need to balance the charge, the conductive layers respond by the arrival of additional charges onto the surface of the conducting layers.

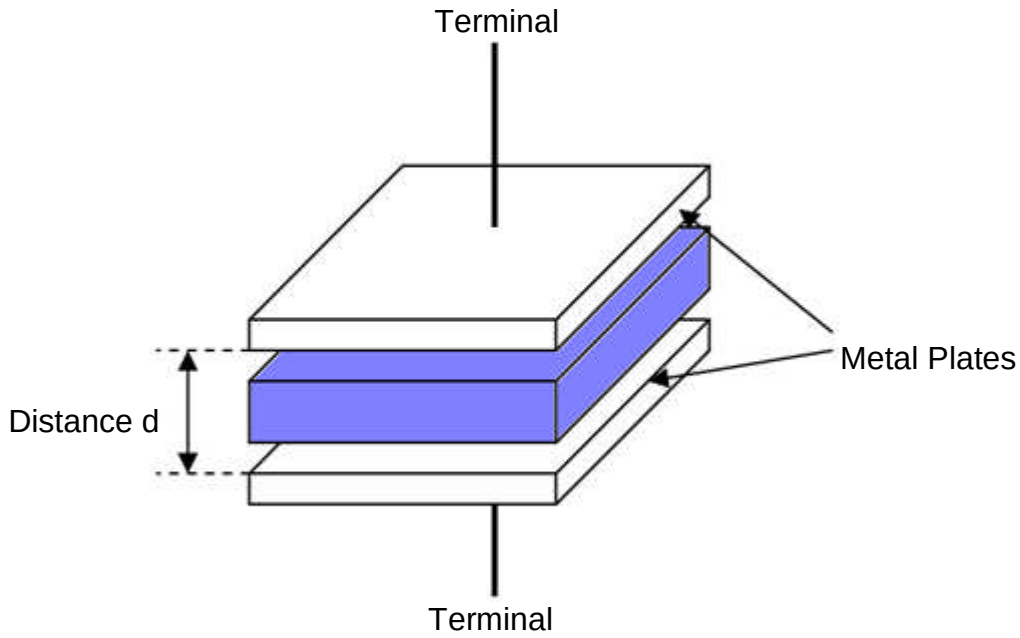

Figure. 2.10. A dielectric material used in a capacitor.

In the presence of a dielectric material the surface charge density on the conducting layers increases by a factor of ε_r, which is termed relative permittivity or dielectric constant. The electric polarization can then be defined as the measure of the increase in the surface charge density of the conductive layers and is given by the following equation:

$$P = \Delta\sigma = \varepsilon_r\varepsilon_o(V/\mathrm{d}) - \varepsilon_o(V/\mathrm{d}) = (\varepsilon_r - 1)\varepsilon_o(V/\mathrm{d}) = \chi\varepsilon_o(V/\mathrm{d}) = \chi\varepsilon_o\mathrm{E}$$

Equation. 2.3.

where:

P = polarization

χ = dielectric susceptibility

E = electric field.

d = separation between the plates

V = voltage across the plates

σ = surface charge density on the condenser plates

ε_r = relative permittivity of the dielectric

ε_o= permittivity of free space (8.85×10^{-12} F m^{-1})

For a capacitor of this type, with plates of area A and separation d, the capacitance C, is given by the following equation:

$$C = \varepsilon_o \varepsilon_r A / d$$ *Equation. 2.4.*

For a fixed value of capacitance, an increase in ε_r enables a decrease in A, hence materials with high ε_r enables miniaturization of capacitors.

2.2.2. Dielectric Loss

In an ideal dielectric the current is 90° out of phase with an applied sinusoidal alternating voltage. As the voltage charges up the capacitor, the current drops below zero. Once the capacitor releases its stored charge the voltage drops and the current reaches its maximum. However unlike an ideal dielectric a real dielectric is prone to losses due to dielectric absorption or resistive leakage, this is known as dielectric loss Moulson, 2003).

One way to describe the relationship between voltage and current is through phasor diagrams (Figure 2.11).

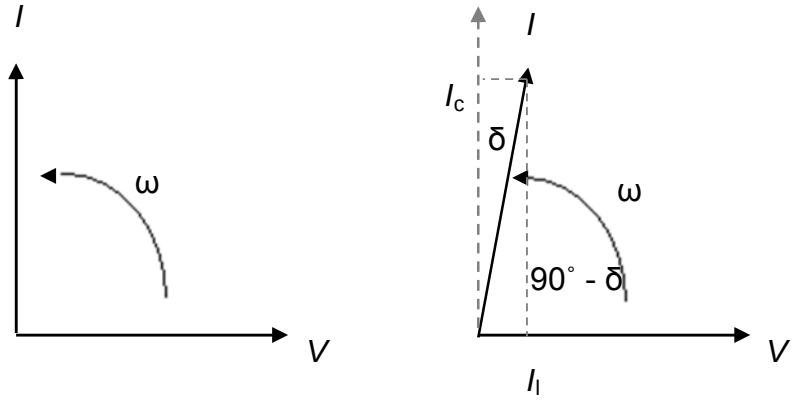

Figure 2.11. Phasor diagrams showing the behaviour of (a) an ideal dielectric with current 90° out of phase with voltage (b) real dielectric exhibiting a loss due to a non-ideal phase difference of (90° - δ) between current and voltage. (adapted from Moulson, 2003)

The power dissipation of a dielectric is averaged over time and is proportional to the dissipated factor / loss tangent which is expressed as tanδ. Therefore when tanδ = 0 the dielectric behaves as an ideal capacitor, however as tanδ approaches infinity the capacitor behaves as a resistor (Moulson, 2003).

In an ideal capacitor the current can be resolved into two components, I_c (which is in phase with the current) and I_l which is the loss current (in phase with the voltage). It is the loss current I_l that is responsible for the power loss and can be written.

$I_l = I \sin\delta = I_c \tan\delta$ *Equation. 2.5.*

The permittivity of a dielectric can also be resolved into two components (Moulson, 2003); real permittivity (ε') and imaginary permittivity (ε''), which can be written;

$\tan\delta = \varepsilon'' / \varepsilon'$ *Equation. 2.6.*

Thus as tanδ increases, the dielectric becomes more 'lossy'.

2.2.3. Ferroelectricity

A ferroelectric material posses a spontaneous electric polarization that can be reversed by the application of an external electric field (Jaffe, 1971). Of the 21 non-centosymmetric point groups, 10 posses a unique polar axis which exhibits spontaneous polarization. The internal electric dipoles of a ferroelectric material are coupled to the material's lattice so anything that changes the lattice structure will change the strength of the dipoles (change in the spontaneous polarization). Above a certain temperature, known as T_c, most ferroelectrics go through a phase transformation to a cubic state usually referred to as paraelectric.

2.2.3.1. Ferroelectric Domains

The original phase (above T_c) has a number of possible equivalent polarization directions. As the crystal passes through the Curie point it develops a polar structure in which the crystal partitions into regions of different polarization directions. These regions are called domains and the boundaries between them are referred to as domain walls. For example when a ferroelectric material transforms from a cubic paraelectric state to a

tetragonal ferroelectric state, 90° and 180° domains will form and when a cubic paraelectric phase transforms to a ferroelectric rhombohedral state, 109°, 71° and 180° domains will form.

Although domains are polar, the net polarization is zero until an electric field or stress is applied to orientate the domains in a specific polar direction, which is termed ‘poling’. A material can be ‘unpoled’ (randomize domain’s polar direction) with the application of stress or elevated temperatures Figure. 2.12. (Haertling, 1999) (Burfoot 1967)

2.2.3.2. Curie Point

The maximum temperature that a ferroelectric material displays spontaneous reversible electric polarization is defined by the Curie point (T_c). The Curie point (T_c) is the transition temperature above which the material no longer exhibits ferroelectric behavior and assumes a centrosymmetric point group. Above T_c the hysteresis loop (refer to Section 2.2.3.3) completely closes and the material becomes parelectric, losing its ferroelectric properties. (Moulson, 2003) (Haertling, 1999)

2.2.3.3. Ferroelectric Hysteresis Loop

The most prominent evidence of ferroelectric property’s is the existence of a polarization - electric field hysteresis loop (P-E loop) Figure 2.12. Prior to an applied electric field the macroscopic structure has no net overall spontaneous polarization. Once an electric field is applied to the ferroelectric material the electric dipoles in the domains begin to orientate in the direction of the applied electric field. Saturation in polarization is achieved at high fields and its magnitude is defined by the point $P_{s.}$ As the field is reversed the net polarization is reduced. When the applied field (E) is returned to zero there is a certain polarization that is retained by the structure which is termed remnant polarization P_r. To reduce the net polarization to zero a further decrease in applied electric field is required (into negative values) which is

termed coercive field E_c. Additional negative field will see the polarization saturation $-P_s$ and upon reversal of the field the hysteresis loop closes.

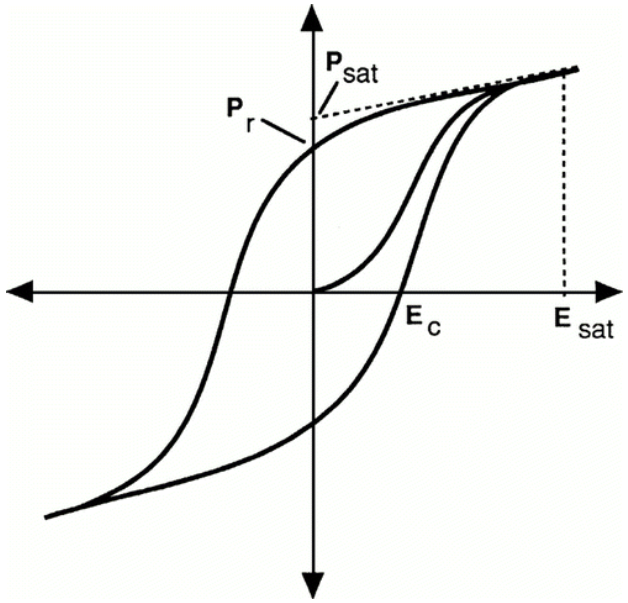

Figure. 2.12. A polarization - electric field hysteresis loop. (Polla, 1998)

2.2.4. Phase Transformations

Above T_c a ferroelectric material no longer displays spontaneous polarization as the structure becomes non-polar (therefore the material is no longer ferroelectric). Ferroelectrics remain polar until T_c and show an increase in the polarizability of the material until this point. As the temperature of the material is decreased further, many ferroelectric materials display several phase transitions. Providing these phase transitions are between one non-centrosymmetric phase and another, and display a unique polar axis, the material will remain ferroelectric despite the transformations in crystal symmetry. With a change in crystal symmetry come a change in the polar axis direction. This is best demonstrated through barium titanate, $BaTiO_3$ (refer to Section 2.3.1.).

2.2.5. Piezoelectricity

Piezoelectric materials can generate an electric polarization with the application of a mechanical stress or generate a strain with the application of an electric field.

When the application of a stress, (σ) causes the development of an electric polarization, *P*, it is termed the 'direct' piezoelectric effect with a simple linear relationship expressed by the following equation:

$$P = d\sigma \qquad \textit{Equation. 2.7.}$$

where *d* is the piezoelectric constant.

In an anisotropic piezoelectric crystal, a complex series of strains arise from an applied electric field in a particular direction. Therefore to fully express the relationship between the polarization and stress vectors, matrices containing several different *d* values are required.

d is expressed as a value with two subscripts, the first relating to the direction of the applied field and the second relating to the direction of the resultant displacement. In electroceramics, the two key values of *d* that are of most interest are the d_{33}, the piezoelectric constant linking longitudinal polarization with longitudinal stress, and the d_{31} linking longitudinal polarization with transverse stress.

When the application of an electric field, *E*, generates a proportional strain, *e*, it is referred to as the 'converse' piezoelectric effect (again relating to the piezoelectric constant *d*):

$$e = dE \qquad \textit{Equation. 2.8.}$$

All materials develop a strain when placed in an electric field which is termed electrostriction. Electrostriction differs from the converse piezoelectric effect

in that reversal of the field does not promote a change in the strain, hence *E* and *e* are not proportional in electrostriction. (Jaffe, 1971)

Another important quantity is the electromechanical coupling factor, *k*, which indicates the efficiency of the piezoelectric effect. It is defined as:

k^2 = electrical energy converted to mechanical energy/input electrical energy

or

k^2 = mechanical energy converted to electrical energy/input mechanical energy

The mechanical coupling factor is also subscribed as k_{33} and k_{31}, which refers to the longitudinal and transverse coupling efficiencies.

2.3. Comparison of Film Preparation Techniques

Deposition of ferroelectric thin films must satisfy certain criteria:

- device-compatibility with highly orientated polycrystalline or single crystalline films
- high density
- resistance to fatigue
- uniform thickness
- high reproducibility
- process must be simple, in-expensive as well as environmentally friendly

There are currently a wide variety of techniques being used for the preparation of ferroelectric thin films. Those which are most commonly used, such as the chemical solution method sol gel and physical deposition techniques such as metal-organic chemical vapour deposition (MO-CVD), physical vapour deposition (PVD) and pulsed laser deposition (PLD), are described in terms of the above criteria.

2.3.1. Sol-gel

The sol-gel process is a wet chemical technique whereby a precursor (which is usually a chemical solution or colloidal particles) (Paz de Araujo, 1996) consisting of one or more metal-organic compounds is prepared and hydrolyzed to obtain a solution with suitable viscosity for dip coating or spin coating.(Attica, 2002)

Once coated, the films are dried to evaporate off the organics from the films surface. This process is termed pyrolysis. Residual organic compounds of the gel are evaporated off via a crystallization heat treatment stage.

The advantages of thin films prepared by sol-gel synthesis are: the uniform thickness of the films, a cost-effective process as well as producing stoichiometric films.

2.3.2. Metal-Organic Chemical Vapour Deposition (MO-CVD)

The metal-organic chemical vapour deposition (MO-CVD) process is commonly used in the semiconductor industry to produce thin films (Paz de Araujo, 1996). The process typically involves one or more volatile precursors which react and/or decompose onto an exposed heated substrate to produce the desired deposit.

A thin film can be deposited by MO-CVD in various forms including: polycrystalline, amorphous and epitaxial.

MO-CVD allows stoichiometric thin films to be prepared with a high degree of uniformity over large substrate areas. Other advantages include high reproducibility of the films as well as layer by layer growth of films which allows epitaxial thin films to be prepared.

2.3.3. Pulsed Laser Deposition (PLD)

Pulsed laser deposition (PLD) is a physical vapour deposition (PVD) technique where a pulsed laser beam strikes the surface of the target material causing the outermost layers of the target material to rapidly heat up and evaporate off. The evaporated target material forms a high energy plume, which deposits onto the heated substrate.(Ohring, 2002) (Chrisey, 1994)

Usually the PLD chamber contains a computer controlled target holder which can hold several targets at one time. By positioning the congruent targets underneath the pulse laser, multilayer materials can easily be fabricated.

PLD offers advantages such as: dense films, low processing temperatures, a wide range of deposition rates, simple setup and operation procedure as well as high reproducibility.

Unfortunately PLD is limited to a small deposition area due to the narrow angular distribution of the plume which results in a non-stoichiometric film with non-uniform thickness. Another disadvantage of PLD is the splashing of

target material onto the substrate which will affect the growth of subsequent layers and eliminate/reduce the electrical properties of the film.

2.4. Ferroelectric Materials

2.4.1. Barium Titanate

During the 1940's materials that had previously shown dielectric anomalies were been tested for ferroelectric properties, which was driven by the need to develop ceramics with high permittivity's. Wul and Von Hippel published independent research on the properties of barium titanate ($BaTiO_3$) showing a ferroelectric hysteresis loop (Von Hippel, 1946) that revealed the presence of ferroelectricity in $BaTiO_3$ (Wul, 1945). Due to its mechanical and chemical stability at room temperature as well as it being ferroelectric at room temperature, it appeared the perfect material for several technological applications. The fabrication of $BaTiO_3$ also held advantages of being cheap and easy to fabricate.

To understand why $BaTiO_3$ displays ferroelectricity, its structure must be understood. $BaTiO_3$ is a perovskite structure which consist of arrays of corner-sharing TiO_6 on octahedra with Ba^{2+} ions in the large interstitial octahedral sites which are formed by the octahedral arrangement. Above T_c of ~ 130 ºC it has a cubic symmetry which is non-polar. On cooling through T_c the unit cell becomes tetragonal (Megaw, 1945) whereby the Ti^{4+} cations are displaced along the unique axis creating a dipole with polarization vector [001].

In 1949 Kay and Vousden showed two more phase transitions on cooling (Kay, 1949). At ~5 °C the tetragonal structure changes to orthorhombic whereby the polarization vector switches from [001] to [101] and at -90 °C the structure becomes rhombohedral whereby the polarization vector switches from [101] to [111] (Megaw, 1952).

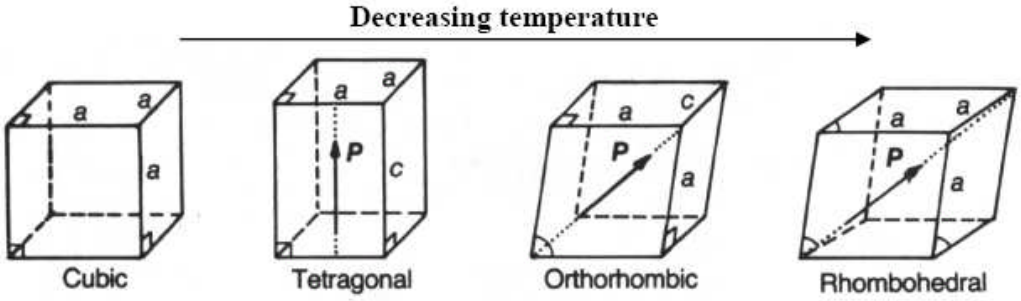

Figure. 2.13. Four structures of $BaTiO_3$, illustrating the distortions that occur at each phase transition and their effects on the shape on the unit cell and the polarization vector. (Moulson, 2003)

When $BaTiO_3$ undergoes a phase transition from cubic to tetragonal the unit cell can be distorted along any of the six cubic <001> directions. In the orthorhombic structure the polarization vector can exits along any of the twelve <101> directions and in the rhombohedral structure there are eight possible <111> directions which the polarization vector can exist along. An applied electric field can cause the polarization vector to switch between any of the different directions.

2.4.2. Lead Titanate

In attempt to develop ferroelectric materials different materials were developed and others revisited. One of those revisited was lead titanate ($PbTiO_3$) due to its analogy to $BaTiO_3$ and high T_c. (Shirane, 1951) The room temperature structure of $PbTiO_3$ remains tetragonal across the solid solution, with an increase in tetragonality compared to $BaTiO_3$ with a c/a ratio of 1.063, which leads to high anisotropy of the piezoelectric and ferroelectric properties (Shirane, 1950). $PbTiO_3$ is a ferroelectric with a T_c ~490 °C above which the space group is cubic Pm3m and below which the space group is tetragonal P4mm.

$PbTiO_3$ is a stable perovskite which can be formed at low processing temperatures with no impurity phases. Therefore $PbTiO_3$ is often used as an

end-member in solid solutions to stabilize less stable perovskite phases (Eitel, 2001).

2.4.3. Lead Zirconate Titanate

In attempt to develop a material that exhibits piezoelectric properties over a wide range of temperatures lead zirconate titanate (known as PZT) was developed at the Tokyo Institute of Technology in the 1950's (Shirane, 1952). PZT is a combination of ferroelectric $PbTiO_3$ and antiferroelectric $PbZrO_3$ to form a continuous solid solution $Pb(Zr_xTi_{x-1})O_3$ where $0 < x < 1$. Where $x < 0.9$ the solid solution is ferroelectric with T_c ranging from 220 – 490 °C (Jaffe, 1954).

PZT goes through several phase transitions with varying composition and temperature. Virtually independent of temperature a phase boundary is present where $0.52 < x < 0.545$ (Moulson, 2003) which is termed the morphotropic phase boundary (between tetragonal P4mm and rhombohedral R3m). In 1999 a monoclinic phase was discovered below room temperature around the morphotropic phase boundary (MPB) for a narrow compositional range (Noheda, 1999). The piezoelectric properties of PZT are optimum with compositions around the MPB due to the increased number of allowable domain states (6 from the <100> tetragonal and 8 from the <111> rhombohedral phase).

Today PZT is the most widely used piezoelectric material for commercial applications. Research continues to be carried out on PZT to improve and enhance its piezoelectric properties (often by doping) and other piezoelectric materials continue to be compared against it.

2.4.4. Bismuth Ferrite

Bismuth ferrite ($BiFeO_3$) was first reported in the 1950's (Royen, 1957). Using x-ray diffraction (Zaslavskii, 1960) and neutron diffraction (Michel, 1969) $BiFeO_3$ was confirmed to be a rhombohedral distorted perovskite with

the space group R3c. This space group allows the $BiFeO_3$ crystal to be ferroelectric. $BiFeO_3$ has received a lot of interest due to its multiferroic properties as well as being a lead-free piezoelectric. The multiferroic properties of $BiFeO_3$ present the potential to couple either the electric or magnetic polarizations which would allow additional degree's of freedom in device design (Wang, 2003). Unfortunately bismuth ferrite has some disadvantages such as low resistivity, weak magnetoelectric effect and high electric coercive field, with the low resistivity of $BiFeO_3$ making the observation of the ferroelectric polarisation - electric field hysteresis loop difficult (Cheng, 2003). In attempt to solve these problems, doping with various ions on both the B-site and A-site of the bismuth ferrite structure has been employed (Cheng, 2003b), (Zhu, 2006). Other perovskites have been introduced to bismuth ferrite to form solid solutions. Among these, lead titanate appears to be a promising solution (Woodward, 1995), (Chen, 2010).

2.4.5. Bismuth Ferrite Lead Titanate

Bismuth ferrite lead titanate ($xBiFeO_3 – (1-x)PbTiO_3$) is a solid solution of bismuth ferrite and lead titanate. In the early 1960's $BiFeO_3 – PbTiO_3$ was first reported as a ferroelectric solid solution (Fedulov, 1961).

Bismuth ferrite $BiFeO_3$ is a ferroelectric perovskite and forms one end member of the solid solution $BiFeO_3 – PbTiO_3$. It has a T_c of 850 °C, below which the structure is rhombohedrally distorted and belongs to an R3c space group with tilted oxygen octahedral which is a pre-requisite for anti-ferroelectric magnetism (Michel, 1969). The ferroelectric perovskite lead titanate $PbTiO_3$ is the other end member of $BiFeO_3 – PbTiO_3$ with a T_c of 490°C (Jaffe, 1971), below which the structure is tetragonally distorted and has a P4mm space group.

In 1964 Fedulov published a complete phase diagram which indicated the presence of a morphotropic phase boundary (MPB) between the tetragonal ($x < 0.62$) and rhombohedral ($x > 0.7$) phase between $x = 0.62 - 0.7$, at which both the rhombohedral and tetragonal phases co-exist (Fedulov, 1964). Ever

since the first publications on bulk $BiFeO_3$ – $PbTiO_3$ (Vanevstev, 1960), (Fedulov, 1961), (Fedulov, 1964) much debate has surrounded the width of the morphotropic phase boundary and the lattice strain c/a ratio. Fedulov measure the c/a ratio as being 1.15 (x = 0.6), 1.16 (x = 0.625) and 1.17 (x = 0.65), with the MPB spanning between x = 0.65 – 0.72 (Fedulov, 1964). Sai Sunder later measured c/a ratio = 1.158 (x = 0.6) and 1.187 (x = 0.7) with the MPB spanning between x = 0.7 – 0.8 (Sai Sunder, 1995). Over the past decade the $BiFeO_3$ – $PbTiO_3$ phase diagram has been re-visited by several research groups, producing differing structural information (Woodward 2003), (Bhattacharjee, 2007), (Zhu, 2008). The most recent interpretation on the $BiFeO_3$ – $PbTiO_3$ phase diagram was reported by Zhu with a reported MPB width between x = 0.69 – 0.83 and c/a ratio = 1.187 (x = 0.69) decreasing with increasing $PbTiO_3$ content to 1.06 (x = 0) (Zhu, 2008). Zhu also reported extra diffraction peaks in addition to the rhombohedral and tetragonal reflections which were indexed as orthorhombic. The structural findings are summarised in Table. 2.1. and Figure. 2.14.

Table. 2.1. Summary of variation in lattice parameters for $xBiFeO_3$ – $(1-x)PbTiO_3$ as a function of composition and morphotropic phase boundary width.

Author	**Width of MPB**	**Max c/a ratio**	**x value (at max c/a ratio)**
Fedulov (1964)	0.65 < x < 0.72	1.17	0.65
Sai Sunder (1995)	0.7 < x < 0.8	1.187	0.7
Woodward (2003)	0.6 < x < 0.7	1.15	0.7
Bhattacharjee (2007)	0.69 < x < 0.73	1.187	0.69
Zhu (2008)	0.69 < x < 0.83	1.187	0.69

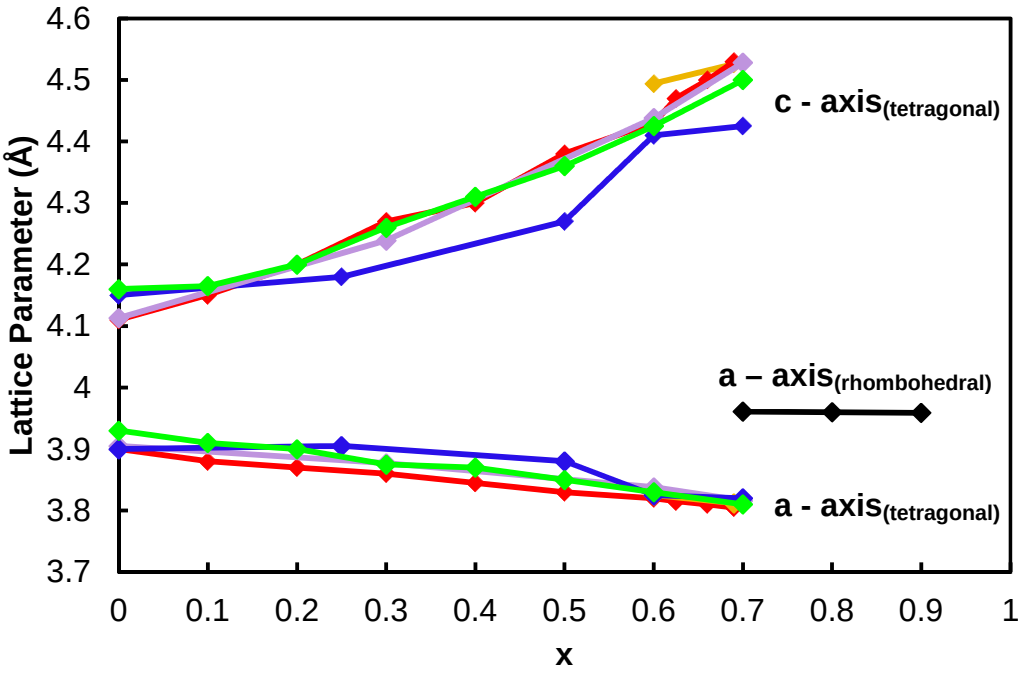

Figure. 2.14. Summary of variation in lattice parameters for $xBiFeO_3$ – (1-x)$PbTiO_3$ as a function of composition (from data in Table. 2.1).

For all the studies described in Table. 2.1. various sample forms were used to crystallographically characterise the $BiFeO_3$ – $PbTiO_3$ samples. These include crushed pellets, bulk pellets as well as annealed crushed pellets. Each process route is likely to induce differing levels of internal stress and could explain the variation in lattice parameters reported by different research groups. All of the studies employed x-ray diffraction to structurally characterise the samples which is known to produce results relating to the surface rather than the bulk crystallography due to x-ray penetration depths. Therefore this may contribute to the varying lattice parameters reported by different research groups.

Regardless of the MPB position all literature to date reports an increase in electrical permittivity and piezoelectric activity around the MPB which is generally attributed to the increased lattice strain in this region. Due to the conductivity of the material ferroelectric loops have never been measured for bulk $xBiFeO_3 – (1-x)PbTiO_3$, with samples electrically breaking down before hysteresis loops can be saturated (Comyn, 2004).

Previous work on $xBiFeO_3 – (1-x)PbTiO_3$ bulk ceramics suggests that hoping of electrons from Fe^{2+} to Fe^{3+} through oxygen vacancies results in electrical conductivity (Zhu, 2008), (Bell, 2007).

Over the past decade the addition of dopants in the $xBiFeO_3 – (1-x)PbTiO_3$ solid solution has been explored by several research groups. The dopants include titanium, manganese, gallium and lanthanum (Sakamoto, 2009), (Chen, 2011), (Chen, 2010), (Bell, 2007), (Cheng, 2005), (Cheng, 2003b). In the majority of these cases it has been where Mn (or other dopants) replace the Fe on the B-site (Fe/Mn ratio) that has been adjusted in attempt to increase the resistivity.

Gallium doping has been shown to generate resistivity up to 10^{13} Ω.cm when substituted for iron (Cheng, 2003). For $0.7Bi(Ga_xFe_{x-1})O_3 – 0.3PbTiO_3$ both the tetragonal and rhombohedral phases were detected where x = 0, with the rhombohedral phase being the dominant phase. However with increasing gallium concentration the x-ray traces show an increase in peak intensity for the tetragonal phase and a decrease in rhombohedral phase. For $0.7Bi(Ga_xFe_{x-1})O_3 – 0.3PbTiO_3$ where x = 0.25 is reported to be of significant importance as the resistivity was reported to increase rapidly $<10^{12}$ Ω.cm however with increasing gallium content the resistivity only increases slightly (Cheng, 2003).

Studies on lanthanum doped $xBiFeO_3 – (1-x)PbTiO_3$ have reported a decreased tetragonality and enhanced ferroelectric and piezoelectric properties with increasing lanthanum concentration. The tetragonal c/a ratio has been reported to dramatically decrease, with values ranging from 1.10 – 1.01 for lanthanum concentrations from 0 – 30 atomic % (Cheng, 2003), (Cheng 2003b), (Leist, 2010), (Leist, 2009).

The manganese ion has a similar ionic radius to the iron ion and can therefore readily substitute on the B-site of the $xBiFeO_3 – (1-x)PbTiO_3$ system. It has been reported that even extremely low levels of manganese doping (Mn = 0.001 atomic %) increases the resistivity of $xBiFeO_3 – (1-x)PbTiO_3$ by two orders of magnitude (Bell, 2007). Bell reports an increase in resistivity by ~ 2 orders of magnitude as a result of manganese doping (0.75 atomic %) on the iron B-site with an increase in activation energy and a reduction in the space charge contribution. It is suggested that the hopping of electrons from the Fe^{2+} to Fe^{3+} is prevented by the addition of manganese which acts to trap the holes. Titanium doping on the iron B-site is reported to act in a similar way in both bulk ceramics (Zhu, 2006) and thin films (Chen, 2010) (Chen, 2011).

The $BiFeO_3 – PbTiO_3$ solid solution system has attractive potential for use in high temperature ferroelectric applications due to its high Curie temperature in comparison to other ferroelectric systems. For example, $BiFeO_3 – PbTiO_3$ has a Curie temperature of 638°C (Sai Sunder, 1995) at the MPB (x = 0.7) which is considerably higher than that of PZT ($Pb(Zr_xTi_{x-1})O_3$) with a Curie temperature of 386°C at the MPB (x = 0.52), (Jaffe, 1971).

In addition to the high Curie temperature, the weak ferromagnetism in the $BiFeO_3 – PbTiO_3$ system was predicted and confirmed by Fedulov and Sakamoto, with a room temperature spontaneous specific magnetization decreasing from 0.018 emu g^{-1} for x = 0.9 to 0.005 emu g^{-1} for x = 0.3, which makes $BiFeO_3 – PbTiO_3$ attractive for potential multiferroic applications (Fedulov, 1964), (Sakamoto, 2009).

2.5. References

ATTICA, S. M., J. WANG, G. M. WU, J. SHEN, J. H. WU. (2002). Review on Sol-Gel Derived Coatings: Process, Techniques and Optical Applications. *J. Mater. Sci. Technol*. **18**, pp.211-218.

BELL, A. J., T. SCHLEGEL, M. ALDURAIBI, M. A. KHAN, T. P. COMYN, J. RODEL. (2007). Impedance spectroscopy of Mn-doped BiFeO3 – PbTiO3 ceramics. 2006 *15th IEEE International Symposium on Applications of Ferroelectrics, IEEE Transactions*. pp.130-133

BHATTACHARJEE, S., S. TRIPATHI, D. PANDEY. (2007). Morphotropic phase boundary in (1-x)BiFeO3 – xPbTiO3: phase coexistanence region and unusually large tetragonality. *Appl. Phys. Lett*. **91**, pp.042903-1

BIRKHOLZ, M. (2006). *Thin Film Analysis by X-Ray Scattering*. Weinheim: Wiley-VCH.

BURFOOT, J. C. (1967). *Ferroelectrics: An Introduction to the Physical Principle*. Canada: D. Van Nostrand Company Ltd.

CHEN, L., W. REN, W. ZHU, Z. G. YE, P. SHI, et al. (2010). Improved dielectric and ferroelectric properties in Ti-doped $BiFeO_3$-$PbTiO_3$ thin films prepared by pulsed laser deposition. *Thin. Solid. Films.* **518**(6), pp.1637-1640

CHEN, L., W. REN, W. ZHU, Z. G. YE, P. SHI, et al. (2011). Structural, dielectric and ferroelectric properties of Ti-modified $0.72BiFeO_3$ - $0.28PbTiO_3$ thin films prepared by pulsed laser deposition. *Ferroelectrics.* **410**(1), pp.42-49

CHENG, J., Z. MENG, L .E. CROSS. (2005). High field and high Tc piezoelectric ceramics based on Bi(Ga,Fe)O3 – PbTiO3 crystalline solutions. *J. Appl. Phys*. **98**(8), pp. 084102-5.

CHENG, J., N. LI, L .E. CROSS. (2003). Structural and dielectric properties of Ga-modified BiFeO3 – PbTiO3 crystalline solutions. *J. Appl. Phys*. **94**(8), pp. 5153-5157.

CHENG, J., L .E. CROSS. (2003b). Effects of La substitution on ferroelectric rhombohedral/tetragonal morphotropic phase boundary in (1-x)(Bi,La)$(Ga_{0.05}Fe_{0.95})O_3$ – x$PbTiO_3$ piezoelectric ceramics. *J. Appl. Phys*. **94**(8), pp. 5188-5191.

CHRISEY, D. B., G. K. HUBLER (1994). *Pulsed Laser Deposition of Thin Films.* New York: John Wiley.

COMYN, T. P., S. P. MCBRIDE, A. J. BELL. (2004). Processing and electrical properties of $BiFeO_3$ – $PbTiO_3$ ceramics. *Mater. Lett.* **58**(30), pp.3844-3846.

CULLITY, B. D. (2001). *Elements of X-Ray Diffraction*. 3rd Edition. London: Prentice-Hall International.

EITEL, R. E., C. A. RANDALL, T. R. SHROUT, P. W. REHIG et al. (2001). New high temperature morphotropic phase boundary piezoelectrics based on Bi(Me)O_3 – $PbTiO_3$ ceramics. *Jpn. J. Appl. Phys*. **40**(10), pp. 5999-6002

FEDULOV, S. A. (1961). Determination of Curie temperature in ferroelectric $BiFeO_3$. *Dolk. Akad. Nauk. SSSR.* **139**(6), pp.1345

FEDULOV, S. A., P. B. LADYZHINSKII, I. L. PYATGORSKAYA, Y. N. VENEVTSEV. (1964). Complete phase diagram of the $PbTiO_3$ – $BiFeO_3$ system. *Sov. Phys. Solid State*. 6, pp.375-378.

GOLDSCHMIDT, V. M. (1927). Geochemische Verteilungsgesetze der Elemente VIII. *Skr. Nor. Vidensk-Akad*. **1**, pp.1

HAMMOND, C. (2009). *The Basics of Crystalloraphy and Diffraction*. 3rd Edition. New York: Oxford University Press.

HAERTLING, G. H. (1999). Ferroelectric ceramics: History and technology. *J. Amer. Ceram. Soc*. **82**(4), pp.797-818

JAFFE, B., W. R. COOK, H. JAFFE. (1971). *Piezoelectric Ceramics*. London: Academic Press Inc.

JAFFE, B., R. S. ROTH, S. MARZULLO. (1954). Piezoelectric properties of lead zirconate – lead titanate solid-solution ceramics. *J. Appl. Phys*. **25**(6), pp.809-810

KAY, H. F., P. VOUSDEN. (1949). Symmetry changes in barium titanate at low temperatures and their relation to its ferroelectric properties. *Philos. Mag.* **40**(309), pp.1019-1040

KHAN, M. A., T. P. COMYN, A. J. BELL. (2007a). Ferroelectric BiFeO3-PbTiO3 thin films on Pt/Si substrates. *Ultrasonics, Ferroelectrics and Frequency Control, IEEE Transactions.* **54**, pp.2583.

KHAN, M.A., T. P. COMYN, A. J. BELL. (2007b). Large remanent polarization in ferroelectric BiFeO3-PbTiO3 thin films on Pt/Si substrates. *Appl. Phys. Lett.* **91**(3), pp.032901.

KHAN, M. A. (2008). *Preperation and properties of bismuth ferrite lead titanate thin films prepared by pulsed laser deposition*. PhD thesis, University of Leeds.

LADD, M., R. PALMER (2003). *Structure determination by X-Ray Crystallography*. 4rd Edition. New York: Kluwer Academic / Plenum Publishers.

LEIST, T., T. GRANZOW, J. WOOK, J. RODEL. (2010). Effects of tetragonal distortion on ferroelectric domain switching: a case study on La-doped $BiFeO_3$ – $PbTiO_3$ ceramics. *J. Appl. Phys*. **108**(1), pp. 014103-6.

LEIST, T., J. WOOK, A. J. BELL, J. RODEL. (2009). Shift in morphotropic phase boundary in La-doped $BiFeO_3$ – $PbTiO_3$ piezoceramics. *Jpn. J. Appl. Phys.* **48**(12), pp. 120205-3.

MEGAW. H. D. (1945). Crystal structure in barium titanate. *Nature.* **155**, pp.484-485

MEGAW, H. D. (1952). Origin of ferroelectricity in barium titanate and other perovskite- type crystals. *Acta. Crystallogr.* **46**, pp.739-749

MEGAW, H. D. (1957). *Ferroelectricity in Crystals*. Academic Press Inc. London: Methuen.

MICHEL, C., J. M. MOREAU, G. D. ACHENBACH, R. GERSON, W. J. JAMES. (1969). The atomic structure of $BiFeO_3$. *Solid. State. Commun.* **7**, pp.701-704

MITCHELL, R. H. (2002). *The Perovskites Modern and Ancient*. Thunder Bay, Canada: Almaz Press.

MOULSON, A. J., J. M. HERBERT (2003). *Electroceramics: Materials, Properties and Applications*. 2nd Edition. Chichester, UK: John Wiley and Sons Ltd.

NOHEDA, B., D. E. COX, G. SHIRANE, J. A. GONZALO, L. E. CROSS, S. E. PARK. (1999). A monoclinic ferroelectric phase in the $Pb(Zr_{1-x}Ti_x)O_3$ solid solution. *App. Phys. Lett*. **74**(14), pp.2059-2061

OHRING, M. (2002). *Materials Science of Thin Films: Deposition and Structure*. 2nd Edition. London: Academic Press Inc.

PAZ DE ARAUJO, C., J. F. SCOTT, G. W. TAYLOR (1996). *Ferroelectric thin films: synthesis and basic properties*. Amsterdam: Gordon and Breach.

PENN ENGINEERING. (2011). *Solid State Chemistry – Bravais Lattices* [online]. Philadelphia, USA: Penn Engineering. [Accessed 19 June 2011]. Available from:http://www.seas.upenn.edu/~chem101/sschem/solidstatechem.html

POLLA, D. L., L. F. FRANCIS. (1998). Processing and characterization of piezoelectric materials and integration into microelectromechanical systems. *Annu. Rev. Mater. Sci.* **28**, pp. 563-597

ROYEN, P., K. SWARS. (1957). Das system wismutoxyd-eisenoxyd im bereich von 0 bis 55 mol% eisenoxyd. *Angew. Chem.* **69**, pp.779SAI SUNDER, V. V. S. S., D. HALLIYAL, A. M. UMARJI. (1995). Investigation of tetragonal distortion in the BiFeO3 – PbTiO3 system by high temperature X-ray diffraction. *J. Mater. Res*. **10**(5), pp. 1301-1306.

SAI SUNDER, V. V. S. S., D. HALLIYAL, A. M. UMARJI. (1995). Investigation of tetragonal distortion in the BiFeO3 – PbTiO3 system by high temperature X-ray diffraction. *J. Mater. Res*. **10**(5), pp. 1301-1306.

SAKAMOTO, W., A. IWATA, T. YOGO. (2009). Electrical and magnetic properties of Mn-doped $0.7BiFeO_3 – 0.3PbTiO_3$ thin films prepared under various heating atmospheres. *Mater. Chem. Phys.* **116**(2-3), pp.536-541

SHANNON, R. D. (1976). The Revised effective ionic radii in halides and chalcogenides. *Acta Cryst*. **A32**, pp.751-767

SHIRANE, G., S. HOSHINO, K. SUZUKI. (1950). X-ray study of the phase transition in lead titanate. *Phys. Rev. Lett*., **80**(6), pp.1105-1106

SHIRANE, G., S. HOSHINO. (1951). On the phase transition in lead titanate. *J. Phys. Soc. Japan*. **6**(4), pp.265-270

SHIRANE, G., A. TAKEDA. (1952). Phase transitions in solid solutions of $PbZrO_3$ and $PbTiO_3$ (I) small concentrations of $PbTiO_3$. *J. Phys. Soc. Japan*. **7**(1), pp.5-11

VENEVTSEV, Y. N., G. S. ZHDANOV, S. N. SOLOVEV, E. V. BEZUS, V. W. IVANOVA, S. A. FEDULOV, A. G. KAPYSHEV. (1960). Crystal chemical studies of substances with perovskite type structure and special dielectric properties. *Soviet. Phys. Crystallogr*. **5**, pp.594-599

VON HIPPEL, A., R. G. BRECKENRIDGE, F. G. CHESLEY, L. TISZA. (1946). High dielectric constant materials. *Ind. Eng. Chem. Res*. **38**(11), pp.1097-1109

WANG, J., J. B. NEATON, H. ZHENG, V. NAGARAJAN, S. B. OGALE, B LIU, et al. (2003). Epitaxial $BiFeO_3$ multiferroic thin film heterostructures. *Science*. **299**, pp.1719-1722

WOODWARD, D. I., I. M. REANEY, R .E. EITEL, C. A. RANDALL. (1995). Crystal and domain structure of the BiFeO3 – PbTiO3 solid solution. *J. Appl. Phys*. **94**(5), pp. 3313-3318.

WUL, B. M., I. M. GOLDMAN. (1945). Dielectric constant of titanates of the metals of the second group. *C. R. Acad. Bulgare. Sci*. **46**(4), pp.139-142

ZASLAVSKII, A. I., A. G. TUTOV. (1960). The structure of new antiferromagnetic $BiFeO_3$. *Dokl. Akad. Nauk. SSSR*. **135**, pp.815-817

ZHU, W. M., Z .G. YE. (2006). Improved dielectric and ferroelectric properties of high Curie temperature (1-x)BiFeO3 – xPbTiO3 ceramics by aliovalent ionic substitution. *Appl. Phys. Lett*. **89**(23), pp. 232904-/1-3.

Chapter 3

Experimental Procedures

The initial part of this chapter gives a general description of the thin film preparation technique, pulsed laser deposition (PLD), with a detailed description of the PLD configuration used to deposit the films in this work. The PLD conditions used to deposit specific $BiFeO_3$ – $PbTiO_3$ film compositions is discussed in Chapter 4. The substrates used underwent a cleaning procedure to ensure high quality films were deposited which is described. All processing techniques for the pulsed laser deposition target materials are described in depth which includes milling, calcination, pressing and sintering.

Analysis of the films produced in this work included several characterisation techniques, all of which require sample preparation to achieve optimum results. The sample preparation techniques of ceramic targets as well as thin films are described. Finally the analysis techniques; x-ray diffraction, scanning electron microscopy, transmission electron microscopy and atomic force microscopy are described.

3.1. Thin Film and PLD Target Processing

3.1.1. Pulsed Laser Deposition

Pulsed laser deposition (PLD) is a physical vapour deposition (PVD) technique where a pulsed laser beam strikes the surface of the target material causing the outermost layers of the target material to rapidly heat up and evaporate off. The evaporated target material forms a high energy plume, which deposits onto the heated substrate (Ohring, 2002), (Craciun, 1999).

Usually the PLD chamber contains a computer controlled target holder which can hold several targets at one time. By positioning the targets underneath the pulse laser, multilayer materials can easily be fabricated (Krupanidhi, 1983).

PLD offers advantages such as: dense films, low processing temperatures, a wide range of deposition rates, simple configuration and operation procedure as well as high reproducibility (Castellano, 1979).

Unfortunately PLD is limited to a small deposition area due to the narrow angular distribution of the plume which results in a non-stoichiometric film with non-uniform thickness. Another disadvantage of PLD is the splashing of target material onto the substrate which will affect the growth of subsequent layers and eliminate/reduce the electrical properties of the film.

3.1.1.1. Pulsed Laser Configuration at Leeds

A Tui Thin Film Star 248 nm KrF Excimer laser system was used to deposit material onto various substrates. The pulsed laser deposition system is composed of a very simple configuration with a high-vacuum chamber and pumping unit, an Excimer Laser including a beam-line, as well as a substrate and target manipulator.

Ultra short pulses of the laser-beam are focussed through a set of mirrors and lenses and guided through the beam-line into the high vacuum chamber (Chrisey, 1994). On entering the high energy vacuum, the laser-beam

interacts with the target which is positioned in the target manipulator. The target manipulator is fixed to the bottom of the chamber and has a rotary drive to move the targets forwards and backwards (toggle) as well as rotating the targets. This allows for up to four different targets to be used during each pulsed laser deposition process as well as uniform ablation of each target.

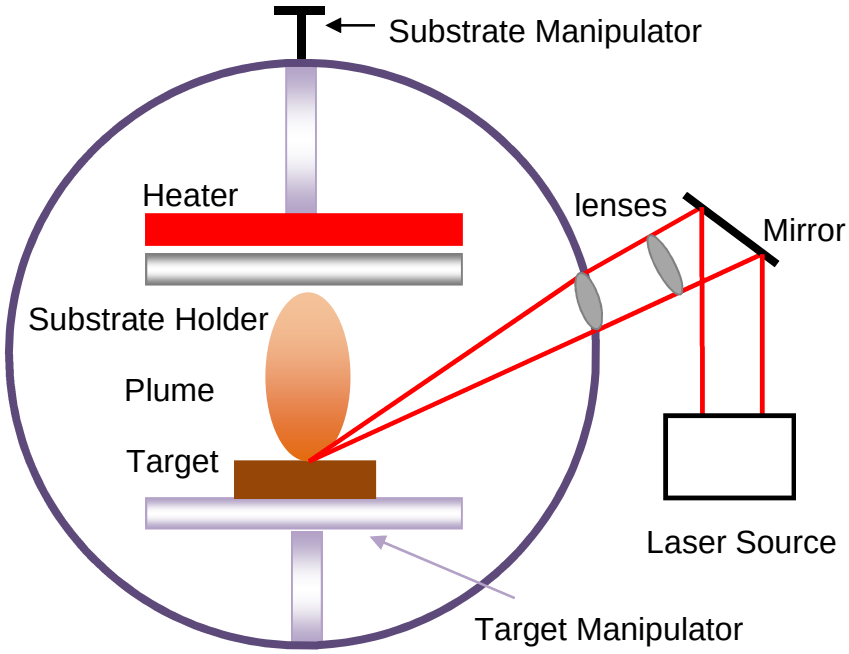

Figure. 3.1. Schematic of the pulsed laser deposition configuration used to deposit the films discussed in Chapter 5 and 6.

The electromagnetic energy of the high energy laser-beam is converted to electronic excitations in the target material, which is converted to thermal, mechanical and chemical energy resulting in the formation of a plasma plume perpendicular to the surface of the target.

There are several circumstances in which the quality of the KrF laser gas and therefore the laser output energy deteriorates. For this reason simple precaution measures must be undertaken:

The lifetime of the laser gas can be defined in terms of a static and dynamic gas lifetime. The static gas lifetime is effected by the reaction of fluorine with

the laser tubes inner surface, resulting in contamination with trace elements. The static gas life is estimated to be approximately 10 days. The dynamic gas lifetime is affected by contact with discharge debris during laser operation and is given as 6 million shots. Both the static and dynamic gas lifetime adversely affect the reproducibility of results. Therefore the gas must be purged from the gas lines and backfilled with pre-mix gas from the gas cylinders (Surface, 2006).

After each deposition cycle the port window (through which the laser enters the chamber) has a residue of material remaining on its surface. This can cause a substantial drop in the laser energy. To avoid this change in laser-beam energy, the port window must be cleaned by a 1 micron diamond paste followed by a wipe with isopropan-2-ol on clean room paper, after each deposition cycle.

The simplicity of this equipment makes pulsed laser deposition a very attractive process for the manufacture of thin films.

3.1.2. Cleaning of Substrates

$Pt/TiO_x/Si/SiO_2$ substrates of two different orientations; (111) orientated and polycrystalline, were used as the substrates in this work. The substrates were cut from a wafer into 9.5 mm x 9.5 mm squares using a Karl Suss scriber. The substrates were ultrasonically cleaned in acetone for five minutes to ensure the removal of any debris and residue from the wafer surface. The substrates were then ultrasonically cleaned in iso-propan-2-ol (IPA) for a further five minutes to remove the acetone (a degreasing agent) from the wafer surface, followed by a rinse in de-ionized water. The substrates were then blow dried with nitrogen.

3.1.3. Platinum Substrates

The work reported in this thesis discusses films deposited by pulsed laser deposition on two different substrates: The first substrate is refered to as

(111) oreiented Pt substrate. These substrates are $Pt/TiO_x/SiO_2/Si$ substrates where the Pt substrates (111) plane is orientated out of plane.

The second substrate used in this work is referred to as *preferentially oriented Pt*. These substrates are $Pt/TiO_x/SiO_2/Si$ substrates where the Pt has the (111) plane and some (200) plane orientated out-of-plane. Although there are two different crystallographic planes orientated out-of plane on the substrate's deposition surface, the substrates are referred to as preferentiality orientated Pt due to the absence of other crystallographic out-of-plane orientations.

The preferentially oriented Pt substrates (PIKEM, UK) were intended to be (111) orientated out-of-plane, however due to unknown problems in the production methods (most probably spin coating temperature) the out-of-plane orientation of the substrates were not the expected (111).

3.1.4. PLD Target Processing

The laser targets were produced by a mixed-oxide route whereby stoichiometric ratios of metal oxide reactants; Fe_2O_4, Bi_2O_3, PbO, TiO_2 (99.9% Sigma Aldrich, Dorset, UK) were mixed to produce:

$$xBiFeO_3 – (x\text{-}1)PbTiO_3 \text{ where } x = 0.7 \text{ and } 0.6$$

TiO_2, was dried in Al_2O_3 crucibles at 300 °C for 4 hours prior to mixing with other reagents as they are hygroscopic materials and therefore potentially retain water which can alter the physical properties of the powder. Once dried, the powders were stored in a sealed decicator to avoid contact the air. The reagents were weighed out in batches of 400 g to an accuracy of 0.01 g before milling.

3.1.4.1. Milling

The mixed powders were ball milled in iso-propan-2-ol for 5 hours in high density polyethylene cylinders with 10mm diameter ZrO_2 milling media to thoroughly mix the reagents and reduce the particle size. However to produce dense pulsed laser deposition targets even finer particle sizes are required. To further reduce particle size from that produced by ball milling, the slurry was attrition milled for a further 2 hours. The attrition mill used was a DYNO Mill (KDLA, Switzerland) with 0.5 mm diameter yttrium - stabilised zirconia balls. The attrition milling process offers a finer distribution of particle sizes as well as a smaller particle size which will produce a dense, homogeneous target. The milling media was removed and the remaining slurry dried on a hot plate in clean glassware at ~ 60 °C. The dried powders were then ground with a pestle and motar to pass through a 300 micron mesh sieve.

3.1.4.2. Calcination

The sieved powders were transferred into lidded Al_2O_3 crucibles to undergo the calcination stage whereby a complete thermochemical reaction of the mixed powders produced the desired solid-solution. A heating rate of 20°C $hour^{-1}$ was upto 400°C followed by a heating rate of 300°C $hour^{-1}$ up to 800°C reaction temperature. The powders were held at reaction temperature for 4 hours and cooled down to room temperature at a rate of 300°C $hour^{-1}$. The calcined powders were then passed through a 300 micron mesh sieve and further attrition milled for 1 hour with a 1.5 wt% of binder additive (Ciba Glascol HA4) to increase the binding between particles during pressing. The powders were dried and sieved through a 300 micron mesh sieve before being pressed. The powders were pressed using a hydraulic press in a stainless steel 40 mm diameter die. To increase the green density of the targets the hydraulic pressing was followed by cold isostatic pressing at 400 MPa.

3.1.4.3. Sintering

Owing to the higher green density of the pressed targets, an appropriate sintering regime is essential to ensure complete burn out of the binder and avoid porosity in the final sintered target. The targets were placed on an alumina tile bedded in calcined powder of the same composition in avoid a loss of bismuth and lead as they are volatile elements. The sintering regime included an initial slow heating stage to 525°C at 30°C $hour^{-1}$ and a dwell time of 15 minutes to ensure complete burn out of the binder. This was followed by a ramp rate of 300°C $hour^{-1}$ to the final sintering temperature of 1000°C and held for 30 minutes. A cooling rate of 300°C $hour^{-1}$ was used down to 700°C followed by a slow cooling rate of 15°C $hour^{-1}$ to room temperature. The slow cooling rate through the Curie point was used so the material is able to accommodate the large changes in stain experienced as the material undergoes a phase transition. If the cooling rate was set to fast the target is likely to have experienced micro cracking.

All targets were polished to a 1 µm finish ready for x-ray analysis and use in the pulsed laser deposition process.

3.2. Sample Characterisation

3.2.1. X-Ray Diffraction

X-ray diffraction (XRD) is a technique commonly used to characterise the structure of crystalline materials. In thin films the distribution of crystallite orientations in polycrystalline films is rarely isotropic, with a certain crystallographic direction (hkl) being found to be preferentially orientated normal to the sample surface. As well as structural information, x-ray diffraction allows the preferential orientation (texture) to be determined which can be used to understand the nature of the films electrical properties. To understand how this analysis is achievable the x-ray radiation source, experimental configuration, x-ray interaction with matter and principles of diffraction are discussed.

3.2.1.1. Interaction of Radiation with Matter

Radiation is commonly used to characterise the structure and chemical make-up of crystalline materials. Radiation in the form of x-rays, neutrons and electrons can be described as both wavelike and particle like. When an incident beam of radiation interacts with a material it will be scattered. There are different types of scattering processes which can be divided into two groups (Kelsall, 2005):

Elastic Scattering:	No energy transfer but changes in direction of the incident wave may be present
Inelastic Scattering:	Energy transfer and a possible change in the direction of the incident wave

The scattering process can be divided between:

Coherent Scattering:	The incident waves are all in-phase
Incoherent Scattering:	The scattered waves are not in-phase

3.2.1.2. Laboratory X-ray Diffraction

X-rays are produced in the laboratory by x-ray tubes in which a tungsten filament is heated by electrical current which emits electrons. These electrons are drawn to a metal target (Cu, Al, Mo, Mg, Ag) anode by a high potential difference. The incident electrons undergo inelastic collisions with inner shell (K, L, M) electrons in the metal atom (Cullity, 2001). Energy is transferred from the incident electron that excites the inner shell electrons in the target to higher energy levels (resulting in a hole in the inner shell).

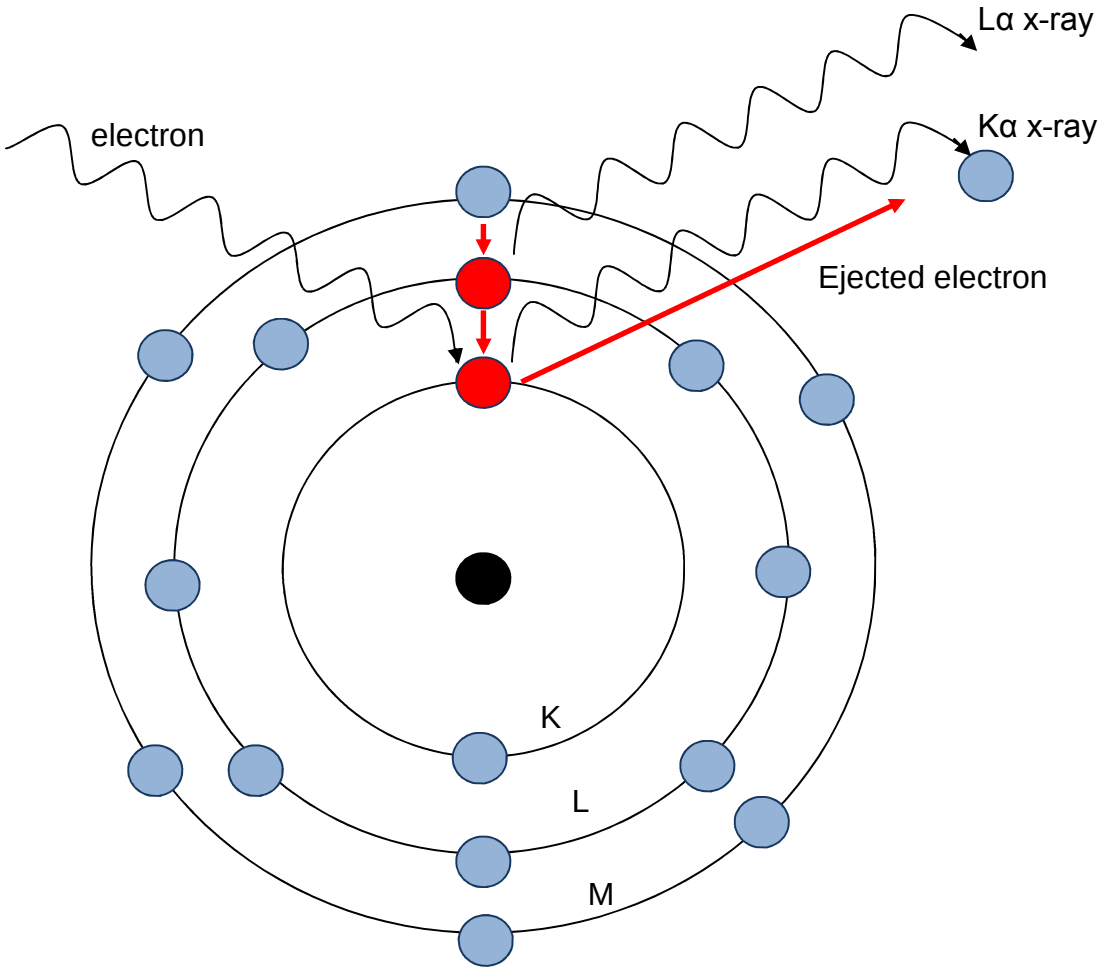

Figure. 3. 2. A diagram to describe electron interaction with an atom and the x-rays emitted as a result of the interaction

The atom de-excites by other electrons from higher energy levels (which fill the hole) resulting in the excess energy being lost in the form of an x-ray

photon. A set of different x-rays are produced (continuous spectrum) in this process because different energy levels are involved in the de-excitation process (Williams, 1996). For example; if a K-hole is filled by a L-shell electron, a Kα x-ray is produced but if an M-shell electron fills the K-hole a Kβ x-ray is produced (Cullity, 2001). Typical x-ray wavelengths for commonly used tube anodes are shown in Table. 3.1.

Table. 3.1. Typical wavelength for commonly used tube anodes (Cullity, 2001) (Birkholz, 2006).

	Wavelength, λ (Å)		
Anode	**$K\alpha_1$**	**$K\alpha_2$**	**$K\beta_2$**
Copper (Cu)	1.541	1.544	1.392
Molybdenum (Mo)	0.709	0.714	0.632
Chrome (Cr)	2.898	2.294	2.085

X-rays may be monochromated by filtering or using crystal monochromators which only allow a narrow energy range of x-rays to pass through and remove the effects of a continuous spectrum. Filters are thin sheets of an element which has a K absorption edge between the wavelength of the Kα and Kβ emission lines of the x-ray anode element. The Kβ line has enough energy to excite K-level electrons of the filter element while the Kα radiation has not, resulting in the majority of the Kβ line being absorbed. In the x-ray diffractometer used to carry out the experiments in this work a Copper (Cu) tube (anode) was used with a Nickel (Ni) filter to monochromate CuKα and Kβ radiation to mainly CuKα (Birkholz, 2006).

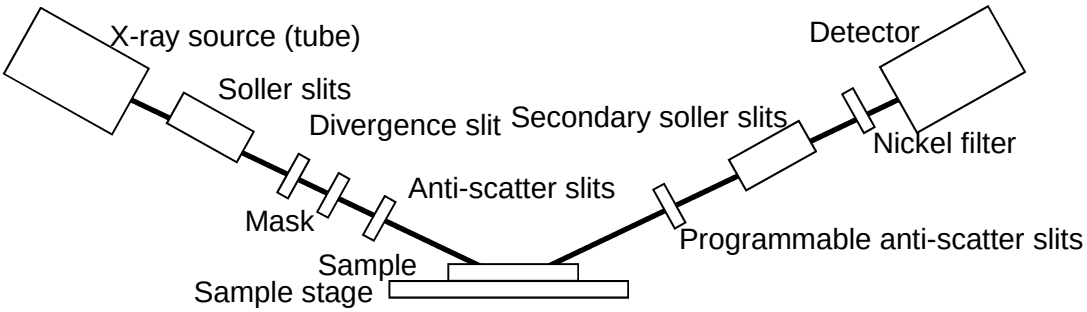

Figure. 3.3. Schematic of x-ray diffraction configuration used in this work

When the incident x-ray beam interacts with an atom a wave re-radiates with the same frequency (elastic scattering). The re-radiated x-ray from adjacent atoms can constructively and destructively interfere with each other producing a diffraction pattern. In a crystal lattice, when two or more x-rays waves are reflected from planes of atoms and the path difference between the reflections from adjacent planes is equal to an integer number of wavelengths diffraction occurs. This condition is termed Bragg's Law (Cullity, 2001).

Bragg's Law: $n\lambda = 2d_{hkl} \sin\theta$ *Equation. 3.1.*

where d is the interatomic spacing between adjacent planes, n is an integar, λ is the wavelength of the incident x-ray beam and θ is the angle between the incident beam and the scattered atomic planes.

There are several configurations using an x-ray diffractometer in which Bragg's Law can be satisfied for diffraction to occur. In this work the Bragg-Bretano configuration was used in which the monochromatic x-rays and diffracted radiation detector are located equal distance and angle to the sample surface.

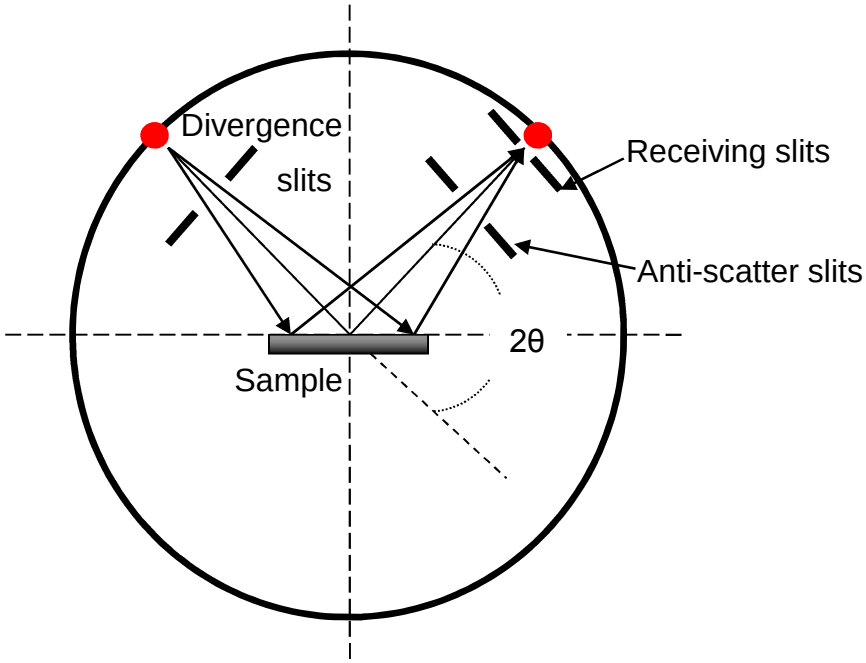

Figure. 3.4. Bragg – Brentano geometry used in the x-ray diffractometer (adapted from Birkholz, 2006)

3.2.1.3. Diffractograms and Peak Broadening

The x-ray intensities are recorded in a plot against 2θ to produce a θ - 2θ x-ray trace also known as a diffractogram. A diffractogram produced from a perfect arrangement of atoms in a crystal lattice will produce vertical lines with exact values of d-spacing for the plane.

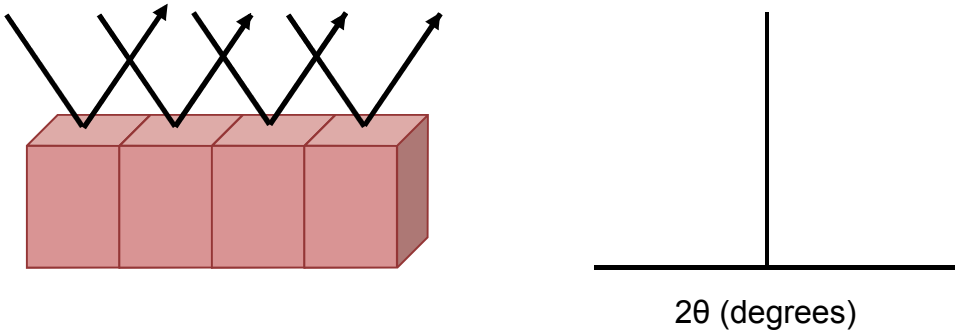

Figure. 3.5. Schematic of unit cells which make up a ‘perfect’ crystal and the resulting diffraction peak which exhibits no peak broadening

However strain, particle size and lattice defects within the material can cause the unit cell to become distorted which can produce varied lattice spacing's. Distortions of the lattice give rise to peak broadening in a x-ray dffractogram, with the d-spacing for a plane being distributed over a range.

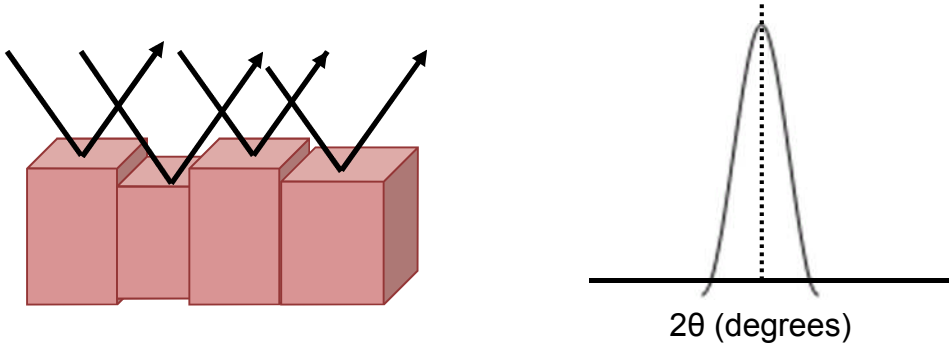

Figure. 3.6. Schematic of unit cells under different strain conditions and the resulting diffraction peak which exhibits peak broadening

The observed broadening can be used to calculate information such as particle size and strain contributions. In thin films the peak broadening reveals information on the crystallite size, shape, stress and texture (Birkholz, 2006).

In this work x-ray diffraction using the Bragg-Brentano configuration has been used to characterise the crystallographic structure and phase identification of the deposited thin films and ceramic target materials. The scans were carried out with a 2θ range from 15 - 60°, with a step size of 0.025° and a scan speed of 0.05° s^{-1}. However the penetration depth of the incident x-ray beam only allows the crystallographic structure of the samples surface to be analysed. In polycrystalline materials the lattice parameters can be calculated from the peaks indexed as the (001) (a-parameter), (010) (b-parameter) and (100) (c-parameter) planes. However in thin films this process cannot give a complete set of lattice parameter values using this method as the peaks on the diffractogram indexed as the (100), (010) and (001) may arise from different unit cells under different strain conditions

(imparted by the strain at the substrate-film interface). Therefore the complete set of lattice parameters for the deposited films can only be estimated using this method and not completely calculated.

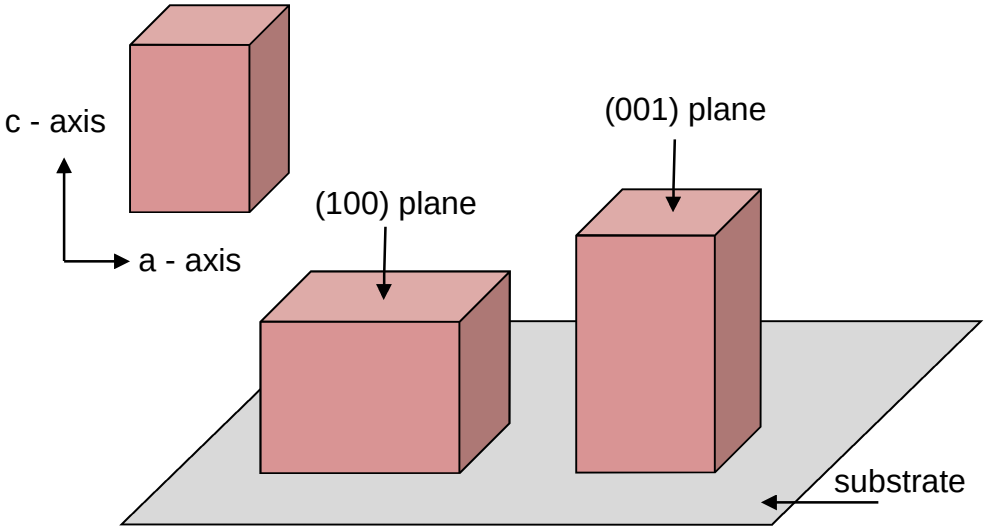

Figure. 3.7. Schematic of (100) and (001) orientated unit cells on a substrate material which demonstrates how the (001) and (100) reflections may not arise from unit cells of the same dimensions.

In thin film analysis using x-ray diffraction it must also be considered that due to geometrical constraints only the lattice planes hkl that are oriented parallel to the surface can contribute to a Bragg reflection. This may result in the absence of various reflections (peaks) and an increased intensity of specific reflections when compared to the powder diffractogram of the same material. This information reveals the out-of plane (preferential) texture in the films and can therefore be used to calculate the in-plane orientation as well. However, it is worth noting that in thin films the diffraction pattern exhibits a decrease in intensity with increasing scattering angle therefore diffractograms are usually presented as square-root intensity plots to emphasise the smaller peaks.

3.2.2. XRD - Sample Preparation

Both the ceramic targets and the thin films were prepared for x-ray diffraction analysis in the same way. However the ceramic targets were made smaller than those used in the pulsed laser deposition process to fit into the x-ray diffractometer sample stage.

The sample is placed onto a glass slide using moulding plasticine with the sample surface flat and matching the reference surface (which was an aluminium ‘bracket’). The sample is then mounted onto the x-ray diffractometer sample stage.

3.2.3. Scanning Electron Microscopy

Scanning electron microscopy (SEM) is a technique similar to optical microscopy but offers a higher resolution. Light microscopes have a magnification of ~1000 times and allow features separated by ~ 200 nm to be resolved, however the resolution power of a microscope is not solely limited by the number and quality of lenses but is limited by the wavelength of light. Therefore visible light only allows features to be resolved that are separated by ~ 200nm. Electrons in a vacuum travel in a straight line with wave-like properties ~ 100,000 times shorter than visible light. Electronic and magnetic fields are used to shape the electron beam (similar to a glass lenses in a light microscope). This allows electron microscopes to resolve features separated by ~ 0.05 nm. Although the wavelength associated with electrons is ~ 100,000 times smaller than the wavelength of light (~ 550 nm) this does not translate to a 1000,000 times better resolution due to a combination of beam voltage, aperture size and lens aberrations. The resolution also depends on electron spot size, working distance and interaction volume (Goodhew, 2001), (Loretto, 1994).

There are several basic modes of operation for scanning electron microscopy;

- Secondary electron imaging
- Backscattered electron imaging
- X-ray analysis and mapping (EDX – Energy Dispersive X-ray Analysis)

When the incident electron beam interacts with the samples surface, secondary electrons arise from the ionization of electrons associated with the atoms in the samples surface. Secondary electrons are low energy (< 50 eV) electrons which have escaped from the top 1 – 30 nm of the sample. Once the escaped electrons (from different points in the sample) are detected, an image is formed of the surface topography (Kelsall, 2005).

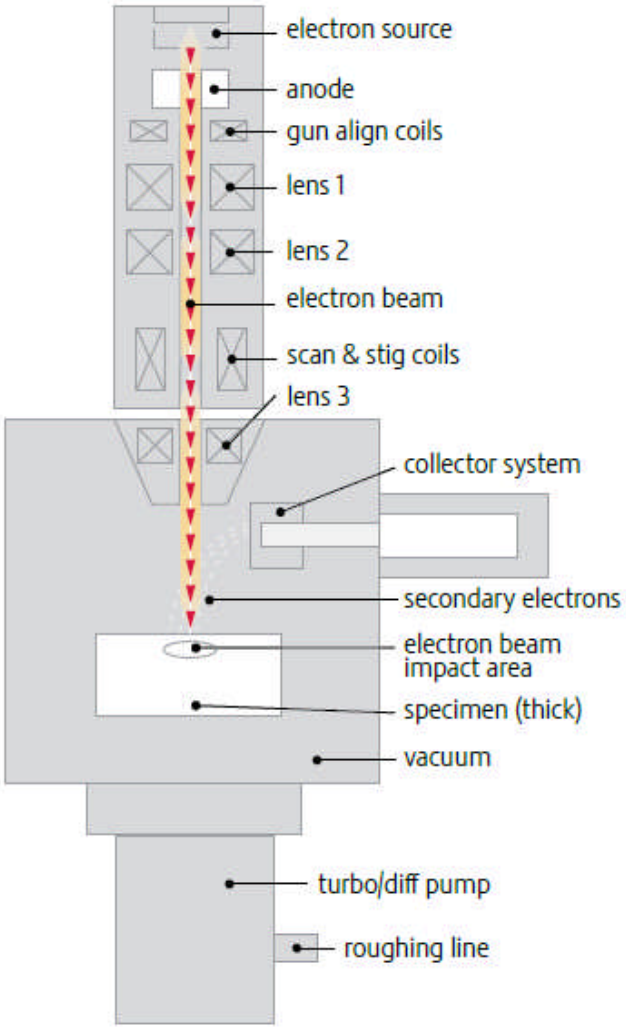

Figure. 3.8. Schematic representation of a scanning electron microscope [FEI, 2010]

Another imaging technique using the scanning electron microscope is known as backscattered electron imaging. This technique is used to image subsurface detail and is possible when higher energy electrons are backscattered from the top 10 – 100 nm of the samples surface. This is achievable when higher incident beam energy is emitted from the electron gun (1 – 20 keV). The intensity of the backscattered electrons is dependent on the average atomic number and can therefore be used to image atomic number contrast if the effects of topography have been removed (e.g. polishing). When the incident beam electrons travel deeper into the samples

surface they progressively spread out with increasing depth into the sample, which reduces the image resolution. Therefore secondary electrons are usually used when high resolution images of the sample are required. Just as was described in section 3.2.1.2. x-rays are emitted when incident beam electrons interact with matter. As the electron beam is scanned across the sample surface x-rays are emitted from all the different points the electron beam is scanned. Different elements in the sample produce x-rays of characteristic wavelengths which allow the distribution of elements in the sample surface (interaction of ~ 1 µm below the sample surface) to be mapped.

In this work the secondary electron imaging was used to image the topography of the ceramic targets as well as film's top surface and fracture surface. X-rays were used to map the elemental distribution before and after pulsed laser exposure. The SEM used in this work was a LEO1530 Gemini FEG-SEM fitted with an Oxford Instruments UTW EDX detector, running ISIS software. Images were taken at an operating voltage of 3 kV and a working distance of ~ 2 - 3 mm.

3.2.4. SEM - Sample Preparation

3.2.4.1. Bulk Ceramic Target

The polished ceramic targets were mounted on an adhesive carbon pad and placed onto an aluminium stub. This creates a conductive path from the aluminium stub to the sample which is then ground(ed) through the sample stage to prevent a charge build up. A charge build up on the sample surface prevents high resolution topography images from being obtained with no contrast between grains. To increase the conductivity path, the sample was coated with a 5 nm layer of Pt-Pd (Pt 80%, Pd 20%) using a platinum sputter coater (Agar High Resolution Sputter Coater).

3.2.4.2. Thin Film

There are two different sites of interest in thin films; the top surface and the fracture surface. By imaging the top surface and fracture surface, an indication of the microstructure, possible growth mechanisms, crystallite size and film thickness can be obtained. When mounting a film to image the top surface a very similar sample preparation technique is followed to the SEM preparation of the ceramic target (see section 3.2.4.1).

When imaging the top surface the film is mounted on an aluminium stub attached by an adhesive carbon tape. A conductive carbon paint is applied to the edge of the film down to the carbon pad. The film is sputter coated with a 5 nm layer of Pt - Pd.

To image the fracture surface a diamond scribe is used to scribe a linear line on the reverse side of the film which increases the possibility of a straight fracture surface. The film is then securely positioned in a 1 mm wide slit purposely cut into an aluminium stub. Added stability is achieved by applying carbon paint between the slit in the aluminium stub and the sample surface.

3.2.5. Transmission Electron Microscopy

Transmission electron microscopy (TEM) is analogous to SEM however the beam in TEM is focussed to a small probe and the transmission signal is detected instead of the backscattered or secondary electron signal.

The configuration of the transmission electron microscope can be compared to a light microscope to help understand how it operates:

- The *electron gun* replaces the light source which is built into a column.
- The lenses are replaced by *electromagnetic lenses* with the power being changed by altering the current through the lens coil.
- A fluorescent screen and digital camera replaces the eyepiece.

The electron beam emerges from an electron gun which is condensed (through condenser lenses) to form a nearly parallel beam when it reaches the sample (Williams, 1996).

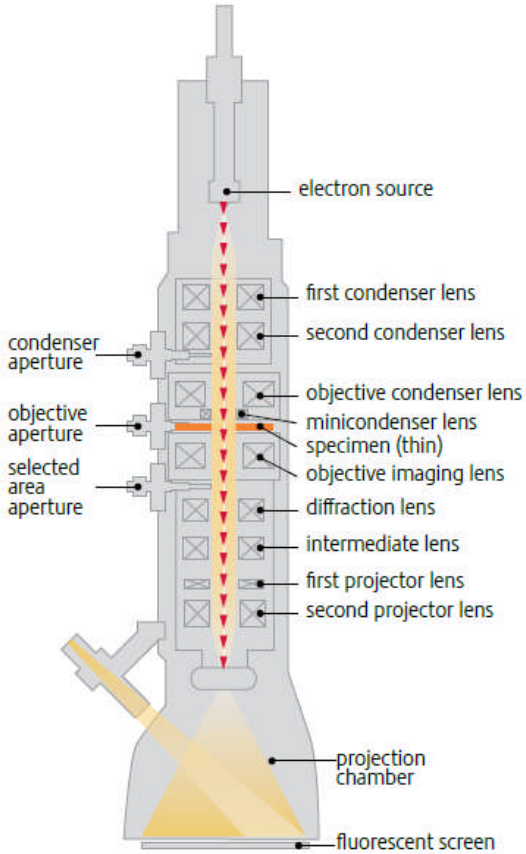

Figure. 3.9. Schematic representation of a transmission electron microscope [FEI, 2010]

Unlike SEM the sample must be thin enough to transmit the electrons (~ 0.5 µm) which allows the high energy electrons to pass through the sample and be collected and focussed by the objective lenses. A magnified image of the sample is projected (using projection lenses) onto the fluorescent disc at the bottom of the column. To avoid scattering of the electron beam the entire column is kept under vacuum.

There are many imaging mechanisms and modes of operation for transmission electron microscopy such as:

- Bright Fields (Diffraction Contrast)
- Dark Field (Diffraction Contrast)
- Lattice Imaging (Phase Contrast)
- Electron Diffraction
- Scanning Transmission Electron Spectroscopy (STEM)
- Spectroscopy Techniques
  - Energy Dispersive X-Ray (EDX)
  - Electron Energy Loss Spectroscopy (EELS)

Here the discussion has been limited to scanning transmission electron spectroscopy (STEM) and the spectroscopy technique energy dispersive x-ray (EDX) as these were the techniques used to analyse the films in this work.

Scanning TEM is analogous to SEM, however the electron beam is focussed to a small probe and the transmitted signal is measure (rather than secondary or backscattered electrons). The TEM configuration can be seen in Figure. 3.9. When the electron beam is focussed to a particular point, the x-ray energies emitted from the point of focus allow the distribution of elements to be determined and mapped (Brydson, 2007). This is possible by the detection of the characteristic energies of the emitted x-rays. These energies can then be assigned to a particular element (for more information refer to section 3.2.1.2).

The TEM used in this work was a Phillips CM200 FEG-TEM fitted with an Oxford Instruments UTW EDX detector, running INCA software. Images were taken at an operating voltage of 197 kV.

3.2.6. TEM – Sample Preparation: Focused Ion Beam Milling

Transmission electron microscopy (TEM) analysis was not carried out on the ceramic targets and therefore the discussion of sample preparation for TEM analysis is limited to thin films. All thin films analysed using TEM are required to be thin enough for the beam of high energy electrons to transmit through the thin film section (refer to Section 3.2.5). In this work the thin film sections were prepared using focused ion beam (FIB) milling. In this section a summary of basic focused ion beam milling is described as only limited use was made of this technique.

The FIB microscope is similar to the SEM (refer to Section 3.3.3) however the electron beam is replaced by a beam of positively charged gallium (Ga^{+}) ions which will sputter atoms away from the sample surface when the ion beam is focused to a point on the sample (FEI, 2010).

In this work focused ion beam milling was used to remove material from the sample with precise control via a sputtering technique. The milling was performed using a Nova200 DualBeam SEM/FIB, FEI, instrument which also incorporates an SEM. This allows immediate high resolution images of the milling process to be obtained to ensure the section being milled is thin enough to analyse in the TEM.

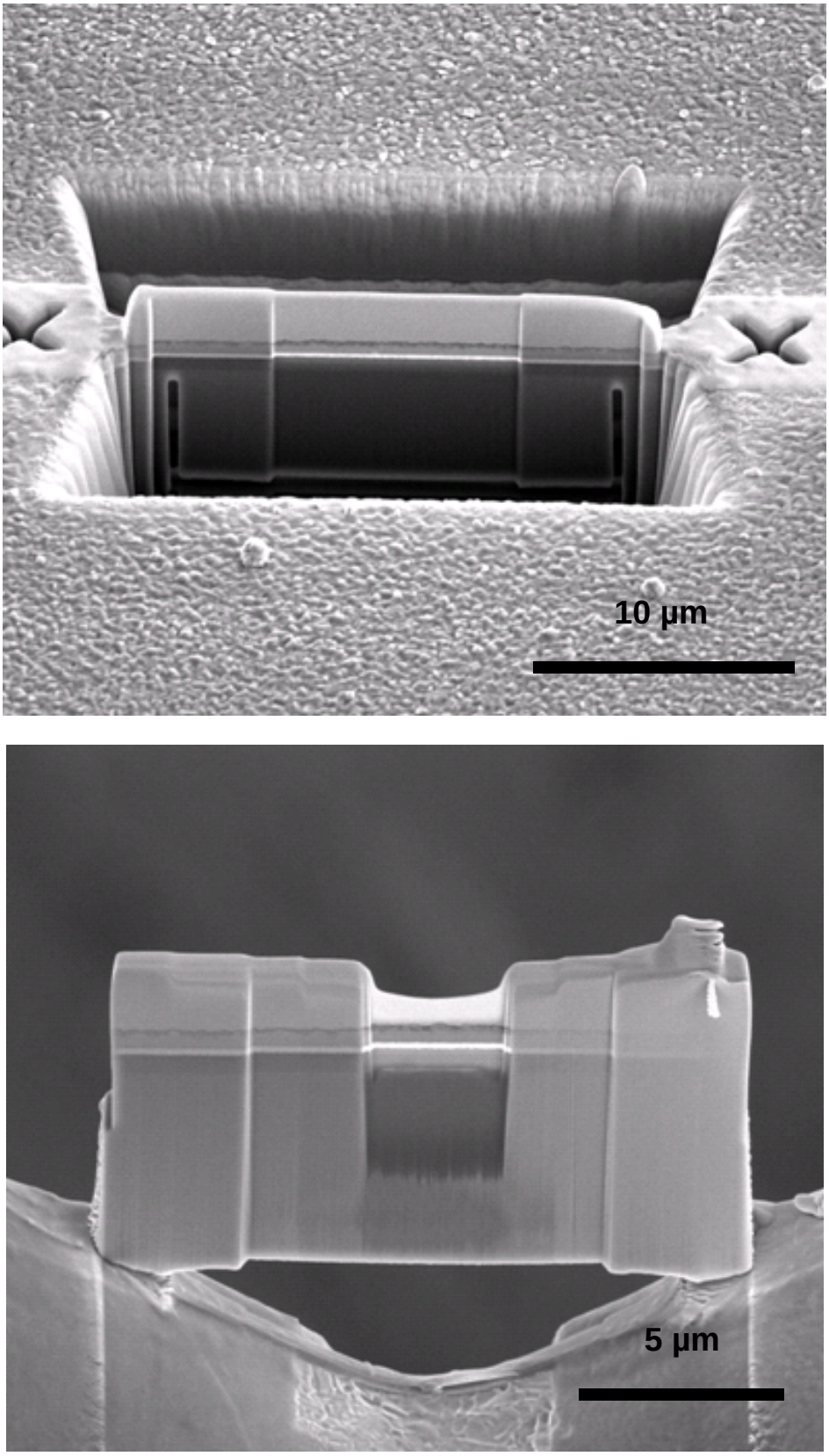

Figure. 3.10. Images taken during the focussed ion beam milling technique used to prepare the sample used in transmission electron microscopy analysis discussed in Chapter 5

3.2.7. Atomic Force Microscopy

Atomic force microscopy (AFM) is an imaging technique which uses a sharp tip (~ 2 µm) length and (~ 20 nm diameter) to scan over the sample surface where the magnitude of 'atomic forces' are measured as a function of the probe position in relation to the sample surface.

3.2.7.1. AFM Configuration

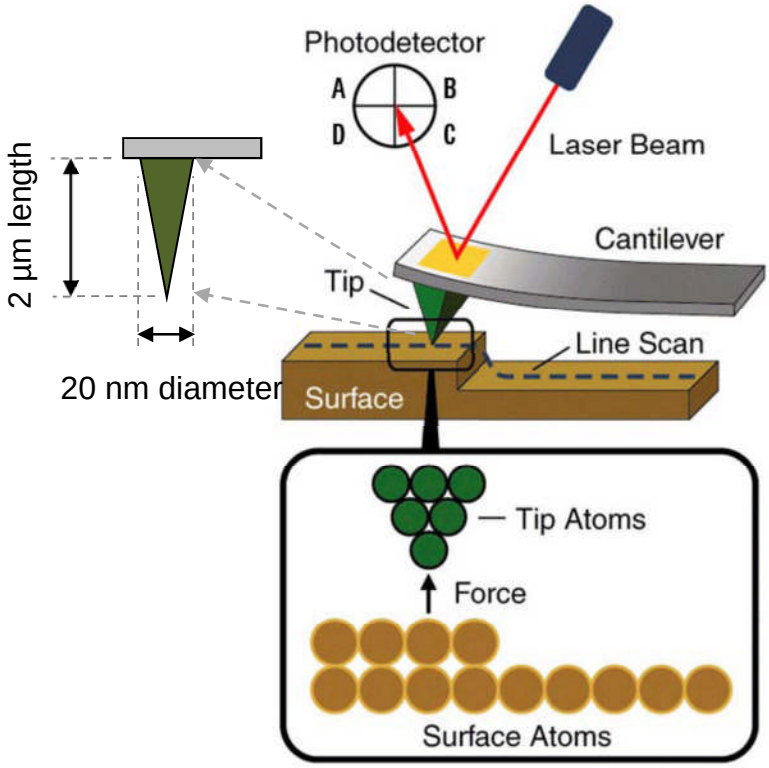

Figure. 3.11. Schematic representation of the tip – sample interaction in the atomic force microscope (Agilent, 2011)

The AFM tip is positioned at the end of the cantilever. Forces between the tip and sample surface may cause the cantilever to deflect and/or bend. The position of the cantilever is detected optically using a focussed laser beam which is reflected from the back of the cantilever (therefore resulting in a shift in the laser position with changing tip position) onto a position sensitive photo detector. The measured deflections generate a map of surface topography. Topography maps are generated by operating with a constant current or constant height because the detector measures a signal from the microscope

and adjust the tip *z*-position to keep this signal at a constant value (Kelsall, 2005).

Constant Height: Topography is measured by changes in current.

Constant Current: Topography is measured by changes in tip-sample separation needed to keep the current constant.

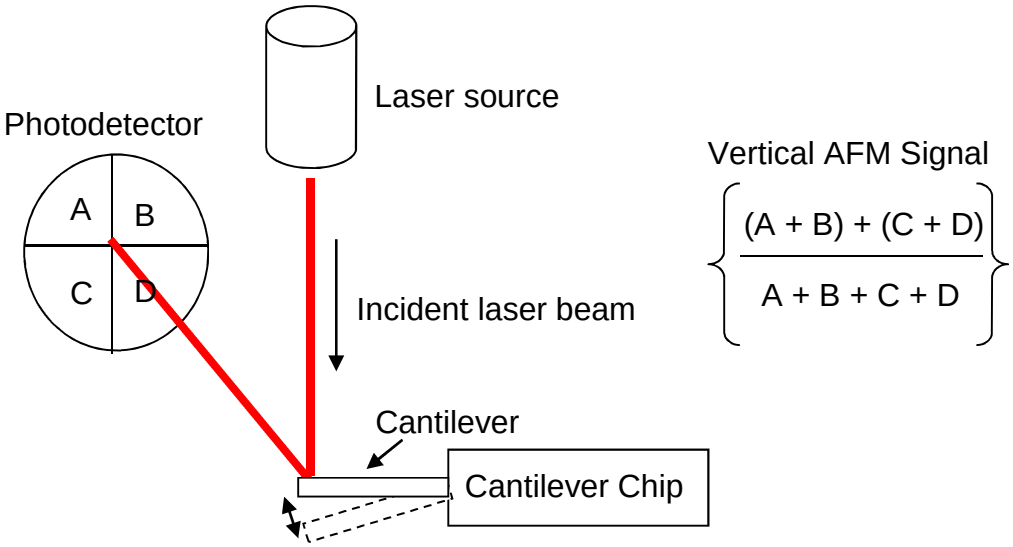

Figure. 3.12. Schematic of the reflected laser being received by the photodetector and the calculated vertical AFM response

The forces that contribute to the tip deflections include attractive van der Walls forces and repulsive electrostatic forces. The contribution of the two forces depends on the distance between the tip and sample.

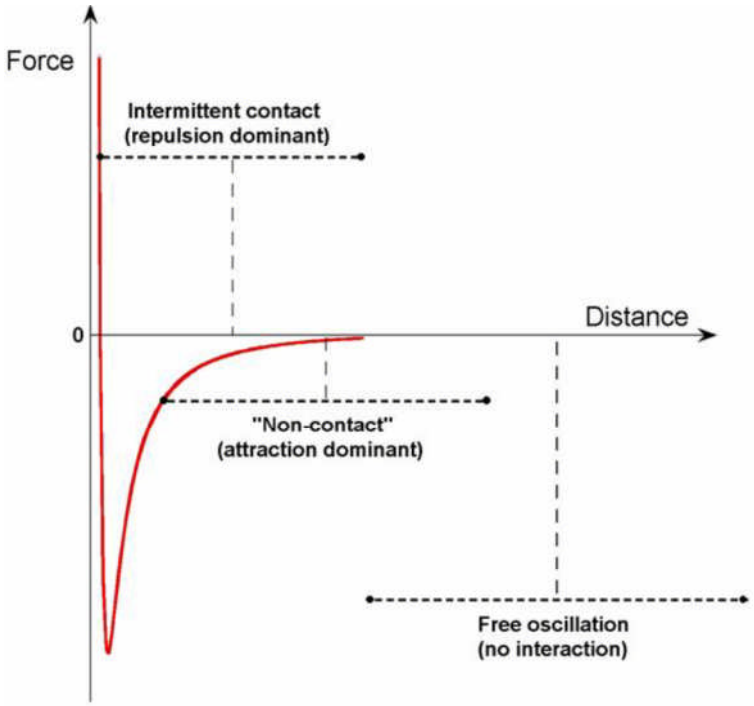

Figure. 3.13. Schematic of the tip – sample interaction forces contact and non – contact mode using atomic force microscopy (Agilent, 2011)

Generally when the tip is less than ~2 Å from the sample the repulsive forces dominate the contribution to the tip deflection. This mode of operation is known as *contact-mode*. When the tip is ~10 - 100 Å from the sample surface the attractive forces dominate. This mode of operation is known as *non-contact* mode.

In contact mode the tip is in constant contact with the sample surface where the repulsive contact force causes the cantilever to bend with changes in topography. A low spring constant in the tip is important to allow the tip to bend rather than damage the sample surface.

Generally in non-contact mode a tip with a higher spring constant is used which is vibrated near the surface of the sample, close to its resonant frequency. The spacing between the tip and sample is similar to the vibration amplitude of the tip therefore as the tip approaches the surface this is detected as a change in resonant frequency which provides sub-Angström resolution in the topography image. Again this feedback signal is used to maintain a constant tip to sample distance.

Another AFM mode of operation is referred to as *tapping mode* which is similar to non-contact mode except the vibrating cantilever tip just touches the sample surface.

Tapping mode has become the preferred mode of operation for imaging topography in ceramic thin films as it is less likely to cause damage to the sample or tip than contact mode as it eliminates lateral forces between the tip and sample. When compared to non-contact mode, larger scan sizes with greater variations in sample topography are possible.

A variation on the standard AFM technique is lateral force microscopy (LFM) which detects lateral deflections (twisting and bending) of the cantilever parallel to the plane of the surface. LFM is used for imaging in homogeneity in surface material as well as obtaining edge enhanced images of the surface. In the case of LFM the cantilever movement is detected by the photodetector, just as it is in vertical response AFM however, the lateral deflection is defined as:

$$\text{Lateral Response (LFM) Signal} = \left\{ \frac{(B + D) + (A + C)}{A + B + C + D} \right\}$$

from the four quadrants (A, B, C and D) of the photodetector, (refer to Figure. 3.12.)

3.2.8. Piezoresponse Force Microscopy

There are an increasing number of variations on the standard AFM one of which is piezoresponse force microscopy (PFM). PFM allows ferroelectric domains to be imaged and manipulated. PFM is a technique based on the converse piezoelectric effect (refer to section. 2.2.6) for a description of the converse piezoelectric effect) where a piezoelectric material expands or contracts upon an applied electric field. The scanning tip used in PFM is coated with a conductive material (Pt) to enhance the electrical contact between the film surface and the tip.

An ac voltage with a dc offset bias is applied to the tip. When the tip comes into contact with the films surface the piezoelectric response is measured from the deflection of the cantilever (as the grains/domains expand or contract with the applied electric field). To ensure a true piezoelectric response is measured, the selected frequency of the applied ac voltage is far from the resonant frequency of the cantilever to avoid driving the cantilever into the resonant frequency.

The resulting deflection of the tip is detected through the photodetector (described in AFM section 3.2.7) which is then demodulated using a lock-in amplifier, thus allowing topography to be imaged simultaneously. In AFM the photodetector is split into quadrants which allows lateral deflections (LFM and vertical deflections (standard AFM) to be detected. In the same way, the quadrants of the photodetector allow the piezoelectric response out-of-plane (vertical response PFM) and in-plane (lateral response PFM) to be imaged. If the laser reflection from the cantilever hits the centre of the photdetector the entire detectors output is 0V but with radial movements from centre the voltage output increases linearly.

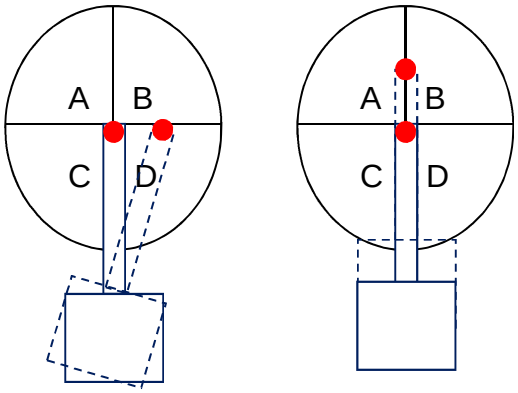

Figure. 3.14. Schematic of the cantilever movement with the photodetector represented by the circle divided into quadrants (A, B, C and D). Lateral deflections (left) are a result of torsional bending and vertical deflections (right) are a result of vertical displacements

$$\text{Vertical deflection} = \left\{ \frac{(A + B) + (C + D)}{A + B + C + D} \right\}$$

therefore positive and negative voltages describe positive and negative vertical displacements.

$$\text{Lateral deflection} = \left\{ \frac{(B + D) + (A + C)}{A + B + C + D} \right\}$$

therefore positive and negative voltages describe positive and negative twisting displacements.

If a polar direction in the film is orientated parallel to the electric field the resulting oscillating movements (from the piezoresponse) would be in-phase with the modulated electric field and if the polar direction is anti-parallel to the electric field the oscillating motion would be 180˚ out-of-phase. This phase information is used to image the piezoresponse which delineates regions of differing piezoresponse with a change in contrast.

3.2.9. AFM and PFM - Sample Preparation

The ceramic targets were not analysed using atomic force microscopy (AFM) or piezoresponse force microscopy (PFM) in this work therefore the discussion for sample preparation for AFM and PFM will be limited to thin films.

In this work the AFM analysis technique was used to image surface topography. This requires the film be placed flat on the sample stage to avoid a false topography map. To ensure the sample does not move when the

AFM tip touches the sample surface, the film was attached to the sample surface using double sided adhesive tape.

For PFM analysis the thin film was placed onto the sample stage and secured using conductive carbon adhesive tape. A metallic wire connecting the sample to ground is positioned and secured using a small drop of conducting silver glue. The wire supplies the voltage to the sample and the silver glue ensures conductivity around the circuit.

3.3. References

AGILENT TECHNOLOGIES. (2011). *AFM – Nanotechnology Measurements Division User Manual*. Santa Clara, USA: Agilent Technologies.

BIRKHOLZ, M. (2006). *Thin Film Analysis by X-Ray Scattering*. Weinheim: Wiley-VCH.

BRYDSON, R. (2007). Electron Energy-loss Spectroscopy and Energy Dispersive X-Ray Analysis. KIRKLAND, A., J. L. HUTCHINSON, eds. *Nanocharacterisation.* Cambridge: Royal Society of Chemistry.

CASTELLANO, R. N., L. G. FEINSTEIN. (1979). Ion-beam deposition of thin films of ferroelectric lead zirconate titanate (PZT). *J. Appl. Phys*. **50**(6), pp.4406-4411

CHRISEY, D. B., G. K. HUBLER. (1994). *Pulsed laser deposition of thin films*. Chichester New York: J. Wiley.

CRACIUN, F., P. VERARDI, M. DINESCU, G. GUIDARELLI G. (1999). Reactive pulsed laser deposition of piezoelectric and ferroelectric thin films. *Thin. Solid. Films*. **344**, pp.90-93

CULLITY, B. D. (2001). *Elements of X-Ray Diffraction*. 3rd Edition. London: Prentice-Hall International.

FEI COMPANY. (2010). *An introduction to electron microscopy* [online]. Oregon, USA: FEI. [Accessed 5 June 2011]. Available from: http://www.fei.com/uploadedFiles/Documents/Content/Introduction_to_EM_booklet_July_10.pdf

GOODHEW, P. J., J. HUMPHREYS, R. BEANLAND. (2001). *Electron Microscopy and Analysis*. 3rd Edition. London: Taylor and Francis.

KELSALL, R. W., I. W. HAMLEY, M. GEOGHEGAN. (2005). *Nanoscale Science & Technology*. Chichester: Wiley.

KRUPANIDHI, S. B., N. MAFFEI, M. SAYER, K. ELASSAL. (1983). rf planar magnetron sputtering and characterization of ferroelectric $Pb(ZrTi)O_3$. *J. Appl. Phys*. **54**(11), pp.6601-6609

LORETTO, M. H. (1994). *Electron Beam Analysis of Materials*. 2nd Edition. London: Chapman and Hall.

OHRING, M. (2002). *Materials science of thin films: deposition and structure*. 2nd Edition. New York: McGraw.

SURFACE. (2006). *Pulsed laser Deposition Excimer Laser Manual - TuiLaser*. Hückelhoven, Germany: Surface.

WILLIAMS, D. B., B. C. CARTER. (1996). *Transmission electron microscopy: A textbook for materials science*. New York: Plenum Press.

Chapter 4

Optimisation of Pulsed Laser Deposition Conditions for $BiFeO_3$ – $PbTiO_3$ Thin Films on PtSi Substrates

This chapter begins with a review of literature to date relating to $BiFeO_3$ – $PbTiO_3$ thin films. The reported effect of varying pulsed laser deposition conditions on the films structure and stoichiometry are also described.

The later part of this chapter looks at the effect of varying post anneal temperature on film structure and morphology and describes the optimum pulsed laser deposition conditions for $BiFeO_3$ – $PbTiO_3$ thin films on preferentially orientated $Pt/TiO_x/SiO_2/Si$ substrates (refer to page 50 for a discussion on substrate types and orientation). X-ray diffraction data was used to analyse the development of crystal structure as the post-anneal temperature was increased.

4.1. Background

In the past decade, ferroelectric research has seen an increased amount of publications relating to thin films due to their potential commercial applications. There are relatively few reports on the structural, electrical or magnetic properties of bismuth ferrite lead titanate ($xBiFeO_3$ - $(1-x)PbTiO_3$) thin films especially for thin films around the morphotropic phase boundary (MPB) (Chen, 2010), (Khan, 2007b), (Gupta, 2009), (Khan, 2008a), (Lui, 2008), (Sakamoto, 2006), (Singh, 2008), (Chen, 2011). The little research carried out on bismuth ferrite lead titanate thin films has centred around compositions lying within or around the MPB produced using a variety of processing techniques including chemical solution deposition, sol-gel synthesis and pulsed laser deposition.

This chapter as well as following chapters reports on two compositions either side of the MPB of $xBiFeO_3$ - $(1-x)PbTiO_3$, x = 0.6 and 0.7, due to the enhanced electrical properties shown in their bulk counterparts.

Singh reported on manganese doped bismuth ferrite lead titanate thin films of compositions around the morphotropic phase boundary, deposited on (111) orientated $Pt/TiO_x/SiO_2/Si$ substrates, by chemical solution deposition using the spin coating technique (Singh, 2008). Although the room temperature dielectric constant suggested that the films had reasonable insulation resistance, the ferroelectric measurements showed the presence of leaky hysteresis behaviour. Lui reported on the preparation of $xBiFeO_3$ - $(1-x)PbTiO_3$ thin films where x = 1 to 0.7 using sol-gel synthesis on $LaNiO_3/SiO_2/Si$ substrates (Lui, 2008). A rhombohedral to cubic phase transition for x = 0.9 was identified. Remnant polarization of $2P_r$ = 3.4 μCcm^{-2} and 4.1 μCcm^{-2} were reported for films where x = 0.2 and 0.3. Sakamoto reported on manganese doped, bismuth ferrite lead titanate thin films x = 0.5 to 0.9 prepared by chemical solution deposition on Pt/TiO_x/SiO2/Si substrates (Sakamoto, 2006). Good surface morphology was observed and all the films showed weak ferromagnetism at room temperature. For films of composition $0.7Bi(Fe_{0.95}Mn_{0.05})O_3 - 0.3PbTiO_3$ ferroelectric polarization electric field (P-E) hysteresis loops were observed, although some leakage components were included at room temperature. The electric resistivity of the

films was improved in the low temperature region and the remnant polarisation and coercive field of the films at -190 °C were approximately 50 μCcm^{-2} and 150 $kVcm^{-2}$.

A significant improvement in the electrical properties of $xBiFeO_3$ - $(1-x)PbTiO_3$ thin film was reported by Khan (Khan, 2007b) with the use of pulsed laser deposition (PLD) as the processing technique. Although measurements were carried out at -10°C to reduce the leakage current Khan reported good electrical properties with fully saturated hysteresis loops. The remnant polarisations $2P_r$ up to 100 μCcm^{-2} at a field amplitude of 820 $kVcm^{-1}$ and switchable polarisation up to 80 μCcm^{-2} at 375 $kVcm^{-1}$ for the $0.6BiFeO_3$ - $0.4PbTiO_3$ composition were reported.

Recently doping has been used in attempt to reduce the leakage current of bismuth ferrite lead titanate thin films and achieve fully saturate hysteresis loops. Chen (Chen, 2010) (Chen, 2011) reported on thin films deposited by pulsed laser deposition of $0.72Bi(_{Fe1-x}Ti_x)O_3$-$0.28PbTiO_3$ (x = 0 and 0.02) on $Pt/TiO_x/SiO_2/Si$ substrates. By B-site ionic substation of the Ti^{4+} for Fe^{3+} the ferroelectric and dielectric properties of the films were reported to be improved from that of the undoped composition. In both the doped and undoped films the preferential orientation was along the (001) tetragonal. Although P-E ferroelectric hysteresis loops were not completely saturated a large remnant polarization of 80 μCcm^{-2} was obtained in the doped films at room temperature.

4.2. Effect of Film Deposition Conditions

Film growth and quality are dependent on a few fundamental deposition conditions, namely the oxygen partial pressure, the substrate temperature, the deposition rate (which is referred to as the laser frequency) and the kinetic energy of the deposition flux known as laser fluence.

4.2.1. Substrate Temperature

The initial stages of deposition are extremely important as several problems may occur as a direct result of unsuitable substrate temperatures. If the substrate temperature is too high there is an increased possibility that the substrate and deposited film may chemically interact with one another and/or substrate degradation may occur. High substrate temperatures may also promote bismuth rich phases in $BiFeO_3$ - $PbTiO_3$ films due to the inherent volatility of lead at high temperature. However if the substrate temperature is too low, unbound deposited atoms may re-evapourate from the surface of the substrate resulting in non-stoichiometric films. Substrate temperature also has a profound effect on the growth mechanism of the film as deposited material may nucleate into clusters, be consumed by existing clusters or be trapped by substrate defects.

Lewis described three possible growth modes of thin films (Lewis, 1978):

1) Volmer-Weber Island Formation occurs due to the cohesive energy of the atoms within the film being greater than that between the atoms of the film and substrate. This results in the formation of islands on the surface of the substrate.

2) Layer-by-Layer (Frank-van der Merwe) occurs when the cohesive energy between the atoms of the film and atoms of the substrate is greater than the cohesive energy of the film atoms. This results in the

growth of one monolayer at the time and resulting in the formation of an epitaxial film. The cohesive energy will decrease as each film layer is added.

3) Mixed growth occurs when the binding energy is energetically over-ridden by factors such as lattice mismatch and strain. This results in the first deposited layer (monolayer) forming a uniform, often epitaxial, layer. However due to strains and mismatch between the substrate and deposited film, it then becomes favorable for island formation to occur on top of the uniform monolayer.

Very small variations in substrate temperature can result in non-stoichiometric films, with a large thickness variation and possible chemical interaction with the substrate. However if the chosen substrate temperature is appropriate for the system, it can be used to induce different film orientations and control microstructural morphology.

4.2.2. Laser Pulse Frequency Rate

The laser pulse frequency rate is the rate at which the laser pulse is emitted from the laser source, for instance 5 Hz. Generally too high of a laser pulse frequency rate does not allow enough time for film relaxation to occur, resulting in film degradation. If the deposition rate is too low the deposition runs will be unnecessarily long.

4.2.3. Oxygen Deposition Pressure

The gas pressure during deposition is reported to effect the stoichiometry, microstructure as well as electrical properties of deposited films. It has been reported that low oxygen deposition pressures can lead to re-evaporation of lead at the surface in lead based systems. Higher oxygen deposition pressures can increase the striking coefficient of ablated material reducing

the chance of lead re-evaporation. In addition a higher oxygen deposition pressure will reduce the oxygen vacancies within the film improving film quality. However too high oxygen deposition pressures will increase the time taken for the ablated material to reach the substrate surface and therefore increase the scattering within the plume. This results in non-stoichiometric films.

4.2.4. Laser Fluence

A high laser fluence produces similar effects to raising the substrate temperature and therefore influences properties such as crystal structure and film. The laser energy is closely related to the substrate temperature, with literature suggesting that a higher laser fluence allows for reduced substrate temperatures.

Calculations for gold deposited at 300 K (Gilmore, 1992) show that low kinetic energies (<10 eV) favour the Volmer-Webber island formation of the film whilst at high kinetic energies the Frank-van der Merwe layer by layer growth is preferred. For this system substrate and film interaction was observed in the form of ion mixing, whereby ions from the substrate were detected in the film and vice versa. This effect appears to scale with impact energy.

Another effect that may be observed with high laser fluence is that of high energy ion bombardment, in which a ballistic collision results in the displacement of substrate atoms. This effect is also dependent on the atomic mass difference of the ablated material and atomic mass of the substrate since the energy transfer during the collision will depend upon the mass difference between the atoms involved in the collision (Brice, 1989). However low laser fluence may result in less compaction within the film resulting in physical defects within the structure.

Although higher laser fluence would allow for reduced substrate temperature, if the laser fluence is too high it may result in ion mixing at the interface and/or ballistic collision displacement of substrate ions. This would have an

impact on the morphology and structure of the film as well as inducing unknown stresses at the interface.

4.3. Optimum Processing Conditions

A Tui Thin Film Star 248 nm KrF laser system (TuiLaser AG, Munich, Germany) incorporated into a Surface PLD Workstation (Surface AG, Hucklehoven, Germany) was used to deposit material onto the various substrates. Two different substrates were used for the experiments; (111) orientated $Pt/TiO_x/SiO_2/Si$ and polycrystalline $Pt/TiO_x/SiO_2/Si$. Khan reported on the optimum conditions for the deposition of $BiFeO_3$ - $PbTiO_3$ on $Pt/TiO_x/SiO_2/Si$ substrates (Khan, 2008b). These conditions were employed and analysed using x-ray diffraction as well as scanning electron microscopy to confirm the quality of the films. On analysis of the deposited films under the processing conditions reported by (Khan, 2008b) it can be confirmed that these condition produce good quality, single phase films and were therefore employed in part to produce the films presented in this chapter.

All films were deposited at a frequency of 5 Hz, substrate temperature of 565 °C with an oxygen partial pressure of 75 mTorr. A lower laser fluence of 2.3 Jcm^{-2} was used to avoid ion mixing at the interface and reduce the possibility of ballistic collision.

Laser Fluence at target = Laser energy at target / area

Laser Fluence at target = 45 mJ / 0.02 cm^2 = 2.3 Jcm^{-2}

4.3.1. Post Deposition Anneal Temperature

The majority of pulsed laser deposition regimes are followed by a post anneal stage under an increased oxygen pressure. This type of post anneal stage increases the chance of oxygenation by the process of diffusion and gas exchange. The anneal temperature and pressure are selected to improve crystallisation and mis-orientation within the deposited film.

To analyse the effect of post deposition anneal temperature on the structure of $xBiFeO_3 – (1\text{-}x)PbTiO_3$ films deposited by pulsed laser deposition all films were deposited under the same deposition conditions for the same

composition, $0.7BiFeO_3 – 0.3PbTiO_3$. All films were ~ 460 nm thick which was measured from the films cross sections using scanning electron microscopy. X-ray analysis data reveals the formation of a perovskite, polycrystalline structure. The post deposition anneal temperatures analysed in this section range from 500 - 700 °C, all held at temperature for 30 minutes and then reduced by 15 °C / minute. The x-ray diffraction traces for the films prepared at different post anneal temperature are shown in Figure. 4.1.

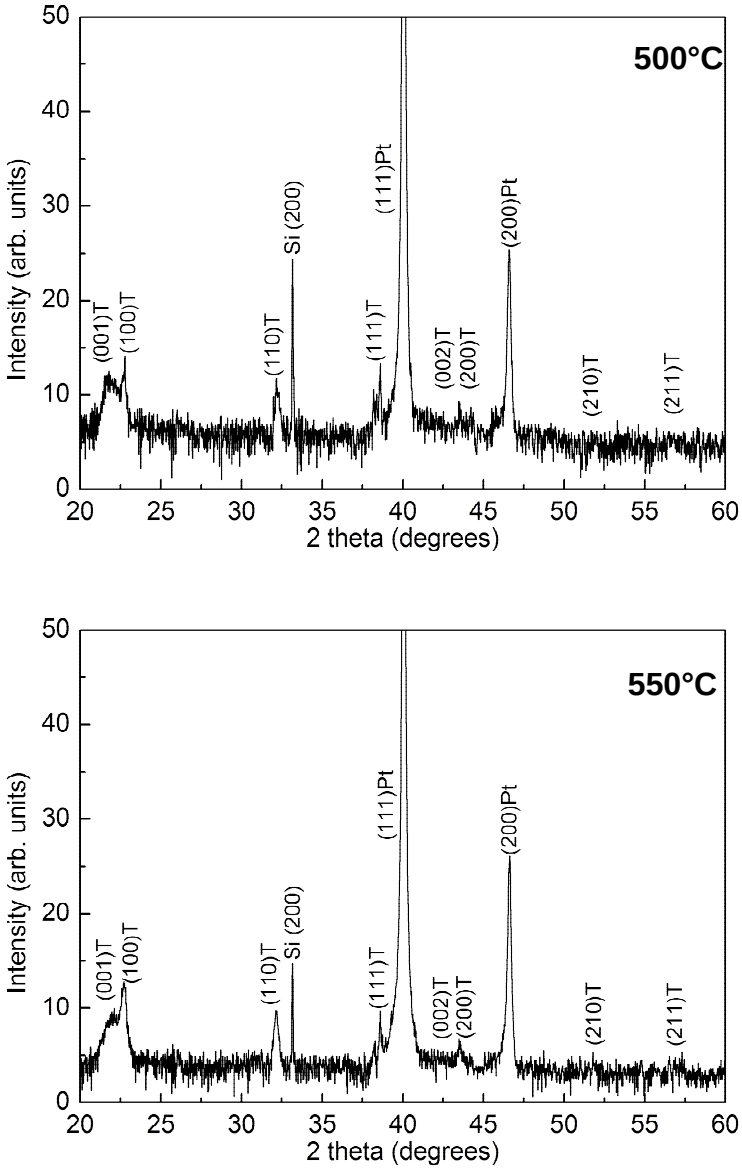

Figure. 4.1. Effect of post anneal deposition temperature on XRD traces for $0.7BiFeO_3$ - $0.3PbTiO_3$. R represents rhombohedral phase and T represents tetragonal phase.

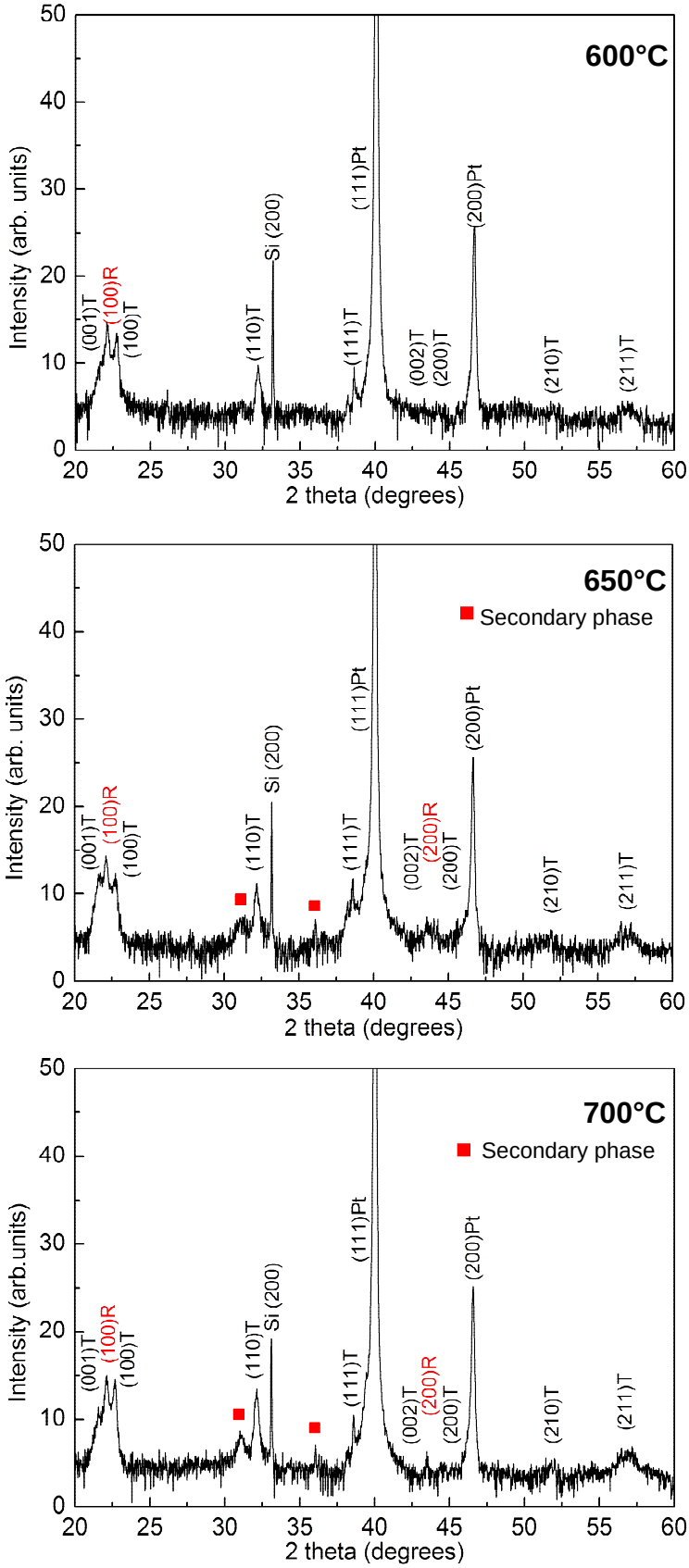

Figure. 4.1. Effect of post anneal deposition temperature on XRD traces for $0.7BiFeO_3$ - $0.3PbTiO_3$. R represents rhombohedral phase and T represents tetragonal phase.

At a post deposition anneal temperature of 500 °C, a single phase, polycrystalline structure $0.7BiFeO_3 – 0.3PbTiO_3$ was observed. The presence of the (001) and (100) peaks at approximately 21.6° 2θ and 22.7° 2θ is indicative of the $BiFeO_3 – PbTiO_3$ tetragonal structure. As the post deposition anneal temperature is increased to 550 °C the film remains single phase $BiFeO_3 – PbTiO_3$, of tetragonal structure. However the $(100)_T$ becomes more prominent over the $(001)_T$ peak which indicates that the post anneal deposition stage is increasing the crystallinity and preferred texture within the film. At an increased post deposition anneal temperature of 600 °C another peak appears between the $(100)_T$ and $(001)_T$ tetragonal peaks at approximately 22.1° 2θ. This peak is more intense than the (100)T and (001)T and can be indexed as the (100)R rhombohedral BiFeO3 – PbTiO3 phase. However using the (100)R peak to calculate the expected d-spacing from the polycrystalline $BiFeO_3 – PbTiO_3$ film it can be confirmed that all the other peaks can be indexed as the tetragonal phase (see Table. 4.1). Therefore the rhombohedral phase present within the films is preferentially (100) orientated.

Table. 4.1. Table of the expected (in black) 2θ values for $BiFeO_3 – PbTiO_3$ tetragonal and rhombohedral phases calculated from the measured (in red) (001) and (100) tetragonal peaks and the (100) rhombohedral peaks shown in Figure 4.1 XRD traces.

hkl values	**2θ (°)**	**2θ (°)**
001 **(measured using x-ray diffractogram)**	21.63	-
100 **(measured using x-ray diffractogram)**	22.71	22.12
110 **(calculated from measured values)**	32.33	31.48
111 **(calculated from measured values)**	39.23	38.81
002 **(calculated from measured values)**	44.08	-
200 **(calculated from measured values)**	46.38	45.12

At the morphotropic phase boundary (MPB) for $xBiFeO_3 – (x-1)PbTiO_3$, where x ~ 0.7, the 18 % strain within the unit cell structure forces the unit cell to undergo a structural transformation from tetragonal to rhombohedral to facilitate the strain. This gives rise to a morphotropic phase region in which the tetragonal and rhombohedral phase co-exist. As the $0.7BiFeO_3 – 0.3PbTiO_3$ composition used in these experiments is located on the MPB between the tetragonal P4mm and rhombohedral R3c phase, it is not unexpected that the tetragonal and rhombohedral phase to co-exist in the same film to produce a mixed phase film.

Table. 4.2 compares the unit cell parameters of platinum to the rhombohedral and tetragonal phases present within the films. The cubic platinum unit cell parameters used in Table. 4.2 have been obtained from the standard JCPDS file (01-087-0644) and the unit cell parameters of the two $BiFeO_3 – PbTiO_3$ phases have been experimentally measured using x-ray analysis (the XRD traces are shown in Figure. 4.1).

Table. 4.2. Comparison of unit cell parameters of the platinum substrate and the measure unit cell parameters of the tetragonal and rhombohedral $BiFeO_3 – PbTiO_3$ phases.

Phase	**a-axis (Å)**	**c-axis (Å)**
Platinum cubic (substrate)	4.028	4.028
Tetragonal $BiFeO_3 – PbTiO_3$	3.911	4.104
Δ Tetragonal and platinum =	*- 0.117*	*0.076*
Rhombohedral $BiFeO_3 – PbTiO_3$	4.014	4.014
Δ Rhombohedral and platinum =	*- 0.014*	*- 0.014*

The unit cell parameters of the rhombohedral phase are more closely matched to that of the platinum in comparison to the tetragonal phase. This would further encourage a transition from the tetragonal to rhombohedral

phase to accommodate the strain, thus providing further explanation to the existence of the mixed phase tetragonal-rhombohedral films.

If grain growth or thermal expansion of the platinised silicon substrates has occurred at the higher post deposition anneal temperatures this would increase the possibility of a tetragonal to rhombohedral structural transformation. At increased temperatures the difference between the unit cell parameters of the platinum and the unit cell parameters of the $0.7BiFeO_3 – 0.3PbTiO_3$ tetragonal phase would increase even further. This is the most probable explanation as to why the films annealed at higher post anneal temperatures contain a higher percentage of rhombohedral phase than those annealed at the lower temperatures.

In addition to the rhombohedral phase (present within the films processed at higher post deposition anneal temperatures), two extra peaks were observed at approximately 30.03° 2θ and 36.04° 2θ which are associated with a secondary phase. At the higher anneal temperatures of 650 - 700 °C, the mixed rhombohedral tetragonal phase remains present and the intensity of the peaks associated with the secondary phase increases in intensity.

As the films have a higher $BiFeO_3$ composition than $PbTiO_3$ it is more likely that the secondary phase is associated with bismuth or iron rather than lead or titanium. Possible lead and titanium based compounds that may be present within the film are lead oxide (PbO) or one of the three mineral forms of titanium dioxide (TiO_2); rutile, anatase and brookite. Analysis of standard JCPDS files for these compounds confirm that the peak at 30.9° 2θ associated with a secondary phase is not related to the most probable lead or titanium based compounds. On comparison of standard JCPDS files several possible compounds have been identified for the secondary phase peak at 30.9° 2θ: $Bi_2Fe_4O_9$ (JCPDS 00-025-0090), Fe_3O_4 (JCPDS 01-089-0950) and Fe_2O_3 (JCPDS 00-039-1346).

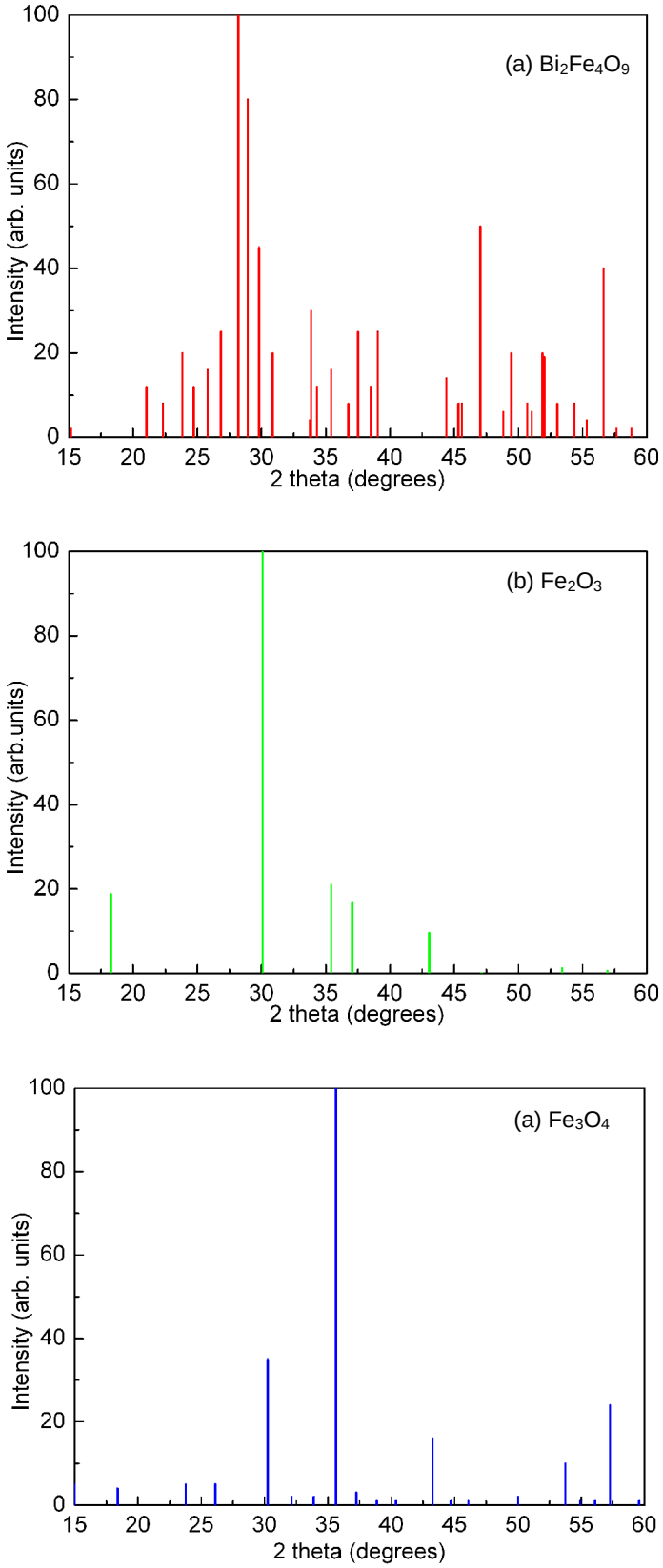

Figure. 4.2. Simulated XRD traces for (a) $Bi_2Fe_4O_9$, (b) Fe_2O_3 and (c) Fe_3O_4.

$Bi_2Fe_4O_9$ (JCPDS: 00-025-0090) has a (002) peak at 29.8° 2θ which is of lower intensity than the (121) and (211) at 2θ 28.2° and 28.9°. Therefore if the peak seen at 30.9° 2θ is associate with $Bi_2Fe_4O_9$ it must be (002) orientated and would therefore be accompanied by the (001) peak at 14.77° 2θ which is absent.

Fe_2O_3 (JCPDS: 00-039-1346) has a (220) peak at 30.2° 2θ which is lower intensity than the (311) peak at 35.6° 2θ. Again if the Fe_2O_3 structure is (220) orientated it would be expected that the (110) peak at 15.0° 2θ also be present, which it is not.

The closet match to the peak at 30.9° 2θ would be cubic phase Fe_3O_4 (JCPDS: 01-089-0950). The most intense peak for Fe_3O_4 is the (220) at 30.1° 2θ with the second being the (311) at 35.4° 2θ. Fig 4.1 shows the formation of a peak at approximately 36.0° 2θ when the peak at 30.9° 2θ is present. As both of these peaks appear at the same time it is probable that they are associated with the same secondary phase. The most likely candidate for the second phase is that of Fe_3O_4 as both the two most intense peaks appear within the films at the elevated post deposition anneal temperatures, where bismuth deficient phases may be expected.

Results presented in Figure 4.1 show that a lower post deposition anneal temperature produces single phase $xBiFeO_3$ – $(1\text{-}x)PbTiO_3$ films with reduced crystallinity. An increased post deposition anneal temperature appears to a produces a bismuth deficient secondary phase. Taking these results into account, the optimum anneal temperature appears to be 600 °C, which produced phase pure $xBiFeO_3$ – $(1\text{-}x)PbTiO_3$ films of mixed phase, rhombohedral/tetragonal, with a preferred (100) orientation. 600 °C was therefore chosen as the post deposition anneal temperature for all films presented in this chapter.

4.4. Conclusion

The optimisation of pulsed laser deposition conditions for $BiFeO_3$ – $PbTiO_3$ thin films around the MPB on $Pt/TiO_x/SiO_2/Si$ are reported in this chapter. Good quality, pure phase films were produced by pulsed laser deposition using the following processing conditions; pulsed frequency of 5 Hz, substrate temperature of 565 °C, substrate target distance of 5 cm, laser fluence of 2.3 Jcm^{-2} and an oxygen partial pressure of 75 mTorr. X-ray analysis was carried out on films with varying post anneal temperatures. Films annealed at 500 – 550 °C for 30 minutes produced single phase polycrystalline films. An increased anneal temperature of 600 °C produced a rhombohedral – tetragonal polycrystalline film with {100} tetragonal and (100) rhombohedral preferential orientation. At post deposition anneal temperatures between 650 – 700 °C, secondary phases are present within the films which have been indexed as Fe_3O_4. The optimum post deposition anneal temperature appears to be 600 °C which produces phase pure $BiFeO_3$ – $PbTiO_3$ tetragonal – rhombohedral films with increased crystallinity and (100) preferred orientation.

4.5. References

BRICE, D. K., J. Y. TSAO, S. T. PICRAUX. (1989). Molecular dynamics simulations of thin film growth on Ag(100) and (111) with energetic Ag atoms. *Nucl. Inst. And. Meth. Structured Materials.* **B44**(68), pp.301-310.

CHEN, L., W. REN, W. ZHU, Z. G. YE, P. SHI, et al. (2010). Improved dielectric and ferroelectric properties in Ti-doped $BiFeO_3$-$PbTiO_3$ thin films prepared by pulsed laser deposition. *Thin. Solid. Films.* **518**(6), pp.1637-1640

CHEN, L., W. REN, W. ZHU, Z. G. YE, P. SHI, et al. (2011). Structural, dielectric and ferroelectric properties of Ti-modified $0.72BiFeO_3$ - $0.28PbTiO_3$ thin films prepared by pulsed laser deposition. *Ferroelectrics.* **410**(1), pp.42-49

GILMORE, C. M., J. A. SPRAGUE. (1992). Molecular dynamics simulations of thin film growth on Ag(100) and (111) with energetic Ag atoms. *Nanostructured Materials.* **2**(3), pp.301-310

GUPTA, S., A. GARG, D. C. AGRAWAL, S. SHUVRAJYOTI, D. PANDEY. (2009). Structural changes and ferroelectric properties of $BiFeO_3$-$PbTiO_3$ thin films grown via a chemical multilayer deposition method. *J. Appl. Phys.* **105**(1), pp.014101

KHAN, M. A., T. P. COMYN, A. J. BELL. (2007a). Ferroelectric BiFeO3-PbTiO3 thin films on Pt/Si substrates. *Ultrasonics, Ferroelectrics and Frequency Control, IEEE Transactions.* **54**, pp.2583.

KHAN, M.A., T. P. COMYN, A. J. BELL. (2007b). Large remanent polarization in ferroelectric BiFeO3-PbTiO3 thin films on Pt/Si substrates. *Appl. Phys. Lett.* **91**(3), pp.032901.

KHAN, M. A., T. P. COMYN, A. J. BELL. (2008a). Growth and characterization of tetragonal bismuth ferrite-lead titanate thin films. *Acta Mater*. **56**(9), pp.2110.

KHAN, M. A. (2008b). *Preparation and properties of bismuth ferrite lead titanate thin films prepared by pulsed laser deposition*. PhD thesis, University of Leeds.

LEWIS, B., J. C. ANDERSON. (1978). *Nucleation and Growth of Thin Films*. New York: Academic Press.

LUI, H., Y. SUN, X. WANG. (2008). Study of the electrical properties of $PbTiO_3$- $BiFeO_3$ multilayer film structure. *J. Phys. D.* **41**, pp.095302-095307

SAKAMOTO, W., H. YAMAZAKI, A. IWATA, T. SHIMURA, T. YOGO. (2006). Synthesis and Characterization of $BiFeO_3$-$PbTiO_3$ thin films through Metalorganic Precursor Solution. *Jpn. J. Appl. Phys.* **45**(9B), pp.7315-7320

SINGH, V. R., S. KAR, A. GARG. (2008). Synthesis and characterization of solution processed $BiFeO_3$-$PbTiO_3$ thin films. *Indian J Eng Mater Sci.* **15**, pp.104-106

Chapter 5

Characterisation as a Function of Film Thickness, Substrate Type and Composition of $BiFeO_3$–$PbTiO_3$ Films on Polycrystalline and (111) Orientated PtSi Substrates

This chapter discusses the structural and electrical properties of bismuth ferrite lead titanate $xBiFeO_3$ – $(1-x)PbTiO_3$ films deposited on preferentially oriented platinised silicon and (111) orientated platinised silicon ($Pt/TiO_x/SiO_2/Si$) substrates (refer to page 51 for a description of substrates). This chapter focuses on two film compositions either side of the MPB of $xBiFeO_3$ - $(1-x)PbTiO_3$, x = 0.6 and 0.7, due to the enhanced electrical properties shown in their bulk counterparts.

Compositions around the morphotropic phase boundary (MPB) of the $xBiFeO_3$ – $(1-x)PbTiO_3$ (Khan, 2008a) (Khan, 2007a), (Khan, 2008b) solid solution are reported to offer high switchable polarizations and temperature stability (Khan 2007b) and are therefore of interest for commercial applications. It is also of interest to identify materials in which polarization and magnetization are strongly coupled at room temperature (whereby they can be strongly influenced by an applied field or the polarization by a magnetic field) as this would lead to developments in spintronic devices for sensing, data storage and signal processing. The exploitation of such devices requires a greater understanding of bismuth ferrite lead titanate film orientation and structure, since the electrical and magnetic properties of electroceramic thin films are directly linked to the degree of film orientation and overall structural properties. Therefore two compositions either side of the MPB form the focus of this work; $0.6BiFeO_3$ - $0.4PbTiO_3$ and $0.7BiFeO_3$ - $0.3PbTiO_3$.

The initial part of the chapter reports on existing literature relating to the effect of varying film thickness on the structure and morphology of various ferroelectric thin film materials.

The later part of the chapter looks at depositing different composition of $BiFeO_3$ – $PbTiO_3$ with two different space groups (R3c and P4mm), onto

preferentially orientated $Pt/TiO_x/SiO_2/Si$ substrates as well as (111) orientated $Pt/TiO_x/SiO_2/Si$ substrates. This allows the structural relationship between substrate and deposited film to be explored in greater depth. It is well reported that the orientation of the substrate influences the orientation of the deposited film, however this effect decreases as the thickness of the film is increased. Therefore analysis has been carried out on deposited films of various thicknesses. The effect of thickness on structural properties has been explored in great depth.

X-ray analysis, atomic force microscopy (AFM), scanning electron microscopy (SEM) and transmission electron microscopy (TEM) have been employed to explore the crystal structure and growth of the films. The piezoelectric nature of the films has been analysed using piezoresponse force microscopy (PFM).

5.1. Background - Effect of Film Thickness

$xBiFeO_3$ - $(1-x)PbTiO_3$ thin films have not received as much interest as their bulk counterpart and little work has been published on the effect of thickness on its structural properties. However work has been published on the $BiFeO_3$ thin films and the effect on thickness but this is predominantly on epitaxial thin films (Tyholdt, 2007), (Zhu, 2008).

Yakovlev reported on the effect of thickness of $BiFeO_3$ thin films on $Pt/TiO_x/SiO_2/Si$ substrates prepared by chemical solution deposition (Yakovlev, 2005). The films range in thickness from 50-300 nm. From atomic force microscopy and x-ray analysis it was found that the thinner films provide a smoother surface with a finer grain size and all films, regardless of thickness, were preferentially (100) orientated.

Zhong reported on the effect of thickness of $BiFeO_3$ thin films on $Pt/TiO_x/SiO_2/Si$ substrates prepared by spin coating (Zhong, 2008). X-ray analysis revealed that all films were of a randomly orientated polycrystalline structure; with the peak intensity regularly increases with increasing thickness. However a secondary phase, $Bi_2Fe_4O_9$, was detected at the electrode-film interface which was only seen in the thinnest samples.

Although a limited amount of work has been carried out on the effect of thickness on the structure of $BiFeO_3$ thin films, the commercially used PZT has been covered to a greater extent (Nagarajan, 1999).

Lian reported on PZT thin films prepared by sol-gel synthesis with thickness ranging from 0.5-2 µm (Lian, 2000). X-ray diffraction analysis revealed two different crystallographic orientations. Some films had a preferred (111) orientation and others had a preferred (100) orientation. SEM micrographs showed that both orientations provide well aligned columnar grains with no dependence of grain size on film thickness. However the (111) orientated films were more uniform with smaller grain size than the (100) preferred orientation.

Kim reported on the thickness dependence of thin films on the morphotropic phase boundary composition (52:48) of PZT (Kim, 2002). The films were deposited by pulsed laser deposition onto (111) orientated $Pt/TiO_x/SiO_2/Si$ at

500 °C and post anneal at 650 °C in oxygen atmosphere with thickness ranging from 0.4 - 6 µm. X-ray analysis was used to analyse crystallinity in the films. The variation of relative peak intensity was quantified in terms of an orientation parameter α_{hkl} calculated from the relative heights of the (100), (110) and (111) reflections.

At 0.4 - 1.5 µm the films were preferentially (111) orientated, with the (111) intensity decreasing with increasing thickness. Kim concludes that the lattice parameter of Pt (111) matching closely with that of the PZT (111). As the thickness is increased the (110) reflection increases. Above the film thickness of 3 µm the growth rate of relative intensities of the (110) and (100) saturates and all relative intensities do not show significant changes. SEM analysis shows that with increasing film thickness, surface roughness and grain size increased.

5.2. Characterisation of $xBiFeO_3 – (1-x)PbTiO_3$ Thin Films as a Function of Thickness

This section reports on the structural characterisation of pulsed laser deposited films of $BiFeO_3 – (1-x)PbTiO_3$, where x = 0.6 and 0.7, onto preferentially orientated and (111) orientated $Pt/TiO_x/SiO_2/Si$ substrates, as a function of thickness. This section is divided into 4 sub-sections;

- X-ray Diffraction of $xBiFeO_3 – (1-x)PbTiO_3$ (where x = 0.6 and 0.7) Films on Preferentially Orientated Pt Substrates
- X-ray Diffraction of $0.7BiFeO_3 – 0.3PbTiO_3$ films on (111) orientated Pt substrates
- Microstructure of Deposited Films – AFM and SEM
- Piezoelectric Response
- TEM Analysis: Interdiffusion at Substrate – Film Interface

5.2.1. X-ray Diffraction of $xBiFeO_3 – (1-x)PbTiO_3$ (where x = 0.6 and 0.7) Films on Preferentially Orientated Pt Substrates

This section discusses the characterisation from x-ray diffraction analysis of $xBiFeO_3 – (1-x)PbTiO_3$ thin films on preferentially orientated $Pt/TiO_2/SiO_2/Si$ substrates. Two different film compositions are discussed within this section starting with $0.6BiFeO_3 – 0.4PbTiO_3$ films (section 5.2.1.1.) followed by $0.7BiFeO_3 – 0.3PbTiO_3$ films (section 5.2.1.2.)

5.2.1.1. XRD: $0.6BiFeO_3 – 0.4PbTiO_3$ pulsed laser deposited films

Figure. 5.1 shows x-ray diffraction patterns of $0.6BiFeO_3 – 0.4PbTiO_3$ films on preferentially orientated $Pt/TiO_2/SiO_2/Si$ substrates. The x-ray diffraction patterns indicate preferential orientation of the deposited films, however to accurately index the peaks and calculate the d-spacing's, peak profile fittings have been carried out using WinPlotR which is part of the Full Prof Suite Software package. Figure. 5.2 shows the peak profile fittings between 18 –

24° 2θ for the various film thicknesses, which is the range the preferential orientation appears to be.

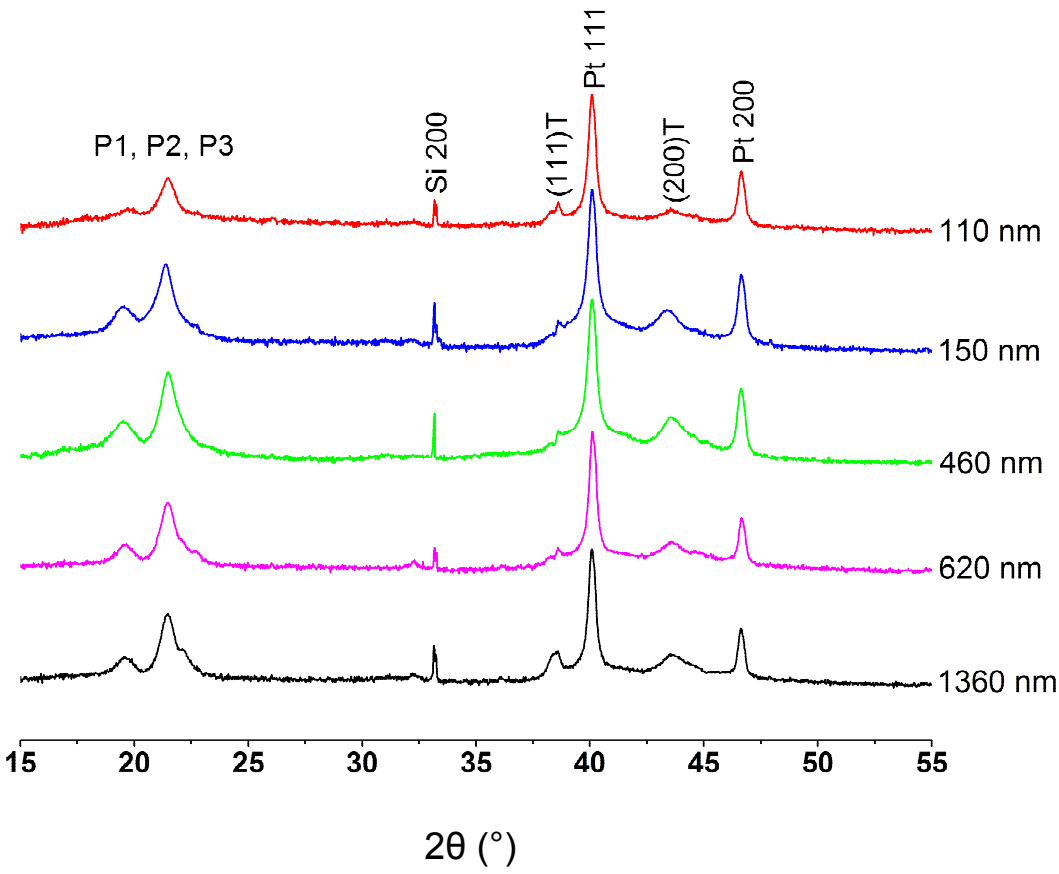

Figure. 5.1. Effect of thickness on XRD traces for $0.6BiFeO_3 – 0.4PbTiO_3$ films on preferentially orientated $Pt/TiO_x/SiO_2/Si$ substrates.

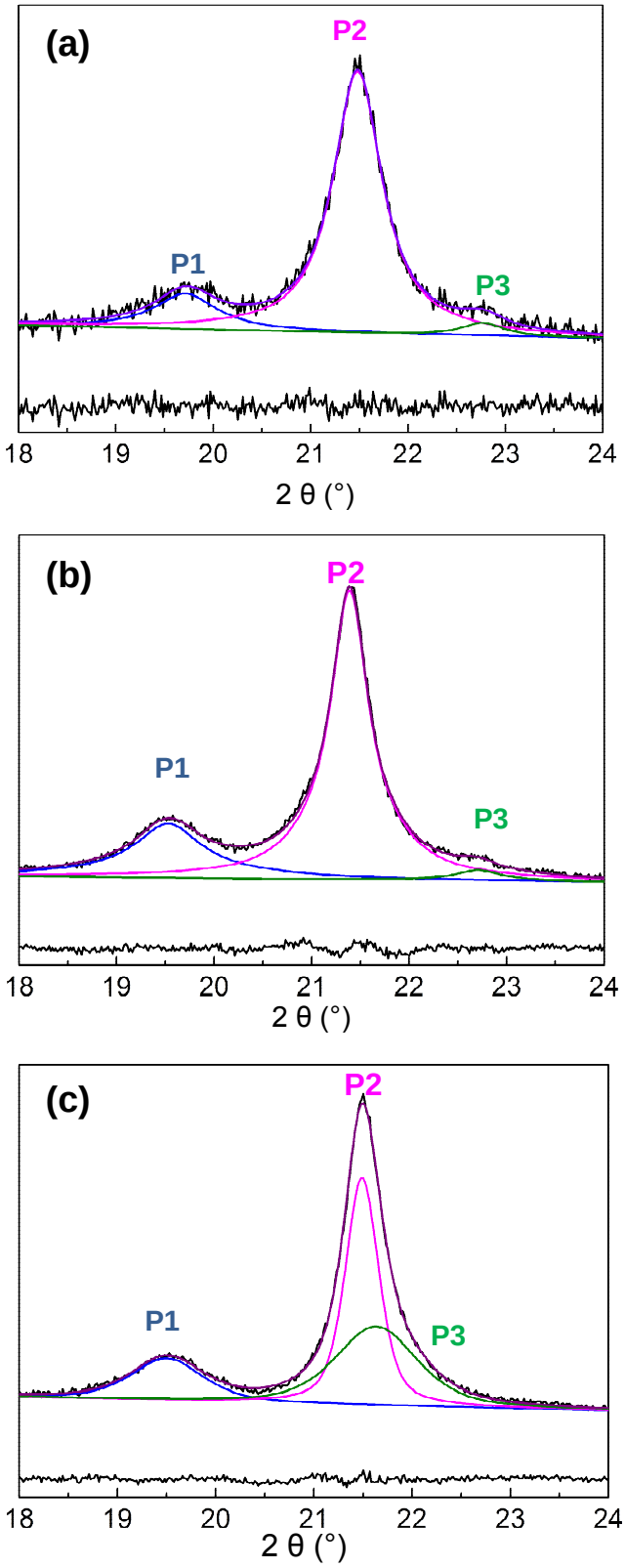

Figure. 5.2. X-ray peak profile fitting between 18 – 24° 2θ for $0.6BiFeO_3$ - $0.4PbTiO_3$ films of thickness a) 110 nm, b) 150 nm, c) 460 nm. P1, P2 and P3 indicate the three peaks identified.

NOTE: P2 has been indexed as the (001) for the $0.6BiFeO_3$ - $0.4PbTiO_3$ films and P3 has been indexed as the (100) for the $0.6BiFeO_3$ - $0.4PbTiO_3$ films. The intensity of P1 decreases with increasing thickness and has been indexed as a secondary phase at the substrate – film interface.

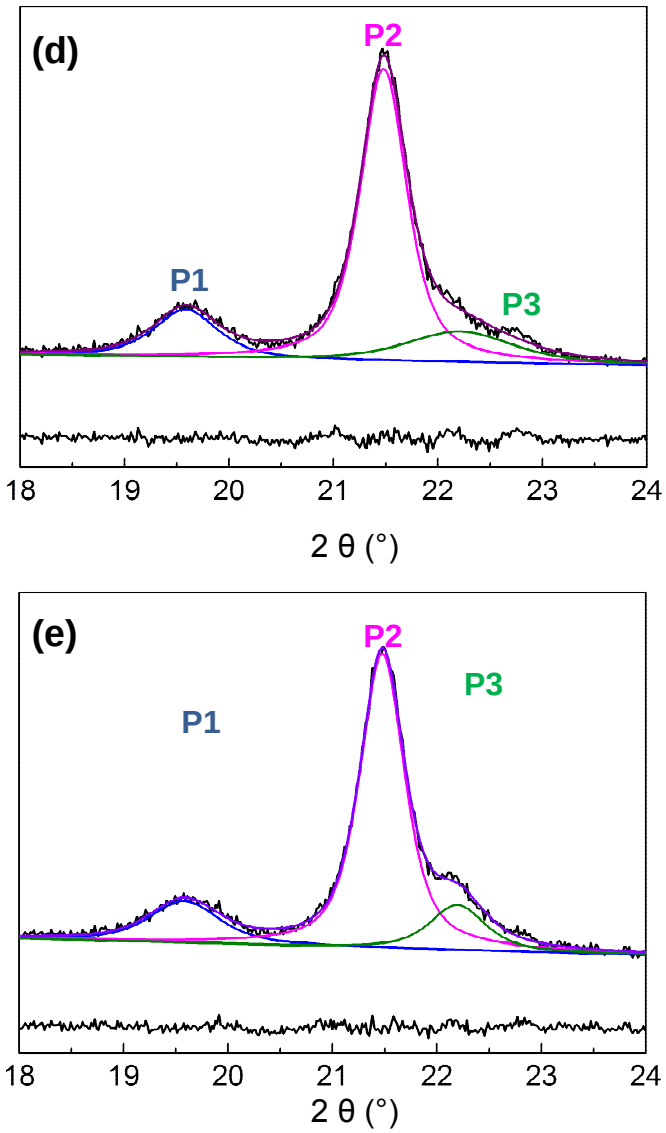

Figure. 5.2. X-ray peak profile fitting between 18 – 24° 2θ for $0.6BiFeO_3$ - $0.4PbTiO_3$ films of thickness d) 620 nm, e) 1360 nm. P1, P2 and P3 indicate the three peaks identified.

Three peaks have identified in the region the preferential orientation appears to be. Theses peaks have been labelled P1, P2 and P3. From the peak profile fits the corresponding d-spacing's and peak heights have been measured for the various film thicknesses and are shown in Table. 5.1.

NOTE: P2 has been indexed as the (001) for the $0.6BiFeO_3$ - $0.4PbTiO_3$ films and P3 has been indexed as the (100) for the $0.6BiFeO_3$ - $0.4PbTiO_3$ films. The intensity of P1 decreases with increasing thickness and has been indexed as a secondary phase at the substrate – film interface.

Table. 5.1. The measured d-spacing's of the three peaks identified in the peak profile fittings for $0.6BiFeO_3 – 0.4PbTiO_3$ films using WinPlotR with the corresponding peak heights.

Film Thickness (nm)	d-spacing P1 (Å)	d-spacing P2 (Å)	d-spacing P3 (Å)	Height P1	Height P2	Height P3
110	4.50	4.14	3.90	0.12	0.80	0.07
150	4.54	4.15	3.92	0.16	0.78	0.06
460	4.55	4.13	4.10	0.11	0.79	0.10
620	4.53	4.13	4.00	0.12	0.79	0.08
1360	4.53	4.13	4.00	0.10	0.72	0.17

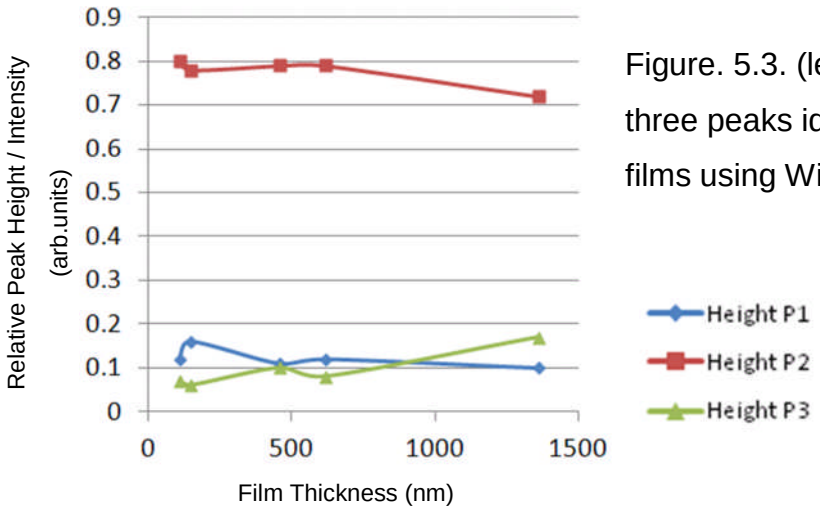

Figure. 5.3. (left) A graph to represent the relative peak height / intensity of three peaks identified in the peak profile fittings for $0.6BiFeO_3 – 0.4PbTiO_3$ films using WinPlotR, as a function of film thickness.

NOTE: P2 has been indexed as the (001) for the $0.6BiFeO_3$ - $0.4PbTiO_3$ films and P3 has been indexed as the (100) for the $0.6BiFeO_3$ - $0.4PbTiO_3$ films. The intensity of P1 decreases with increasing thickness and has been indexed as a secondary phase at the substrate – film interface.

X-ray diffraction patterns of 110 nm $0.6BiFeO_3$ – $0.4PbTiO_3$ films on preferentially oreientaed $Pt/TiO_x/SiO_2/Si$ substrates (Figure. 5.1) appear to show preferential orientation. As the thickness is increased the structure of the film is able to relax away from any strain imparted by the substrate and / or hetroepitaxial growth to the underlying substrate. This allows the film to develop a more 'bulk-like' structure with the (101) and (111) peaks beginning to appear with increasing thickness. However the films remain preferentially orientated throughout the thickness range. This indicates that the $0.6BiFeO_3$ – $0.4PbTiO_3$ film crystallography is closely matched to the substrate and the preferential orientation remains present at increased thicknesses due to the highly orientated underlying $0.6BiFeO_3$ – $0.4PbTiO_3$.

To determine the preferential orientation direction and mis-fit strain on the deposited unit cells, the known lattice parameters of bulk $0.6BiFeO_3$ – $0.4PbTiO_3$ at 565 °C (the deposition temperature) have been used to calculate the d-spacing's and interatomic spacing's (Figure. 5.3) which can then be compared to the interatomic spacing's in the platinum substrate (Figure. 5.4.). The interatomic spacing's shown in Figure. 5.3 and 5.4 describe closely matching lattice parameters between (101) plane of the platinum and the $0.6BiFeO_3$ – $0.4PbTiO_3$ however the platinum is not cut on the (101) plane and therefore this orientation would not be possible if the film orientation is determined by hetroepitaxial growth. The interatomic spacing of the $0.6BiFeO_3$ – $0.4PbTiO_3$ (100) and (001) plane is also very closely matched to the platinum. In addition the (001) plane is cubic which may also increase the likelihood of hetroepitaxial growth from the cubic structure of the platinum substrate. If the (001) plane of the deposited material was to align with the platinum in this way, it would result in a (001) preferred orientation in the deposited film. Based on the interatomic spacing's at the deposition temperature the development of the (001) or (100) preferential orientation seems likely as no other interatomic spacing's are as closely linked to the platinum substrate as these.

NOTE: P2 has been indexed as the (001) for the $0.6BiFeO_3$ - $0.4PbTiO_3$ films and P3 has been indexed as the (100) for the $0.6BiFeO_3$ - $0.4PbTiO_3$ films. The intensity of P1 decreases with increasing thickness and has been indexed as a secondary phase at the substrate – film interface.

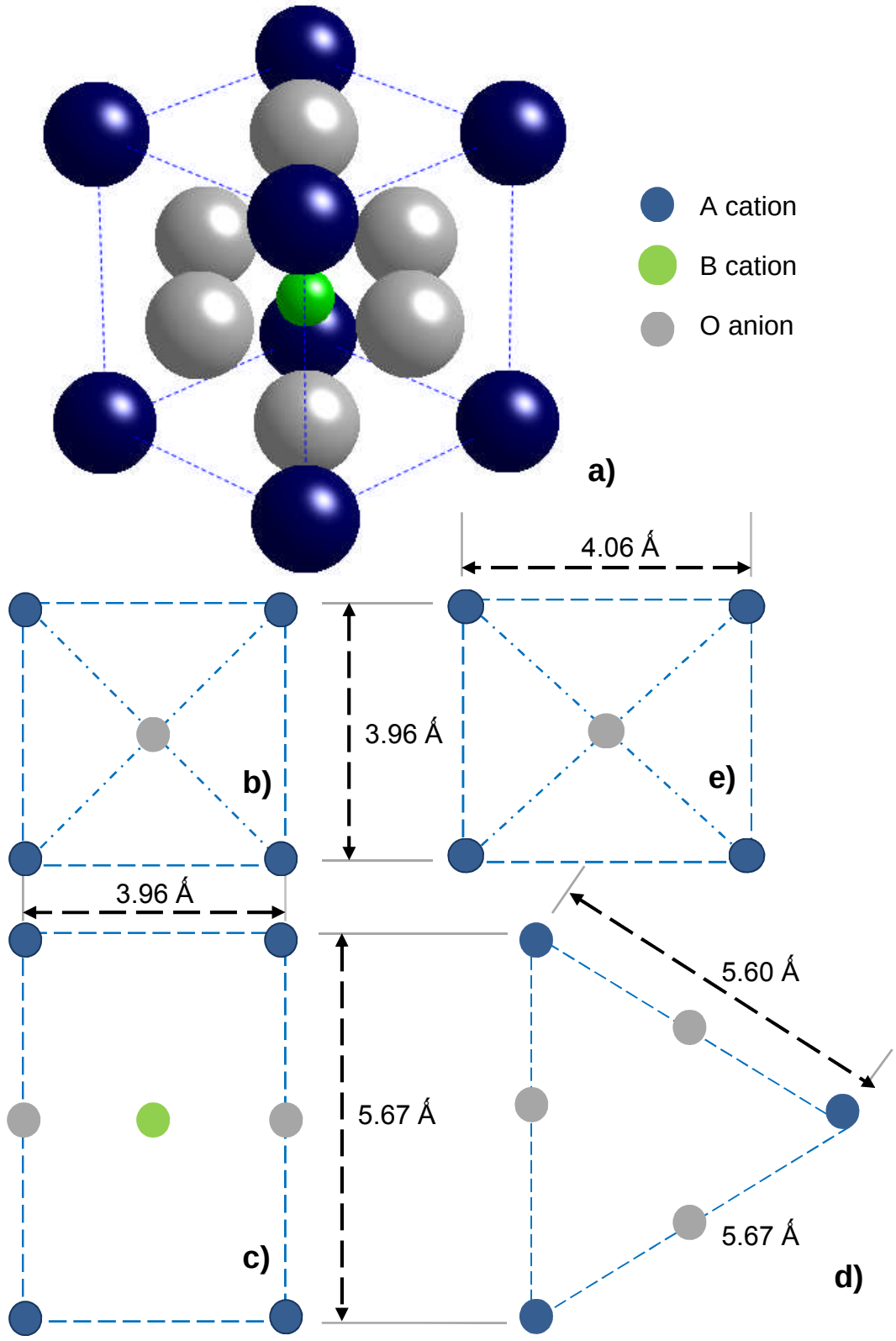

Figure. 5.4. $0.6BiFeO_3$ - $0.4PbTiO_3$ bulk material at 565 °C a) schematic of unit cell, b) dimensions of (001) plane, c) dimensions of the (110) plane, d) dimensions of (111) plane, e) dimensions of (100) plane. (Please see reverse back cover for transparent versions of this diagram).

NOTE: P2 has been indexed as the (001) for the $0.6BiFeO_3$ - $0.4PbTiO_3$ films and P3 has been indexed as the (100) for the $0.6BiFeO_3$ - $0.4PbTiO_3$ films. The intensity of P1 decreases with increasing thickness and has been indexed as a secondary phase at the substrate – film interface.

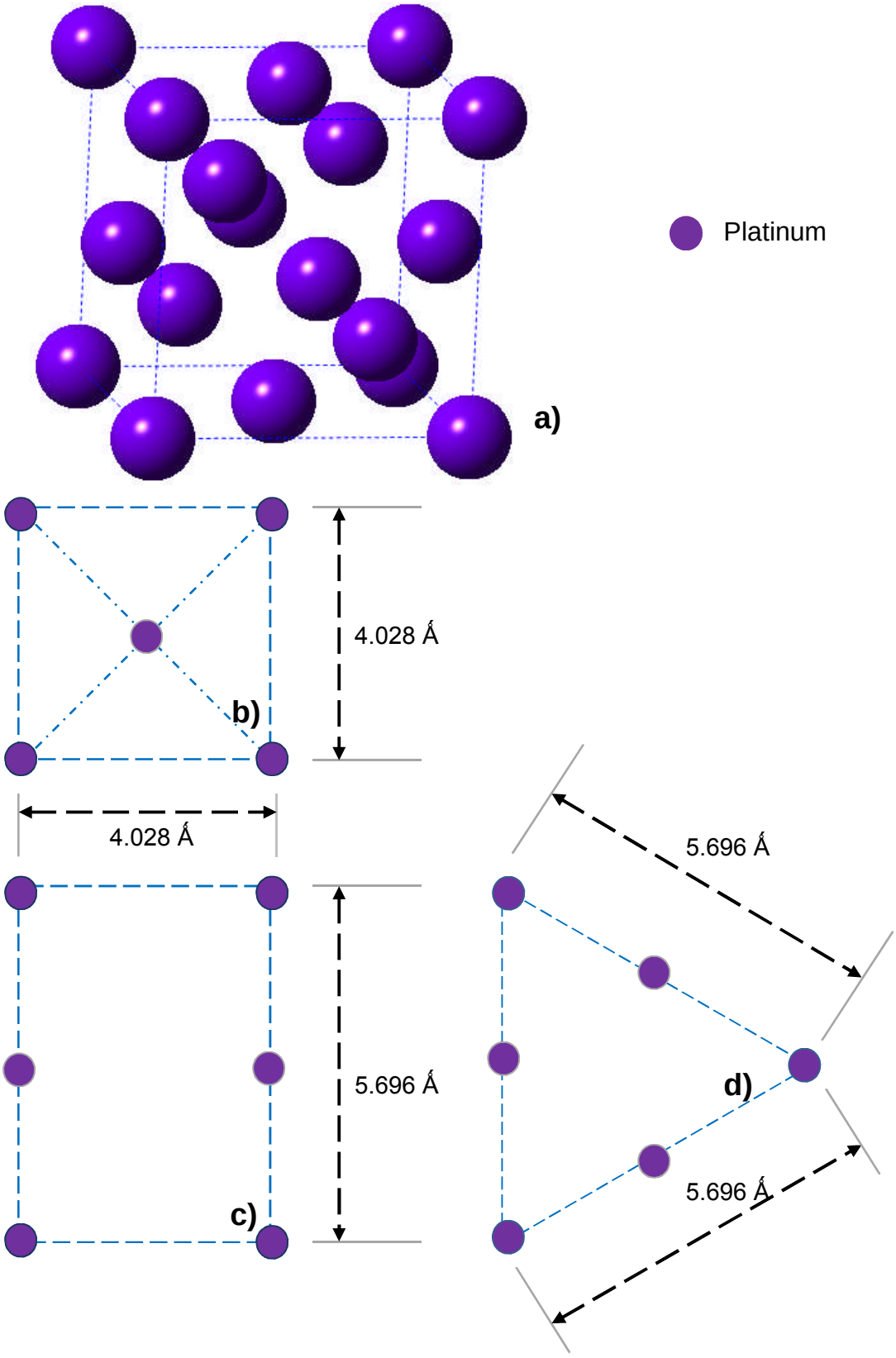

Figure. 5.5. Cubic platinum a) schematic of unit cell, b) dimensions of (100) and (001) plane b) dimensions of (001) plane, c) dimensions of (110) plane, d) dimensions of (111) plane. (See reverse back cover for transparent versions of this diagram).

NOTE: P2 has been indexed as the (001) for the $0.6BiFeO_3$ - $0.4PbTiO_3$ films and P3 has been indexed as the (100) for the $0.6BiFeO_3$ - $0.4PbTiO_3$ films. The intensity of P1 decreases with increasing thickness and has been indexed as a secondary phase at the substrate – film interface.

As the film cools from the deposition temperature (565 °C) to room temperature, the unit cell parameters of bulk $0.6BiFeO_3 – 0.4PbTiO_3$ change, as can be seen in Table. 5.2.

Table. 5.2. Lattice parameters for bulk $0.6BiFeO_3 – 0.4PbTiO_3$ at room temperature and deposition temperature 565 °C.

	$0.6BiFeO_3 – 0.4PbTiO_3$		
Temp (°C)	**a - axis (Å)**	**b - axis (Å)**	**c - axis (Å)**
565	3.96	3.96	4.06
25	3.84	3.84	4.44

This decrease in temperature produces an increase in tetragonality as the T_c phase transition point is approached, with an increase in the c-axis and a decrease in the a-axis, with decreasing temperature. If any of the deposited film was orientated in the [100] directions when held at the deposition temperature, it is likely that the (100) orientated planes will transform to (001) when cooled to room temperature due to the closely matting lattice parameters to the platinum (100) and the cubic interatomic spacing of the $0.6BiFeO_3 – 0.4PbTiO_3$ (001) plane when at room temperature. This would result in a preferential (001) orientated film (as seen in the x-ray traces Figure. 5.1).

In bulk materials the diffraction peaks from the (001) and (100) are assumed to be from the a-axis and c-axis of the unit cell and therefore knowing the (100) d-spacing the (001) d-spacing can be calculated. However, unlike bulk materials, these assumptions cannot be made in thin films because the diffraction peak from the (001) and the (100) may not be from the same unit cell. For example; if the deposited film is orientated in the c-axis only the (001) peak will be seen in the x-ray diffraction trace, however if the film

NOTE: P2 has been indexed as the (001) for the $0.6BiFeO_3$ - $0.4PbTiO_3$ films and P3 has been indexed as the (100) for the $0.6BiFeO_3$ - $0.4PbTiO_3$ films. The intensity of P1 decreases with increasing thickness and has been indexed as a secondary phase at the substrate – film interface.

contains both c-axis and a-axis orientated unit cells the x-ray diffraction trace will show an (001) and (100) peak from different unit cells.

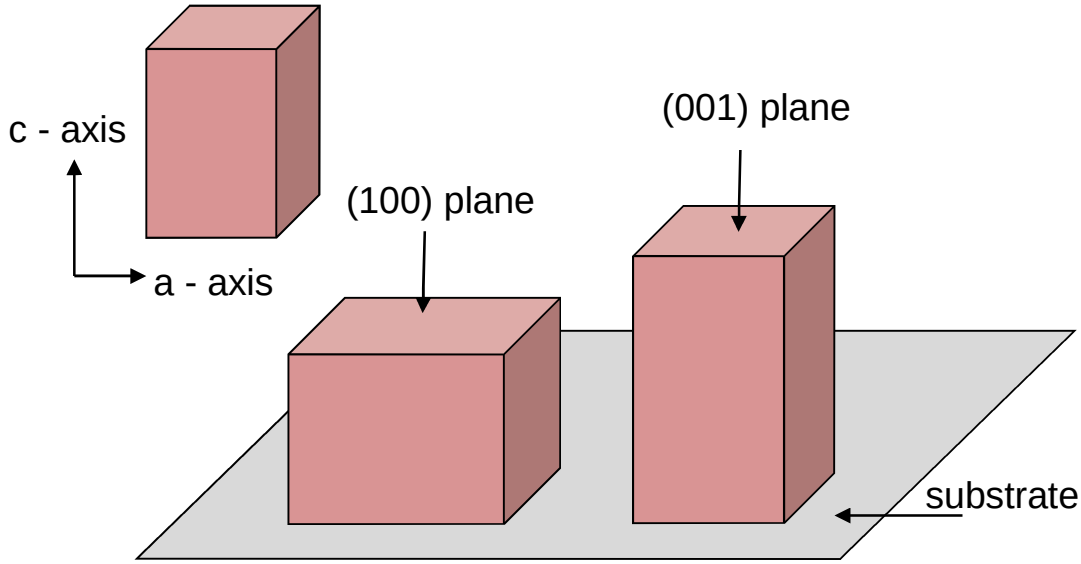

Figure. 5.6. Schematic of (001) and (100) orientation on the substrate.

P2 is the most intense peak seen in the x-ray trace (Figure. 5.1). If this peak is associated with the (001) plane of the deposited material it would mean that the d-spacing of P2 (~4.14 Å) (Table. 5.1) is smaller than the (001) d-spacing in the bulk $0.6BiFeO_3$ - $0.4PbTiO_3$ (4.44 Å). However if the a-axis of the unit cell has increased to match the larger a-axis of the underlying platinum (4.028 Å) the c-axis of the same unit cell will reduce (to retain a similar unit cell volume) thus reducing the d-spacing between the (001) planes. Therefore P2 has been indexed as the (001) for the $0.6BiFeO_3$ - $0.4PbTiO_3$ films.

The d-spacing of P3 is similar to the d-spacing of the (100) in the bulk $0.6BiFeO_3$ - $0.4PbTiO_3$ and when the difference in d-spacing between P2 and P3 is compared to the difference seen in its bulk counterpart, it is likely that P3 is the (100) of the deposited film. In Table. 5.1 the relative peak height of P2 and P3 describe a highly (001) preferred orientation at reduced film thicknesses. With increasing thickness, the relative intensity of the (001)

NOTE: P2 has been indexed as the (001) for the $0.6BiFeO_3$ - $0.4PbTiO_3$ films and P3 has been indexed as the (100) for the $0.6BiFeO_3$ - $0.4PbTiO_3$ films. The intensity of P1 decreases with increasing thickness and has been indexed as a secondary phase at the substrate – film interface.

reduces and an increase in relative intensity of P3 is observed. This increase in intensity with increasing thickness increases the likelihood that P3 relates to the (100) of the film. The increase in concentration of P3 (100) with increasing thickness may be attributed to relaxation with structure with increasing distance from the substrate therefore allowing the structure to take on a more relaxed orientation. However, throughout the thickness range the $0.6BiFeO_3$ - $0.4PbTiO_3$ films remain (001) preferentially orientated.

Although the (001) is a close match to the structure of the underlying substrate the misfit between the platinum and $0.6BiFeO_3$ – $0.4PbTiO_3$ unit cell parameters still remains. The strain that will arise from this appears to have been compensated for by the presence of the closely matching (100) orientation that increases in concentration with increasing thickness.

To calculate the fraction of unit cells which would need to transform into the (100) orientation in order to compensate for the misfit strain present in the (001) orientated films, the thermal expansion coefficient of the underlying silicon needs to be considered as it dramatically differs from that of $0.6BiFeO_3$ – $0.4PbTiO_3$ (which can be seen from the change in $0.6BiFeO_3$ – $0.4PbTiO_3$ lattice parameters in Table. 5.2).

When at the deposition temperature, a length (*L*) of unit cells in the deposited film, with an a-axis (*a*) lattice parameter, the number of unit cells (*n*) is equal to:

$$n = \frac{L}{a} \qquad \textit{Equation. 5.1.}$$

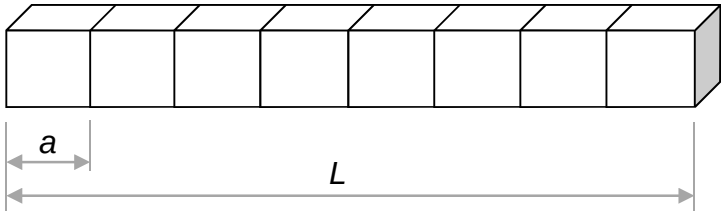

Figure. 5.7. Schematic of the deposited films unit cells of length *L* and in-plane lattice parameter *a* (assuming complete epitaxial strain with the substrate).

NOTE: P2 has been indexed as the (001) for the $0.6BiFeO_3$ - $0.4PbTiO_3$ films and P3 has been indexed as the (100) for the $0.6BiFeO_3$ - $0.4PbTiO_3$ films. The intensity of P1 decreases with increasing thickness and has been indexed as a secondary phase at the substrate – film interface.

As the film is cooled to room temperature the silicon substrate contracts and it is assumed it stresses the deposited film which adjusts the lattice parameters of the unit cells through transformation and stress to take up the new length *L'*.

$$L' = L\,(1 - \alpha\Delta T) \qquad \textit{Equation. 5.2.}$$

where T is the change in temperature and α is the thermal expansions coefficient of silicon (2.6 x 10^{-6} °C^{-1}).

There is still *n* unit cells in *L'* but some of the lattice parameters change to compensate for the stress. It is assumed that *m* of the unit cells have the c-axis in-plane and the rest of the unit cells (*n-m*) have the a-axis in the plane.

$$L' = (n - m)\,a' + mc' \qquad \textit{Equation. 5.3.}$$

$$L' = na' - ma' + mc'$$

$$L' = na' - m\,(c' - a') \qquad .$$

$$m = \frac{L' - na'}{c' - a'}$$

$$m = \frac{L\,(1-\alpha\Delta T) - na'}{c' - a'}$$

$$m = \frac{na\,(1-\alpha\Delta T) - na'}{c' - a'}$$

where *a'* and *c'* are the a-axis and c-axis lattice parameters at room temperature.

NOTE: P2 has been indexed as the (001) for the $0.6BiFeO_3$ - $0.4PbTiO_3$ films and P3 has been indexed as the (100) for the $0.6BiFeO_3$ - $0.4PbTiO_3$ films. The intensity of P1 decreases with increasing thickness and has been indexed as a secondary phase at the substrate – film interface.

To calculate the fraction of unit cells which need to be (100) orientated to relieve the stress, $\frac{m}{n}$ needs to be calculated:

$$\frac{m}{n} = \frac{a\,(1-\alpha\Delta T) - a'}{c' - a'} \qquad \textit{Equation. 5.4.}$$

The lattice parameters of the $0.6BiFeO_3 – 0.4PbTiO_3$ film at the deposition temperature and room temperature can then be substituted into the above equation.

The lattice parameters have been calculated for the temperatures of interest by graphically extrapolating existing data points for silicon, $0.6BiFeO_3 – 0.4PbTiO_3$ and $0.7BiFeO_3 – 0.3PbTiO_3$. from existing literature (Dutta, 1962) (Sai Sunder, 1995). These values are shown in Table. 5.3.

NOTE: P2 has been indexed as the (001) for the $0.6BiFeO_3$ - $0.4PbTiO_3$ films and P3 has been indexed as the (100) for the $0.6BiFeO_3$ - $0.4PbTiO_3$ films. The intensity of P1 decreases with increasing thickness and has been indexed as a secondary phase at the substrate – film interface.

Table. 5.3. Lattice parameters for silicon and $xBiFeO_3 – (1-x)PbTiO_3$ where x = 0.6 and 0.7 at room temperature and deposition temperature 565 °C.

Temperature (°C)	Lattice Parameters	Silicon (Å)	$0.6BiFeO_3 – 0.4PbTiO_3$ (Å)	$0.7BiFeO_3 – 0.3PbTiO_3$ (Å)
	a	3.849	3.984	3.915
600	b	3.849	3.984	3.915
	c	3.849	3.932	4.180
	a	3.848	3.960	3.870
565	b	3.848	3.960	3.870
	c	3.848	4.060	4.405
	a	3.840	3.838	3.816
25	b	3.840	3.838	3.816
	c	3.840	4.438	4.528

Therefore:

$$\frac{m}{n} = \frac{3.96\ (1-(2.6\text{x}10^{-6}\ \text{x}\ 40)) - 3.838}{4.438 - 3.838}$$

$$\frac{m}{n} = 0.19$$

Therefore approximately 19% of the unit cells need to transform from (001) orientated to (100) orientated to relieve the stress imparted at the substrate – film interface with the decrease in temperature from the deposition temperature.

NOTE: P2 has been indexed as the (001) for the $0.6BiFeO_3$ - $0.4PbTiO_3$ films and P3 has been indexed as the (100) for the $0.6BiFeO_3$ - $0.4PbTiO_3$ films. The intensity of P1 decreases with increasing thickness and has been indexed as a secondary phase at the substrate – film interface.

From the peak profile fittings, Figure. 5.2, P2 and P3 describe an (001) preferential orientation throughout the thickness range with an increase in (100) orientations with increasing thickness. However P1 intensity decreases with increasing thickness with respect to P3. This indicates that this phase is present close to the substrate-film interface. The d-spacing of P1 is approximately 4.53 Å which is larger than expected for $0.6BiFeO_3$ - $0.4PbTiO_3$. As $0.6BiFeO_3$ - $0.4PbTiO_3$ is a composition close to the reported mixed phase region in the phase diagram the presence of the rhombohedral phase has been considered, however the (100) peak for the rhombohedral phase is expected to be situated between the (001) and (100) tetragonal in the x-ray trace yet P1 has a higher d-spacing than P2 and P3. Therefore the possibility that P1 arises from the rhombohedral phase has been eliminated. With P3 being present at higher concentrations in the thinner films it is possible that the phase associated with P3 is a secondary phase situated at the substrate-film interface. It has been widely reported that under certain conditions bismuth based compounds can potential react with platinum coated substrates to produce intermetallic phases such as Bi_3Pt_2 and Bi_2Pt. From the evidence provided in the x-ray trace's (Figure. 5.1 and 5.2) it is likely that P1 is a peak from a secondary phase relating to reactions at the film-substrate interface. This has been investigated in further detail later in this chapter.

NOTE: P2 has been indexed as the (001) for the $0.6BiFeO_3$ - $0.4PbTiO_3$ films and P3 has been indexed as the (100) for the $0.6BiFeO_3$ - $0.4PbTiO_3$ films. The intensity of P1 decreases with increasing thickness and has been indexed as a secondary phase at the substrate – film interface.

5.2.1.2. XRD: $0.7BiFeO_3 – 0.3PbTiO_3$ pulsed laser deposited films

Figure. 5.7. shows x-ray diffraction patterns of $0.7BiFeO_3$ - $0.3PbTiO_3$ films of different thicknesses on polycrystalline $Pt/TiO_x/SiO_2/Si$ substrates, which is a composition closer to the morphotropic phase boundary where the mixed phase tetragonal – rhombohedral has been reported. Again the d-spacings and peak heights have been measured between 18 – 24° 2θ for the various film thicknesses from peak profile fitting's using WinPlotR (Figure. 5.8) and can be seen in Table. 5.3.

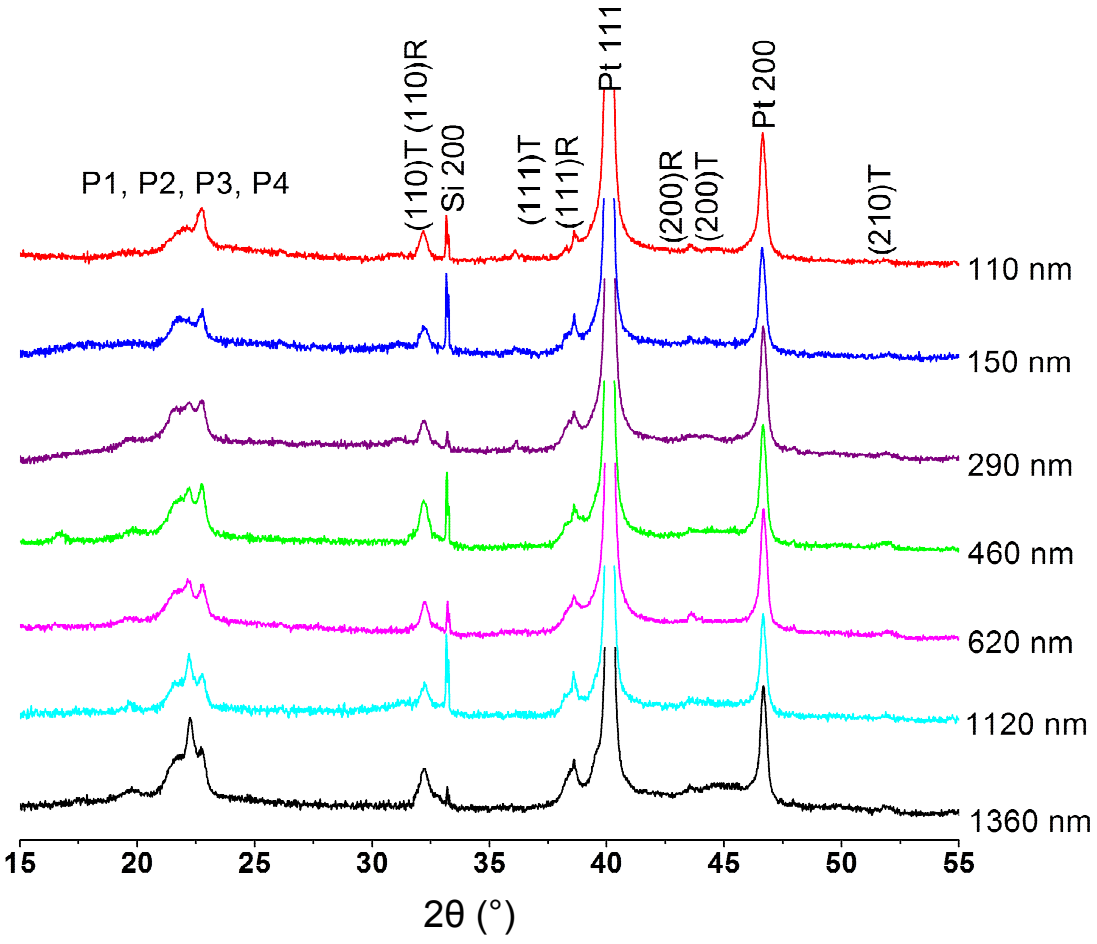

Figure. 5.8. Effect of thickness on XRD traces for $0.7BiFeO_3$ - $0.3PbTiO_3$ films on preferentially orientated $Pt/TiO_x/SiO_2/Si$ substrates

NOTE: For the $0.7BiFeO_3 – 0.3PbTiO_3$ films on preferentially orientated platinum substrates: P1 has been indexed as a secondary phase at the substrate – film interface, P2 the $(001)_{tetragonal}$, P3 the $(100)_{rhombohedral}$ and P4 the $(100)_{tetragonal}$.

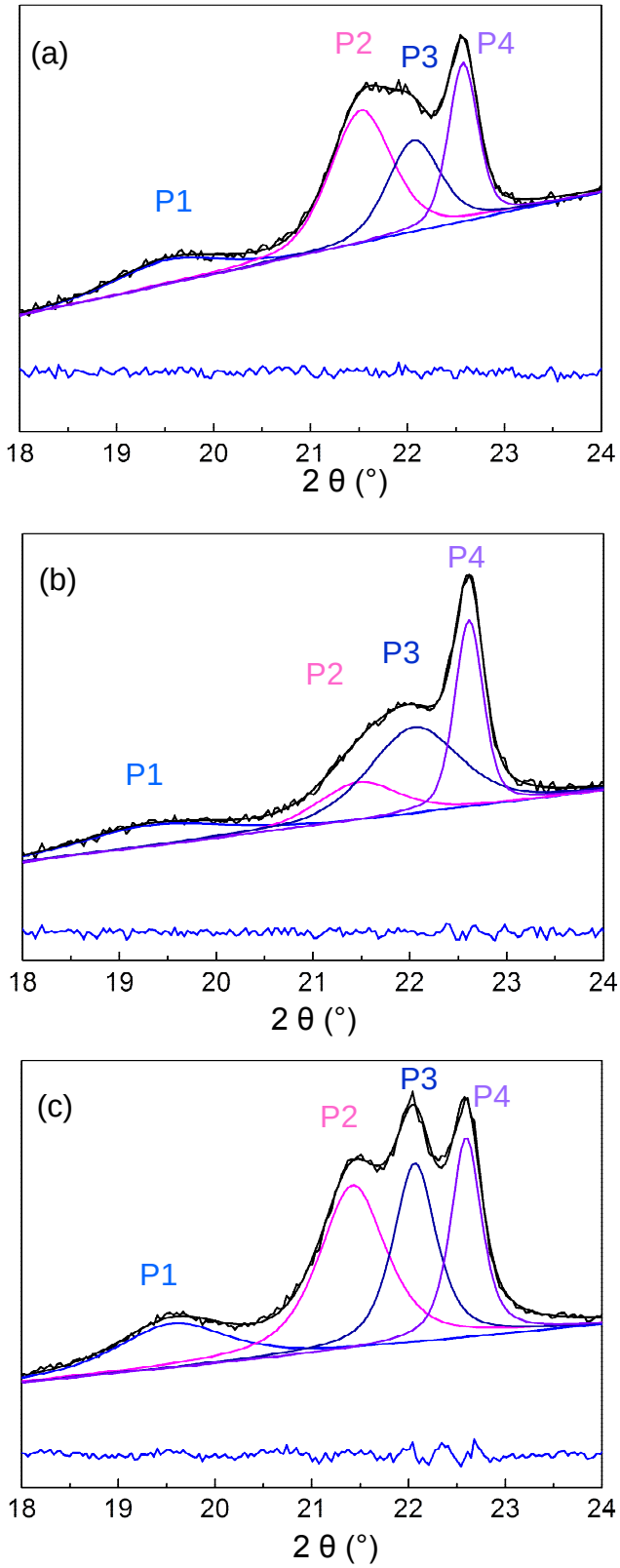

Figure. 5.9. X-ray peak profile fitting between 18 – 24° 2θ for $0.7BiFeO_3$ - $0.3PbTiO_3$ films of thickness a) 110 nm, b) 150 nm, c) 290 nm. P1, P2, P3 and P4 indicate the four peaks identified.

NOTE: For the $0.7BiFeO_3$ – $0.3PbTiO_3$ films on preferentially orientated platinum substrates: P1 has been indexed as a secondary phase at the substrate – film interface, P2 the $(001)_{tetragonal}$, P3 the $(100)_{rhombohedral}$ and P4 the $(100)_{tetragonal}$.

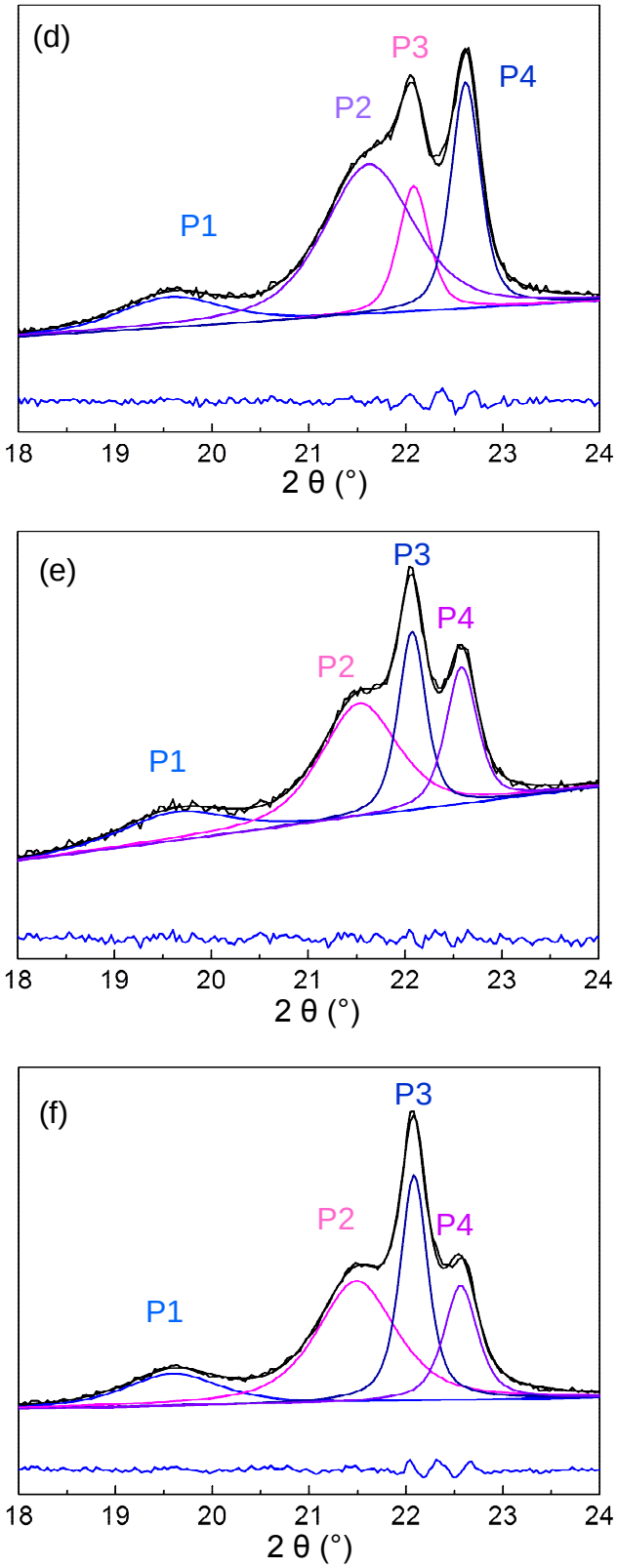

Figure. 5.9. X-ray peak profile fitting between 18 – 24° 2θ for $0.7BiFeO_3$ - $0.3PbTiO_3$ films of thickness d) 460 nm, e) 1120 nm, f) 1360 nm. P1, P2, P3 and P4 indicate the four peaks identified.

NOTE: For the $0.7BiFeO_3$ – $0.3PbTiO_3$ films on preferentially orientated platinum substrates: P1 has been indexed as a secondary phase at the substrate – film interface, P2 the $(001)_{tetragonal}$, P3 the $(100)_{rhombohedral}$ and P4 the $(100)_{tetragonal}$.

Table. 5.4. The measured d-spacing's of the four peaks identified in the peak profile fittings for $0.7BiFeO_3 – 0.3PbTiO_3$ films using WinPlotR with the corresponding peak heights.

Film Thickness (nm)	**d-spacing P1 (Å)**	**d-spacing P2 (Å)**	**d-spacing P3 (Å)**	**d-spacing P4 (Å)**	**Height P1**	**Height P2**	**Height P3**	**Height P4**
110	4.55	4.13	4.03	3.94	0.05	0.32	0.27	0.36
150	4.59	4.14	4.03	3.93	0.05	0.21	0.23	0.50
290	4.53	4.14	4.02	3.93	0.07	0.26	0.34	0.33
460	4.53	4.11	4.02	3.93	0.06	0.22	0.43	0.28
620	4.51	4.10	4.00	3.90	0.06	0.27	0.36	0.31
1120	4.51	4.12	4.02	3.93	0.05	0.23	0.34	0.38
1360	4.53	4.13	4.02	3.94	0.06	0.22	0.48	0.24

NOTE: For the $0.7BiFeO_3 – 0.3PbTiO_3$ films on preferentially orientated platinum substrates: P1 has been indexed as a secondary phase at the substrate – film interface, P2 the $(001)_{tetragonal}$, P3 the $(100)_{rhombohedral}$ and P4 the $(100)_{tetragonal}$.

The peak profile analysis between 18 - 24° 2θ describes the presence of an extra peak to the three seen in the $0.6BiFeO_3$ - $0.4PbTiO_3$ films. The four peaks identified will be referred to as P1, P2, P3 and P4 (Figure. 5.7 and 5.8).

The most intense peak for $BiFeO_3$ – $PbTiO_3$ powder diffraction is the (101) however Figure. 5.7. shows the (100) and (111) peaks being more intense than the (101). This indicates that the films are influenced by the (111) and (200) of the underlying platinum rather than adapting the bulk relaxed form. Although this is not one direction preferred orientation, as seen in the $0.6BiFeO_3$ – $0.4PbTiO_3$ films, it is still referred to as preferred orientation because the film adapts a substrate influenced structure rather than a relaxed form that would been seen in a powder of the same composition. This indicates that although the films are influenced by the substrate structure, the change in composition produces a film that less readily grows hetroepitaxialy to one particular plane in the atomic structure of the underlying platinum substrate.

Analysis of the peak profile fit's shows P1 has the same d-spacing's as the peak associated with the secondary phase in the $0.6BiFeO_3$ – $0.4PbTiO_3$ films therefore it is likely that P1 is associated with a secondary phase from possible substrate film interactions.

The d-spacing's of P2 and P4 are very similar to those indexed as the (001) and (100) in the $0.6BiFeO_3$ – $0.4PbTiO_3$ films, with the 110nm films producing a difference of 0.007 Å for P2 and 0.09 Å for P4 in the d-spacing values. Therefore P2 has been indexed the $(001)_{tetragonal}$ and P4 the $(100)_{tetragonal}$. P3 has a d-spacing of 4.02 Å and is situated between the (001) and (100) tetragonal in the x-ray trace. As $0.7BiFeO_3$ - $0.3PbTiO_3$ is a composition close to the reported mixed phase region in the phase diagram the presence of the rhombohedral phase has once again been considered. Due to this it seems likely that P3 is associated with the (100) rhombohedral phase. Further evidence of this is obtained from analysis of the peak heights (Table. 5.4) with P3 increasing in intensity with increasing thickness to become the most dominant peak.

NOTE: For the $0.7BiFeO_3$ – $0.3PbTiO_3$ films on preferentially orientated platinum substrates: P1 has been indexed as a secondary phase at the substrate – film interface, P2 the $(001)_{tetragonal}$, P3 the $(100)_{rhombohedral}$ and P4 the $(100)_{tetragonal}$.

The a–axis of the platinum is larger than the expected rhombohedral and tetragonal, as shown in Table. 5.5. however it is closer to the rhombohedral parameters. If the film orientation was dependent on the substrate alone a rhombohedral film orientation would be expected. The 110nm film appears to be predominantly tetragonal with a small amount of rhombohedral phase present; however as the film thickness is increased the rhombohedral phase becomes the dominant phase. This indicates that the strain required for the $0.7BiFeO_3$ - $0.3PbTiO_3$ tetragonal phase to grow hetroepitaxialy to the substrate (which is higher than was seen in the $0.6BiFeO_3$ - $0.4PbTiO_3$ films) is too much for the tetragonal phase to remain stable and therefore transforms to the less strained state of rhombohedral.

Table. 5.5. The a-axis unit cell parameters of platinum and rhombohedral and tetragonal $0.7BiFeO_3$ - $0.3PbTiO_3$ in powder form.

Phase	**a-axis (Å)**	**Difference in a-axis to platinum (Å)**
$0.7BiFeO_3$ - $0.3PbTiO_3$ tetragonal	3.816	0.212
$0.7BiFeO_3$ - $0.3PbTiO_3$ rhombohedral	3.969	0.059
Platinum substrate	4.028	

Although the $0.6BiFeO_3$ – $0.4PbTiO_3$ films displayed evidence of an increase in the (100) orientation with increasing thickness, the preferred orientation and overall structure changed very little. The $0.7BiFeO_3$ – $0.3PbTiO_3$ films displayed dramatic changes with increasing thickness from a tetragonal structure with a tetragonal (100) preferential orientation to a mixed phase structure with the rhombohedral being the dominant phase and highly orientated (100) direction. As the d-spacing between the $0.6BiFeO_3$ – $0.4PbTiO_3$ and $0.7BiFeO_3$ – $0.3PbTiO_3$ films varied very little it appears that

NOTE: For the $0.7BiFeO_3$ – $0.3PbTiO_3$ films on preferentially orientated platinum substrates: P1 has been indexed as a secondary phase at the substrate – film interface, P2 the $(001)_{tetragonal}$, P3 the $(100)_{rhombohedral}$ and P4 the $(100)_{tetragonal}$.

the inherent preference of the $0.7BiFeO_3$ – $0.3PbTiO_3$ composition to be mixed phase tetragonal – rhombohedral prevents the films from hetroepitaxialy growing on the substrate to the same extent as the $0.6BiFeO_3$ – $0.4PbTiO_3$ films. However the dominance of the preferred (100) rhombohedral orientation at the increased thickness is clear evidence of substrate influence on the films structure.

5.2.2. XRD: $0.7BiFeO_3$ – $0.3PbTiO_3$ Films on (111) Orientated Pt Substrates

This section discusses the characterisation from x-ray diffraction analysis of $0.7BiFeO_3$ – $0.3PbTiO_3$ thin films on (111) orientated $Pt/TiO_2/SiO_2/Si$ substrates.

Figure. 5.9. shows x-ray diffraction traces for $0.7BiFeO_3$ - $0.3PbTiO_3$ films on (111) orientated $Pt/TiO_x/SiO_2/Si$ substrates at different film thicknesses. If the platinum substrate is cut on one crystallographic plane, (111), it should forbid hetroepitaxial growth on the (100) and (110) due to the large differences in interatomic spacing's between the different planes. If the film is to grow hetroepitaxialy on the (111), the unit cells within the deposited film must be able to withstand over 16% strain to hetroepitaxial grow on the (111) of the platinum substrate.

The x-ray diffraction trace's in Figure. 5.9. show a preferred (111) orientation in the thinner films, however the unit cell parameters ('a' axis = 3.92 Å, 'c' axis = 4.58 Å) appear to be very closely match to the relaxed bulk $0.7BiFeO_3$ – $0.3PbTiO_3$. This indicates that the films are unable to withstand the high strain required to grow hetroepitaxialy on the (111) platinum and take on a more relaxed tetragonal phase even at the lower thicknesses. As the thickness is increased the films exhibit an enhanced (100) and (110) texture. This suggests that the development of the (111) orientation in thinner films is nucleation controlled whilst the formation of the (100) and (110) orientation in thicker films is growth controlled. Unlike the $0.7BiFeO_3$ - $0.3PbTiO_3$ films on polycrystalline platinum, there is no evidence of a rhombohedral phase being

present. As the films arrange in a relaxed polycrystalline state, there is no need for the rhombohedral phase to be present to accommodate the strain.

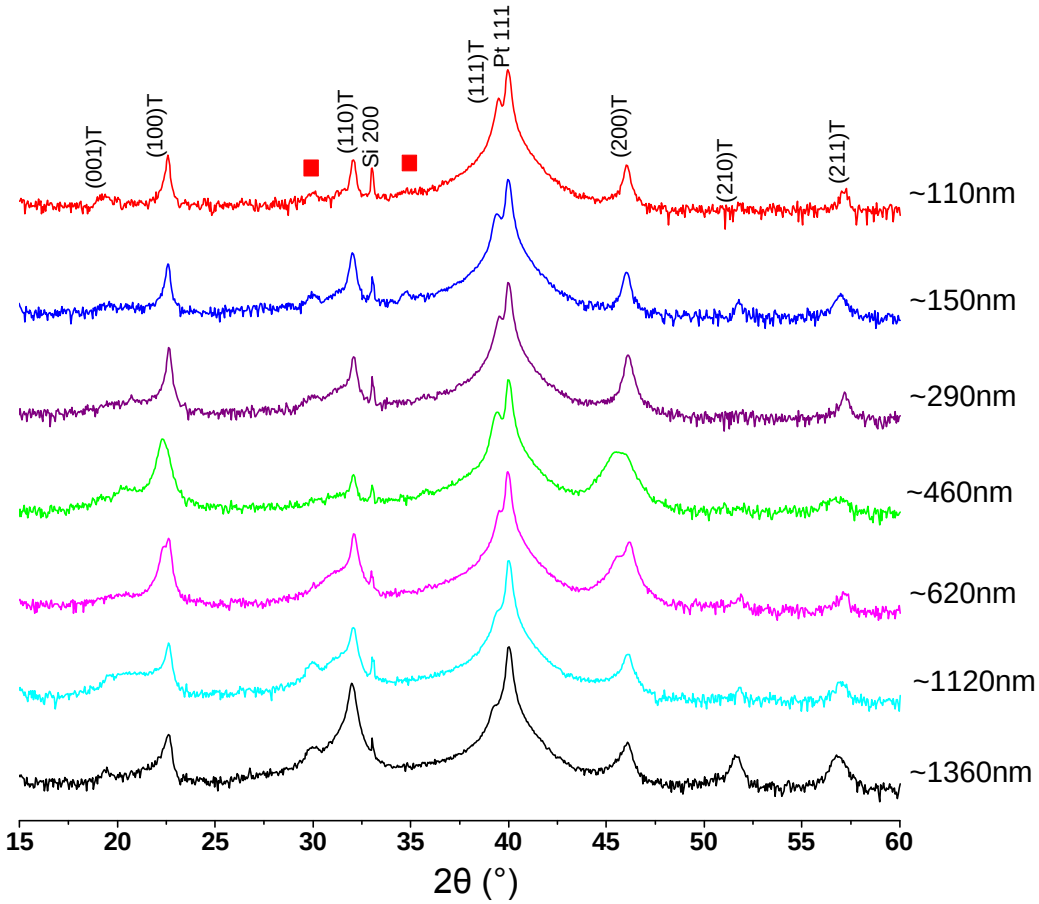

Figure. 5.10. Effect of thickness on XRD traces for $0.7BiFeO_3$ - $0.3PbTiO_3$ on (111) orientated $Pt/TiO_x/SiO_2/Si$ substrates. ■ = secondary phase

5.2.3. Microstructure of Films – AFM and SEM

This section discusses the characterisation from atomic force microscopy and scanning electron microscopy analysis of $xBiFeO_3$ – $(1-x)PbTiO_3$ thin films on preferentially orientated $Pt/TiO_2/SiO_2/Si$ substrates. Two different film compositions are discussed within this section starting with $0.7BiFeO_3$ – $0.3PbTiO_3$ films (section 5.2.3.1.) followed by $0.6BiFeO_3$ – $0.4PbTiO_3$ films (section 5.2.3.2.)

5.2.3.1. Growth: $0.7BiFeO_3 – 0.3PbTiO_3$ pulsed laser deposited films

As can be seen in Table. 5.6 and the corresponding graph Figure. 5.10, above 290 nm, 40,000 pulsed laser shots, there is a linear increase in thickness with respect to the number of pulses emitted from the laser. However, below 290 nm there is a non-linear relationship between film thickness and pulses emitted.

Table. 5.6. A table to show the film thickness of $0.7BiFeO_3 – 0.3PbTiO_3$ films on preferentially orientated Pt substrates after a set number of laser pulses.

Number of pulsed laser shots	Thickness	RMS Roughness
5,000	110 nm	21.6 nm
10,000	150 nm	17.3 nm
20,000	210 nm	14.1 nm
40,000	290 nm	14.4 nm
50,000	460 nm	14.4 nm
60,000	620 nm	13.9 nm
80,000	1120 nm	14.4 nm
90,000	1360 nm	18.4 nm

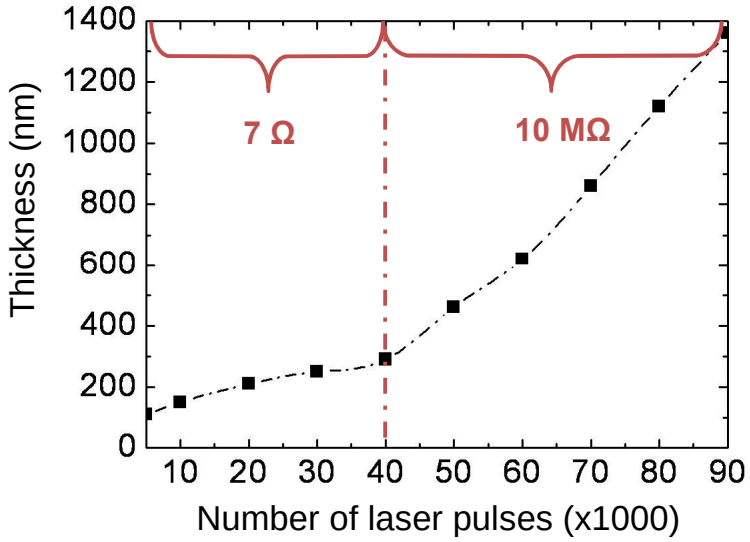

Figure. 5.11. A graph to show thickness as a function of the number of laser pulses for $0.7BiFeO_3$ - $0.3PbTiO_3$ on preferentially orientated $Pt/TiO_x/SiO_2/Si$ substrates (this is discussed in further detail in section 5.2.3.3).

To investigate this in further detail the surface profile of $xBiFeO_3 – (1-x)PbTiO_3$ films on preferentially orientated Pt substrates, films were analysed by atomic force microscopy (AFM) for various film thicknesses, Figure. 5.11.

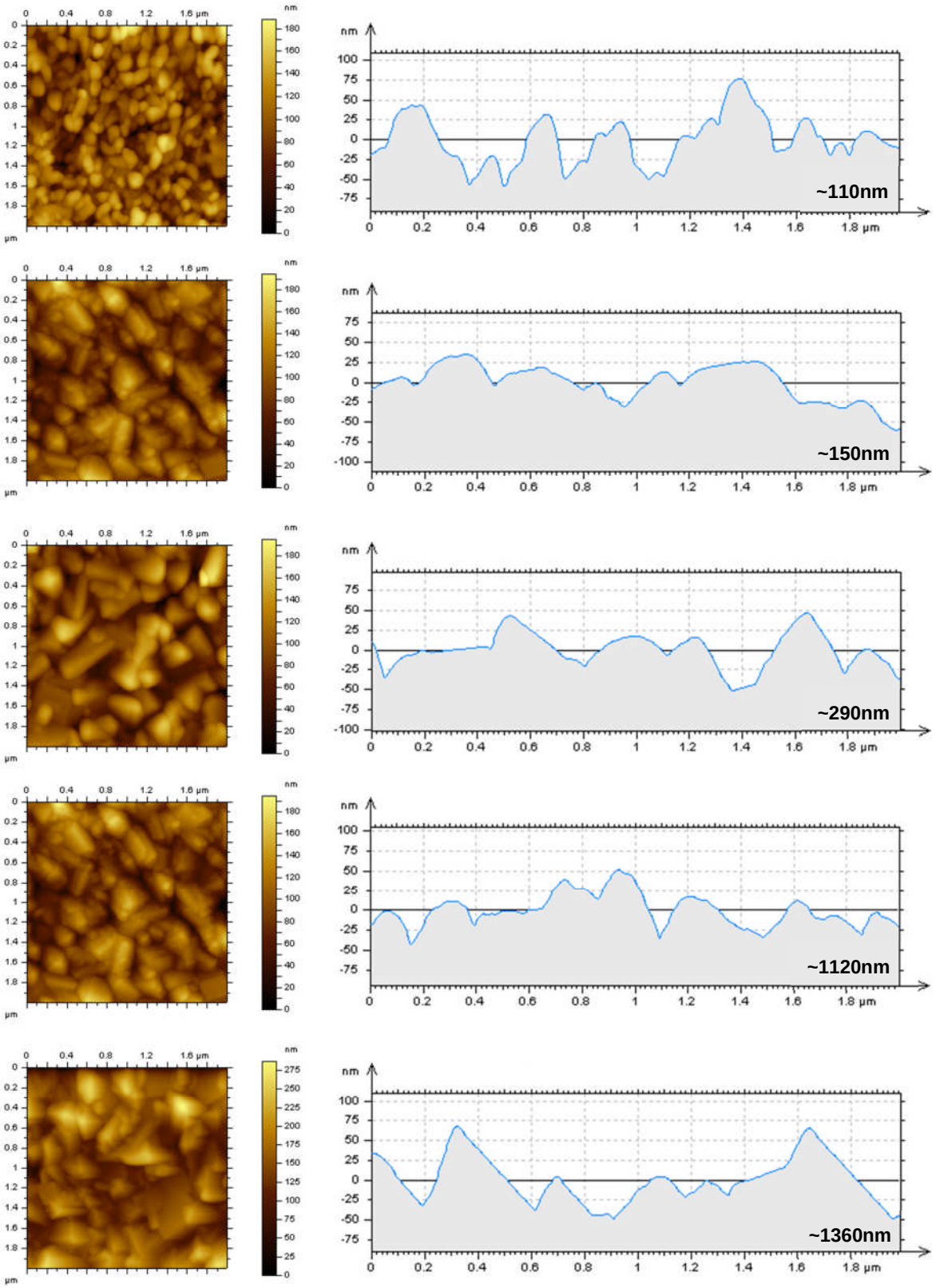

Figure. 5.12. A 2D AFM 2 x 2 μm image of the surface of $0.7BiFeO_3$ - $0.3PbTiO_3$ films, of different thicknesses, on preferentially orientated $Pt/TiO_x/SiO_2/Si$ substrates and a profile plot of the morphology.

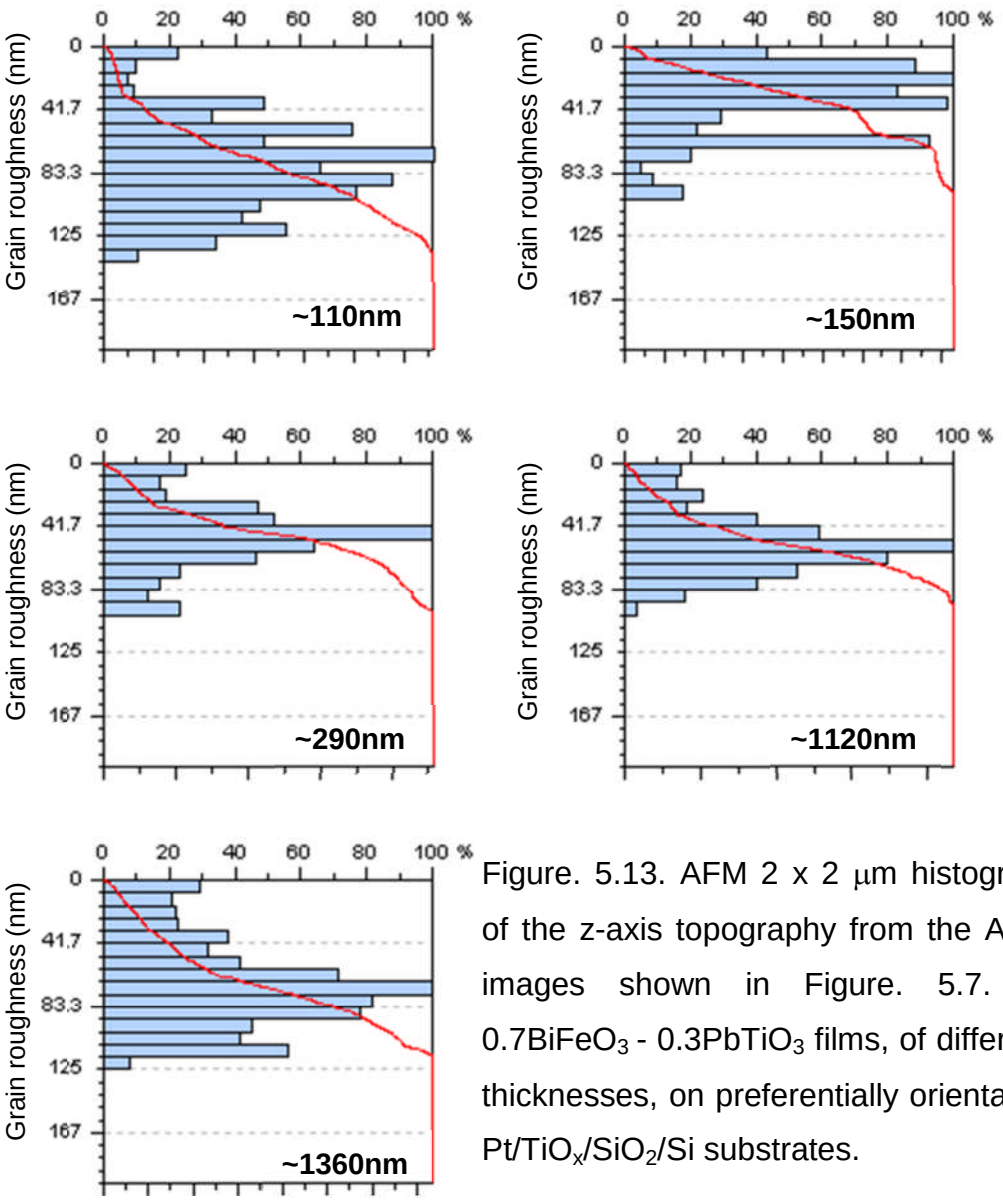

Figure. 5.13. AFM 2 x 2 μm histogram of the z-axis topography from the AFM images shown in Figure. 5.7. of $0.7BiFeO_3$ - $0.3PbTiO_3$ films, of different thicknesses, on preferentially orientated $Pt/TiO_x/SiO_2/Si$ substrates.

When comparing the surface profile and morphology in Figure. 5.11 of the 110 nm film to the 290 nm film, the peak-to-trough distance decreases with increasing thickness. It can also be seen from the surface profiles in Figure. 5.11 of the 110 nm and 290 nm that the grain size increases with increasing thickness. This suggests that any material deposited after the film has exceeded 110 nm, nucleates in the holes between the grains already deposited, resulting in the reduced peak-to-trough distance. The already existing grains then grow at the expense of the smaller grains resulting in an increased grain size. This theory is supported by the histograms presented in Figure. 5.12 whereby the average peak-to-trough distance is reduced from

~70 nm for 110 nm films to ~ 30 nm for 150 nm films, producing a more uniform thickness. Figure. 5.12 confirms a mono-modal grain height distribution at 110 nm and a bi-modal grain height distribution at 150 nm. As the thickness is increased to 290 nm the average peak-to trough distance remains relatively low at ~ 50 nm with a mono-modal height distribution. This suggests that the Volmer-Weber growth mechanism is occurring at the lower thicknesses, whereby the coercive energy of the atoms within the film is greater than that between the atoms of the film and substrate resulting in island formation. The Volmer-Weber island mechanism will continue to occur as the thickness of the film is increased due to the topography that is already present. This is evident as the films approach a thickness of ~1120 nm where the average peak-to-trough distance is larger than that of the 290 nm film and still mono-modal. However as the thickness is increased to ~1360 nm the average peak-to-trough distance dramatically increases and develops a bi-modal distribution, suggesting a columnar growth of grains in the z-direction. AFM (Figure. 5.11) and SEM images (Figure. 5.13) imply that the $0.7BiFeO_3$ - $0.3PbTiO_3$ films on preferentially orientated $Pt/TiO_x/SiO_2/Si$ grow into a columnar structure. Therefore the films grow in the (111) c-axis direction.

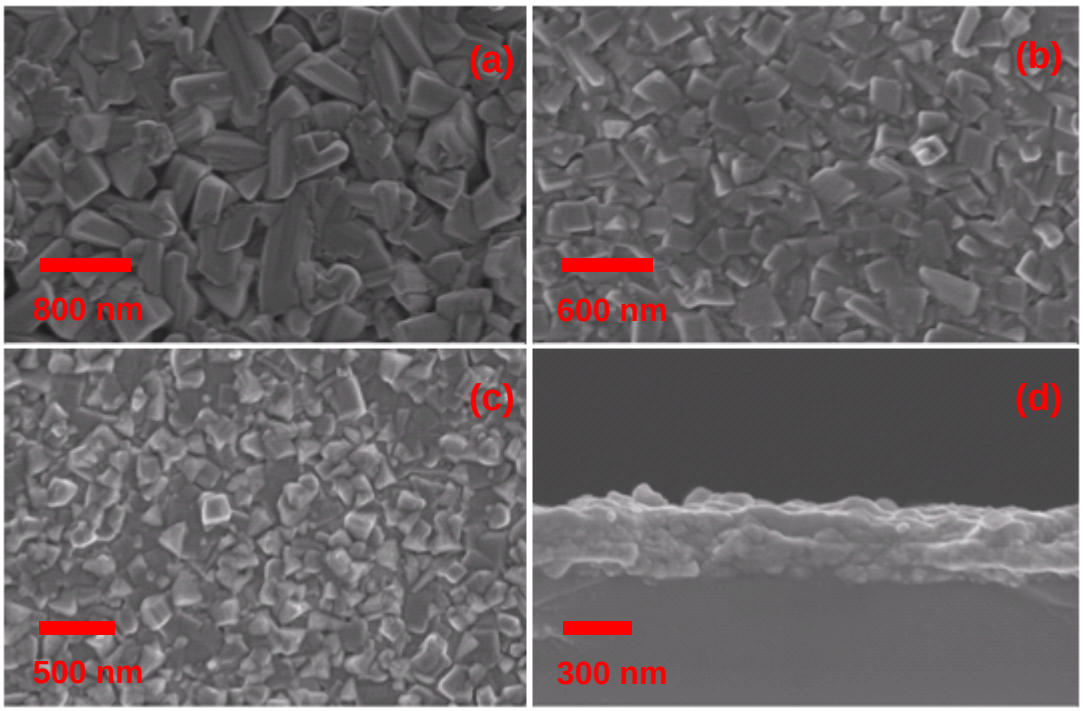

Figure. 5.14. SEM images of $xBiFeO_3 – (1-x)PbTiO_3$ films approximately 290 nm thickness (a) x = 0.7 film on (111) $Pt/TiO_x/SiO_2/Si$, (b) x = 0.6 on polycrystalline $Pt/TiO_x/SiO_2/Si$, (c) x = 0.7 on preferentially orientated $Pt/TiO_x/SiO_2/Si$, (d) cross section of x = 0.7 on preferentially orientated $Pt/TiO_x/SiO_2/Si$.

5.2.3.2. Growth: $0.6BiFeO_3 – 0.4PbTiO_3$ pulsed laser deposited films

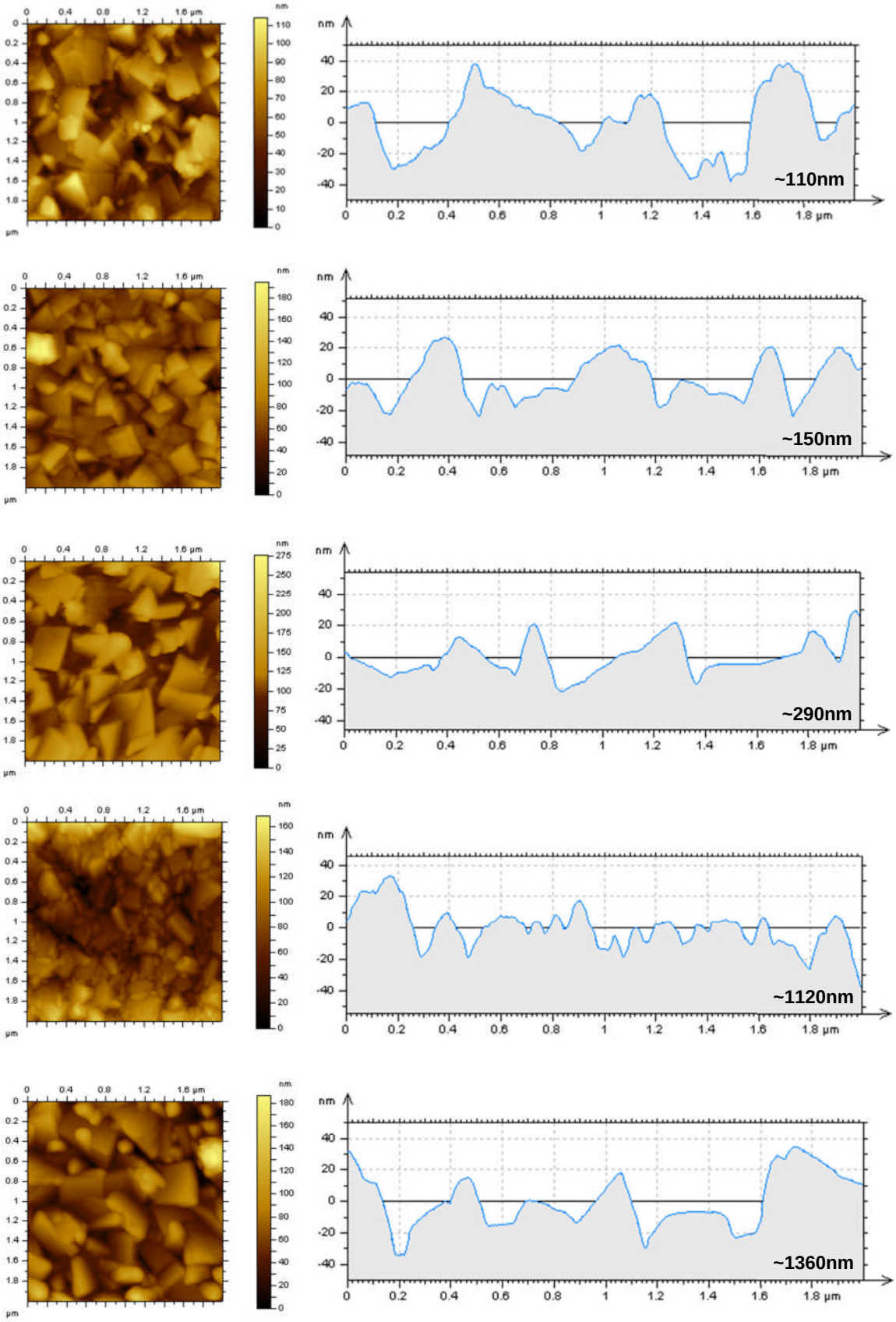

Figure. 5.15. A 2D AFM 2x2 μm image of the surface of $0.6BiFeO_3$ - $0.4PbTiO_3$ films, of different thicknesses, on polycrystalline $Pt/TiO_x/SiO_2/Si$ substrates and a profile plot of the morphology.

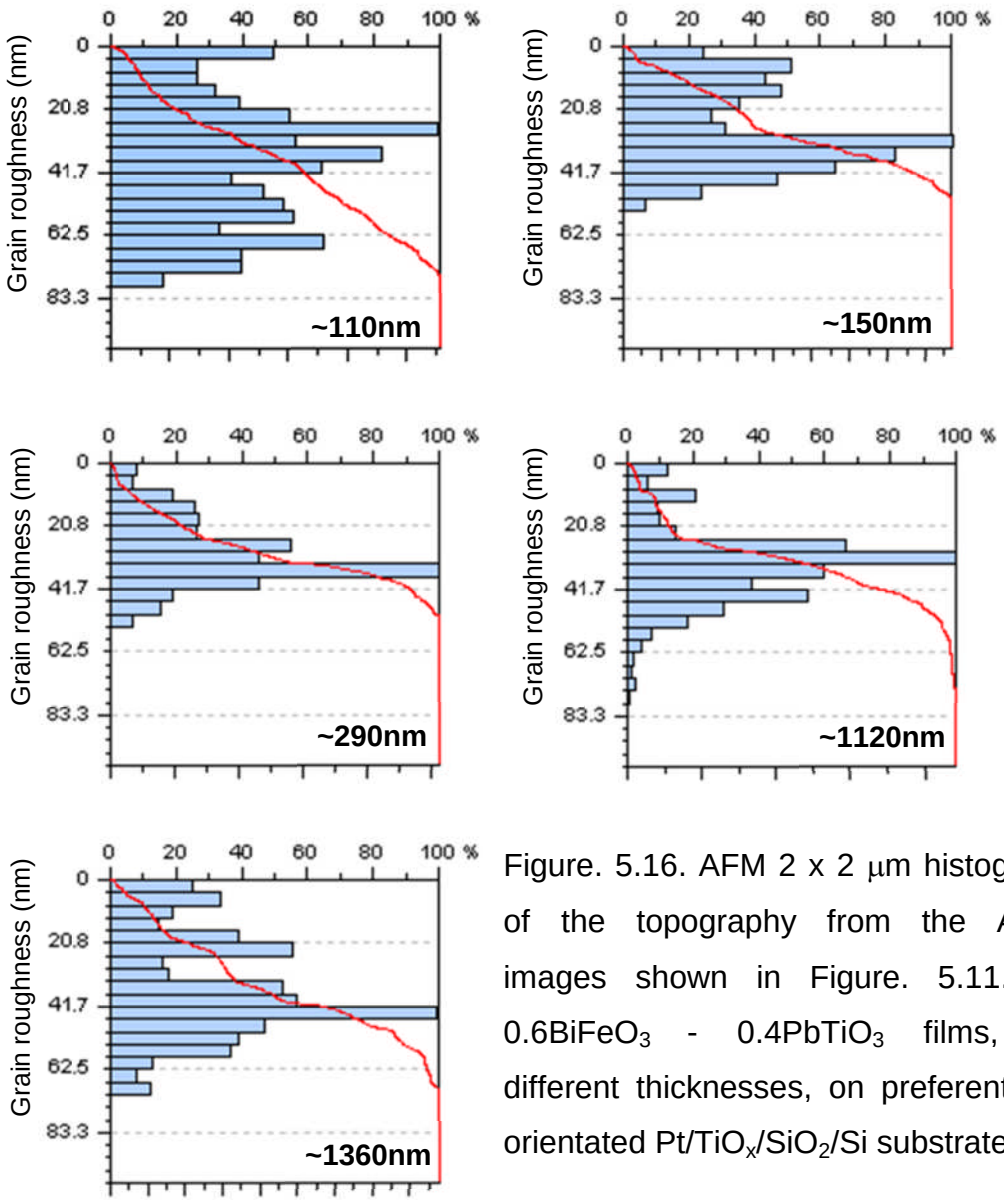

Figure. 5.16. AFM 2 x 2 μm histogram of the topography from the AFM images shown in Figure. 5.11. of $0.6BiFeO_3$ - $0.4PbTiO_3$ films, of different thicknesses, on preferentially orientated $Pt/TiO_x/SiO_2/Si$ substrates.

When comparing the surface profile and morphology for the $0.6BiFeO_3$ - $0.4PbTiO_3$ films (Figure. 5.14) of the 110 nm film to the 290 nm film the peak-to-trough distance decreases with increasing thickness even more than that seen in the $0.7BiFeO_3$ - $0.3PbTiO_3$ films (Figure. 5.11). Unlike the $0.7BiFeO_3$ - $0.3PbTiO_3$ films, it is only when the 290 nm film thickness is obtained that the average peak-to-trough distance is reduced and a mono-modal distribution is observed. At ~ 290 nm the average peak-to-trough distance also increases, suggesting that any material present before ~ 290 nm nucleates in the holes between the grains already deposited and grows at the expense of the smaller grains resulting in an increased grain size. The

histogram in Figure. 5.15 suggest that the Volmer-Weber growth mechanism is occurring in the $0.6BiFeO_3$ - $0.4PbTiO_3$ films. Just as was seen in the $0.7BiFeO_3$ - $0.3PbTiO_3$ films, the Volmer-Weber island mechanism continues to occur as the thickness of the film is increased up to the 1120 - 1360 nm range. The ~ 1120 nm film has a larger average peak-to-trough distance than that of the 290 nm film with a mono-modal height distribution, whilst the ~1360 nm film's average peak-to-trough distance dramatically increases and develops a bi-modal distribution, suggesting that material is once again nucleating within the troughs of the films surface. AFM (Figure. 5.14) and SEM images (Figure. 5.13) show that the $0.6BiFeO_3$ - $0.4PbTiO_3$ films on preferentially orientated $Pt/TiO_x/SiO_2/Si$ grow into a plate-like structure suggesting the (100) plane sits parallel to the (100) plane of the platinum substrate.

5.2.3.3. Defects in Structure of Films and Resulting Conductivity

At ~290 nm both the $0.7BiFeO_3$ - $0.3PbTiO_3$ and $0.6BiFeO_3$ - $0.4PbTiO_3$ films go from being conductive (7 Ω) to resistive (~ 10 MΩ). Based on the AFM and SEM analysis it is probable that physical defects may be present within the films below ~ 290 nm that result in short circuits. Once the thickness is increased above ~ 290 nm the films become resistive suggesting that any holes within the films structure are no longer present as the Volmer-Weber growth mode fills the holes therefore the platinum bottom electrode is no longer exposed.

From these results it appears the conductivity at reduced thicknesses is a direct result of physical defects within the films. By increasing the thickness beyond 290 nm the films are no longer conductive due to the absence of physical defects within the structure of the film. However none of the films tested were able to produce ferroelectric polarization-electric field loops (P-E loops) despite their increased thickness.

5.2.4. Piezoelectric Response

When the $0.7BiFeO_3$ - $0.3PbTiO_3$ and $0.6BiFeO_3$ - $0.4PbTiO_3$ films of differing thicknesses on polycrystalline $Pt/TiO_x/SiO_2/Si$ were tested on the PFM, the films did not display a convincing piezoelectric response below 290 nm and all films above 290 nm displayed a piezoelectric response in both normal and the lateral direction Figure. 5.16. The thickness at which a piezoelectric response is observed (290 nm) is referred to as the critical thickness for the remainder of this chapter.

Figure. 5.16 shows areas with a clear piezoelectric response. Domain patterns are observed with little correlation with topography and were verified by scanning different areas of the sample. The PFM response indicates an out-of-plane preferential orientation as the piezoelectric response from different facets delivers different levels of response, whilst the response from individual grains on the top surface all describe a 180° phase difference. This implies that all of grains/domains orientated out-of-plane are grains orientated in the same direction with a large piezoelectric response. From x-ray diffraction and atomic force microscopy analysis (Figure. 5.7. and 5.11.) the grain orientation with a large piezoelectric response appears to be the (111) direction.

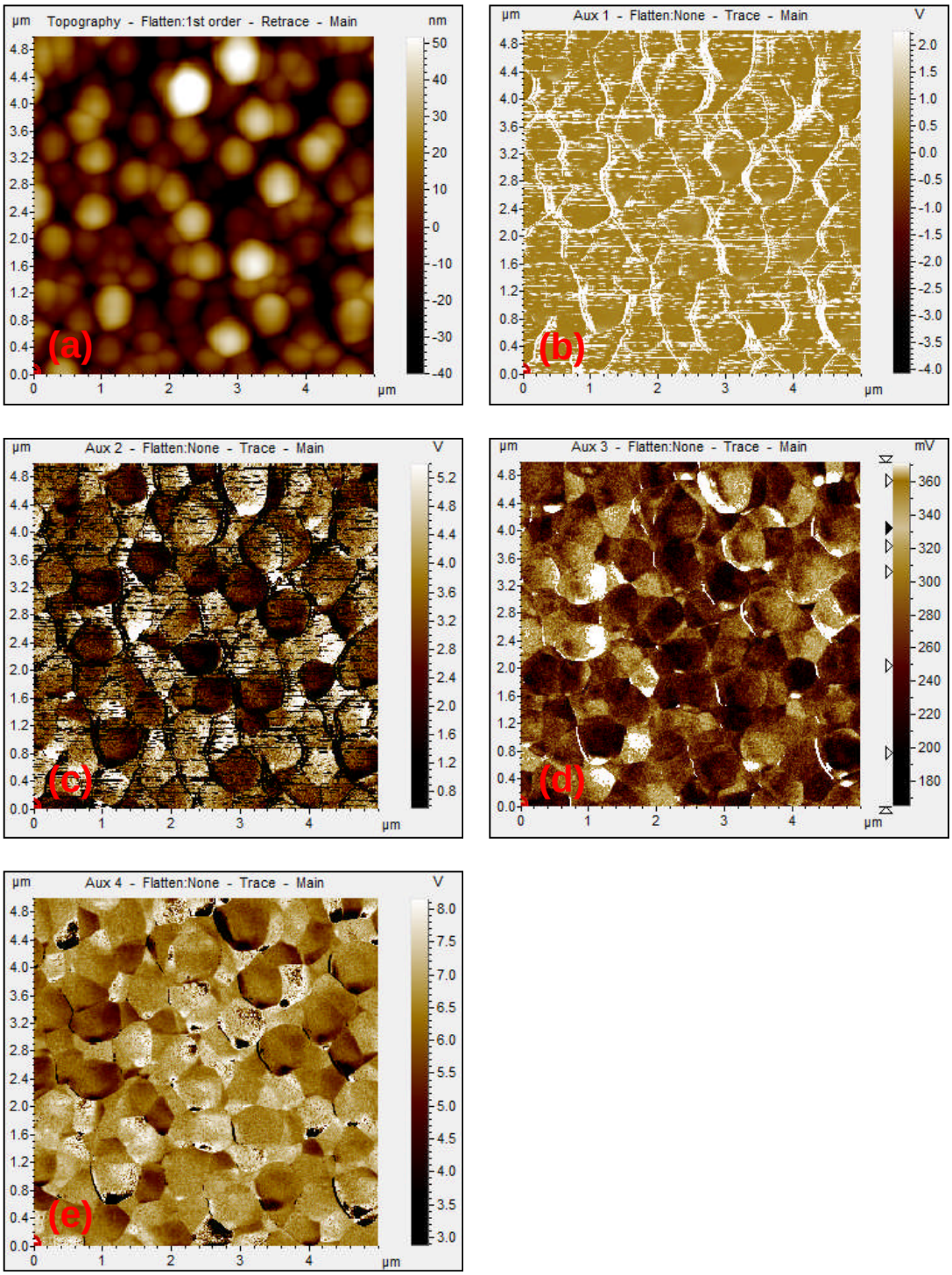

Figure. 5.17. AFM, PFM images of a 290 nm thin film of composition $0.7BiFeO_3$ - $0.3PbTiO_3$, on a preferentially orientated $Pt/TiO_x/SiO_2/Si$. (a) topography, (b)vertical amplitude, (c) vertical phase (d)lateral amplitude, (e) vertical phase.

5.2.5. TEM Analysis: Interdiffusion at the Substrate - Film Interface

To investigate why there is no piezoelectric response below 290 nm the films were analysed using transmission electron microscopy, energy dispersive x-ray analysis (TEM EDX analysis).

5.2.5.1. Background – Interdiffusion at the Substrate – Film Interface

The key component of an FeRAM non-volatile memory is a ferroelectric capacitor containing a ferroelectric thin film sandwiched by two platinum electrodes. However platinum is known as a catalytic active material for the degradation of electrical properties in ferroelectric materials (Niwa, 2000).

Many researchers (Sreenivas, 1994), (Lee, 1996), (Niwa, 2000), (Kim, 1997), (Vilquin, 2002) have reported on the suitability of platinum as a bottom electrode. They claim that degradation in the electrical properties can be caused by interactions at the interface and by the roughness of the electrode. Effects of the top electrode deposition and annealing on the ferroelectric properties have also been reported (Naik, 1992), (Ishihara, 1995).

Niwa describes the degradation of ferroelectric properties of PZT when deposited on platinum electrodes after annealing in a hydrogenous atmosphere (Niwa, 2000). The degradation has been attributed to the catalytic nature of platinum which dissociates H_2 into protons which then migrate into the PZT film, Niwa found that the lead from the PZT film diffuses into the platinum electrode.

Bursill characterised the interface of a Pt/PZT/Pt/TiO_2/SiO_2/Si by high resolution TEM. The pyrochlore phase $PbZrTiO_{7-x}$ ($x \neq 1$) was observed on the top surface of the PZT layer (Bursill, 1994).

The phenomenon of interdiffusion at the platinum-film interface has also been well reported for bismuth based films.

Seong reported on a $Bi_4Ti_3O_{12}$ or a $Bi_2Ti_4O_{12}$ secondary phase formed at the interface between $SrBiTaO_9$ (SBT) film and the Pt/TiO_2/SiO_2/Si substrate

during metal organic chemical vapour deposition (MOCVD) at 550 °C (Seong, 1998). The formation of $Bi_4Ti_3O_{12}$ was presumed to be caused by the reaction of accumulated bismuth out of the film with titanium out of the TiO_2 adhesion layer, which both diffuse through the platinum bottom electrode. The deterioration of the electrical properties in 40 nm films are associated with a thick $Bi_4Ti_3O_{12}$ interfacial diffusion layer.

Yakovlev investigated the platinum electrode top and bottom interface of $BiFeO_3$ thin films on $Pt/TiO_x/SiO_2/Si$ substrates prepared by chemical solution deposition (Yakovel, 2005). It was found that the $BiFeO_3$ film was depleted in bismuth and iron with respect to oxygen and segregation of iron and bismuth formed Bi_2O_3 with surface segregation. When annealed at 650 °C for 1 hour substantial interdiffusion at the film-substrate interface was detected with Pt-Fe and Pt-Bi intermetallic compounds being formed. The presence of the phases at the interface, in the form of a passive layer, is reported to disturb the film stoichiometry and structure which causes a deterioration of electrical properties.

5.2.5.2. TEM: Analysis of Interdiffusion

On analysis of the films using TEM EXD analysis it appears that all the films suffer significant interdiffusion at the substrate – film interface.

The EDX line scan in Figure. 5.17 shows the increase in bismuth concentration (relative to lead, titanium and iron) in the platinum bottom electrode layer. Figure. 5.17 demonstrates how films below the critical thickness suffer from interdiffusion of the bismuth (and possibly lead) into the platinum bottom electrode and therefore iron rich regions form within the deposited film (demonstrated by the increase in iron content in line scan when detecting in the deposited film).

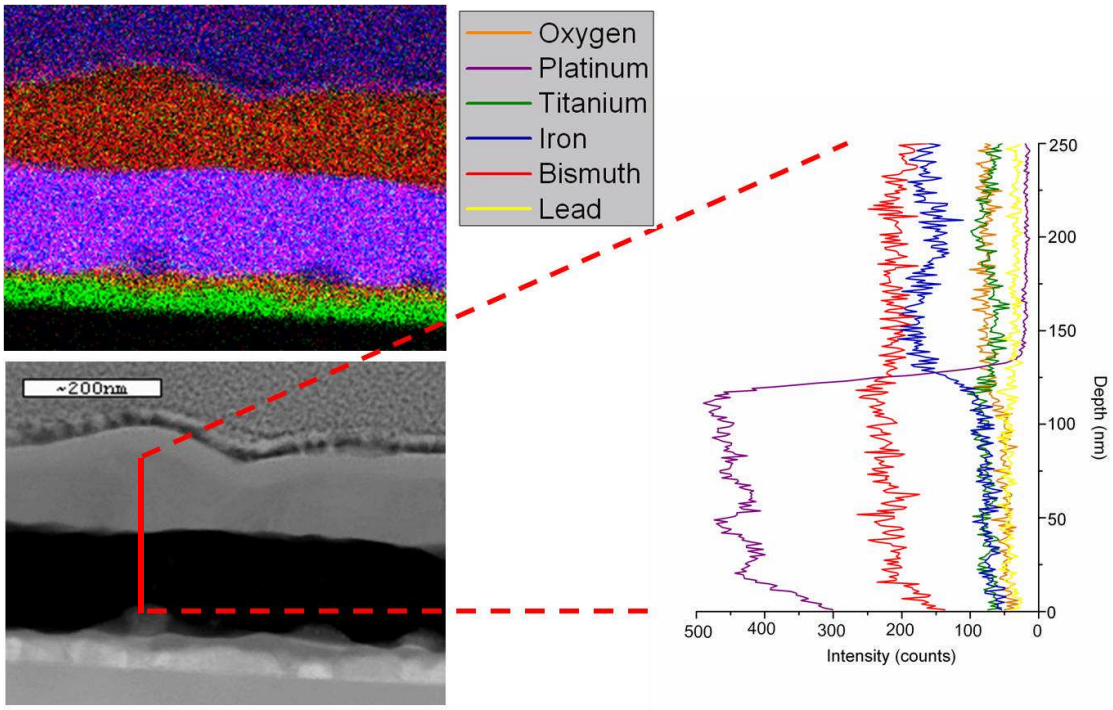

Figure. 5.18. TEM EDX analysis ~ 150 nm thick $0.7BiFeO_3$ - $0.3PbTiO_3$ film. Top left: EDX elemental map of the film with colour assigned to different elements, Bottom Left: TEM dark field image of film, Right: EDX analysis across the red line shown on the dark field image.

The bismuth and lead move through the entire platinum bottom electrode and sit just above the titanium adhesion layer. It appears that the bismuth moves through the platinum forming porous channels rather than a uniform rate of degradation on the top surface of the electrode. This interdiffusion results in a porous platinum layer that is unable to act as a bottom electrode.

It is only when the critical thickness is exceed that the films no longer suffer severe bismuth and lead loss throughout the entire film surface. Although the XRD traces in Figure 5.1 and 5.7 provide evidence for the presence of a secondary phase, at 290 nm the relative intensity of the corresponding peak has reduced compared to that seen if the thinner samples and therefore indicates that the secondary phase may be confined to certain areas rather than throughout the entire film. As PFM is a technique which measures interaction at the tip, the piezoelectric response observed in the 290 nm thin films indicates that top surface of the films no longer contains the non-

piezoelectric secondary phase, allowing the exposed $BiFeO_3$ - $PbTiO_3$ structure to produce a piezoelectric response. However even with increased thickness the damage to the platinum bottom electrode is already complete and will be unable to act as a bottom electrode therefore preventing the $0.7BiFeO_3$ - $0.3PbTiO_3$ film from sustaining ferroelectric polarization reversal.

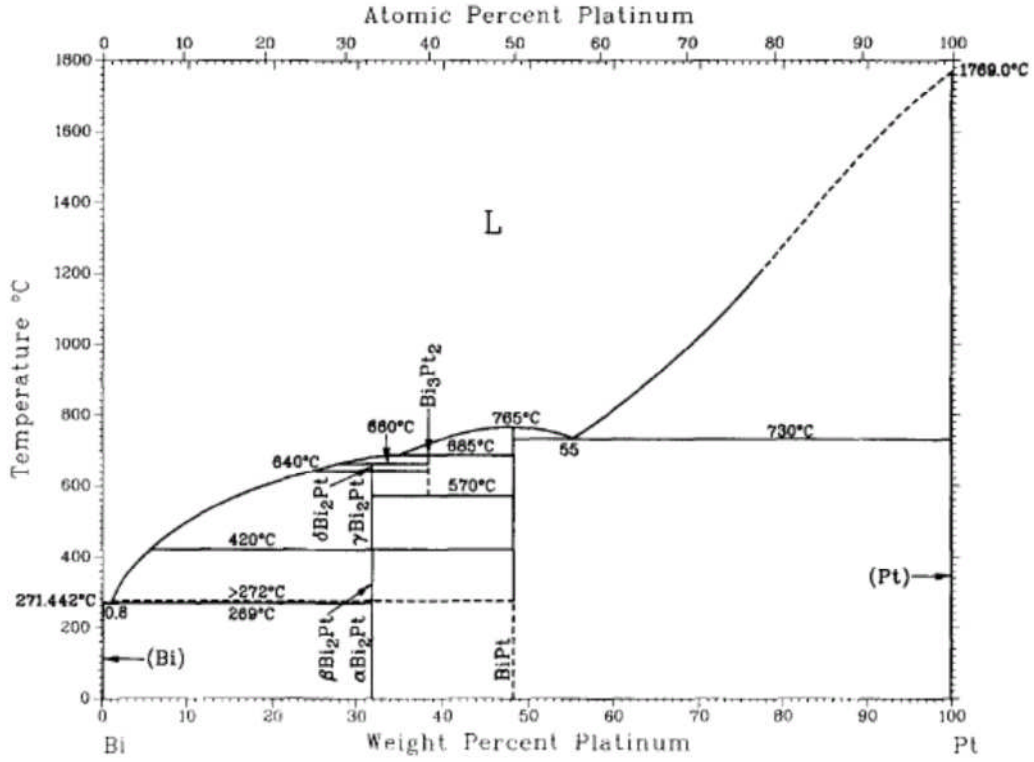

Figure. 5.19. Phase diagram of the bismuth – platinum system (Okamoto, 1991).

The interdiffusion can be explained using the platinum – bismuth phase diagram (Figure. 5.18). Bismuth has a low melting point of 271 °C therefore throughout the entire deposition process (565 °C) bismuth will remain in liquid form. When in contact with platinum a low melting point eutectic is present in the phase diagram and therefore a eutectic alloy will form. As bismuth will remain in the liquid form throughout the entire deposition process it will constantly react with the platinum. As the composition of platinum compared to bismuth increases, intermetallics such as δBi_2Pt, Bi_3Pt and γBi_2Pt will form. The excess bismuth will continue to react its way through the bottom electrode until no more platinum is present within the

system and / or the temperature is reduced therefore preventing the reaction. This results in a bismuth deficient film with iron rich phases present. These iron rich phases are detected in the XRD traces of the thinner films but not the thicker films. This is most likely because all the platinum has already been used up in the eutectic reaction and / or the bismuth is too far away from the platinum in the thicker films and / or the deposition temperature has been reduced before the reaction is complete. To prevent the reaction from occurring the deposition temperature must be reduced below ~ 271 °C but this will result in non-stoichiometric films as unbound deposited atoms re-evaporate from the surface of the substrate. Another option to prevent interdiffusion at the substrate – film interface is the use of a diffusion barrier layer between the deposited film and platinum substrate. This is covered in Chapter 6.

5.3. Conclusion

The $0.6BiFeO_3 – 0.4PbTiO_3$ films were all tetragonal with (001) preferential orientation due to the close matching lattice parameters with the underlying substrate at room temperature. The mis-match strain that partially arrives from the varying thermal expansion coefficients of the deposited film and substrate is compensated for by the development of (100) orientated grains. With increasing thickness the contribution from the (100) increases although the (001) remains the preferred orientation. The $0.7BiFeO_3 – 0.3PbTiO_3$ films are not orientated in one direction like the $0.6BiFeO_3 – 0.4PbTiO_3$ films however the structure is still substrate influenced, displaying tetragonal (100) and (111) preferential orientation. The identification of an extra peak in the x-ray traces suggests the films are tetragonal-rhombohedral mixed phase. The rhombohedral phase (100) becomes the most dominant phase at increased thickness at the film is unable to accommodate the strain at the substrate film interface.

At ~290nm both the $0.7BiFeO_3$ - $0.3PbTiO_3$ and $0.6BiFeO_3$ - $0.4PbTiO_3$ films go from being conductive (7 Ω) to resistive (~ 10 MΩ). This is due to the topography of the films structure where by the peak-to-trough distance of some grains can be equal to the thickness of the film. The Volmer-Weber island growth mechanism allows the $0.7BiFeO_3$ - $0.3PbTiO_3$ films develop a columnar polycrystalline structure and the $0.6BiFeO_3$ - $0.4PbTiO_3$ films develop a plate like polycrystalline structure with large peak-to-trough distances. This structure leaves the platinum bottom electrode exposed and results in a short circuit. Once the film thickness exceeds 290 nm additional ablated material from the laser plume fills any remaining holes between the grains therefore covering the platinum bottom electrode. Theoretically at a film thickness < 290 nm the films should be able to sustain a PE loop once the platinum bottom electrode is no longer exposed, however TEM EDX analysis confirms the occurrence of interdiffusion between the bismuth from the $0.7BiFeO_3 – 0.3PbTiO_3$ deposited film and the platinum from the bottom electrode therefore exposing a non-piezoelectric secondary phase at the substrate-film. The damage to the platinum bottom electrode by interdiffusion with the bismuth prevents it acting as a bottom electrode and therefore a

polarization – electric field hysteresis loop cannot be achieved even at increased thicknesses. It is only when the critical film thickness of 290 nm is exceeded that the bismuth present on the top surface of the deposited film no longer interacts with the platinum and leaves a pure perovskite $BiFeO_3$ - $PbTiO_3$ structure exposed at the film surface. It is this $BiFeO_3$ - $PbTiO_3$ perovskite structure that induces a piezoelectric response in films above 290 nm. The piezoelectric nature of the film has been confirmed by PFM measurements that analysis the interaction of the tip at the surface.

5.4. References

BAI, F., J. WANG, M. WITTIG, J. F. LI, N. WANG, A. P. PYATAKOV et al. (2005). Destruction of spin cycloid in (111)c-oriented BiFeO3 thin films by epitiaxial constraint: Enhanced polarization and release of latent magnetization. *Appl. Phys. Lett*. **86**(3), pp.032511-3032513

BURSILL, L. A., I. M. REANEY, D. P. VIJAY, S. B. DESU. (1994). Comparison of lead-zirconate-titanate thin-films on ruthenium oxide and platinum-electrodes. *J. Appl. Phys.* **75**(3), pp.1521-1525

DUTTA, B. N. (1962). Lattice constants and thermal expansion of silicon up to 900°C by X-ray method. *Physica. Status. Solidi. B.* **2**(8), pp.984-987

FISCHER, P., M. POLOMSKA, I. SOSNOWSKA, M. SZYMANSKI. (1980). Temperature dependence of the crystal and magnetic structures of $BiFeO_3$. *J. Phys. C: Solid State Phys.* **13**(10), pp.1931-1940.

ISHIHARA, K., T. ISHIKAWA, K. HAMADA, S. ONISHI, J. KUDO, K. SAKIYAMA. (1995). The degradation of ferroelectric properties of PZT thin films due to plasma damage. *Integrat. Ferroelectr.* **6**(1-4), pp.301

KHAN, M. A., T. P. COMYN, A. J. BELL. (2007a). Ferroelectric BiFeO3-PbTiO3 thin films on Pt/Si substrates. *Ultrasonics, Ferroelectrics and Frequency Control, IEEE Transactions.* **54**, pp.2583.

KHAN, M.A., T. P. COMYN, A. J. BELL. (2007b). Large remanent polarization in ferroelectric BiFeO3-PbTiO3 thin films on Pt/Si substrates. *Appl. Phys. Lett.* **91**(3), pp.032901.

KHAN, M. A., T. P. COMYN, A. J. BELL. (2008a). Growth and characterization of tetragonal bismuth ferrite-lead titanate thin films. *Acta Mater*. **56**(9), pp.2110.

KHAN, M. A., T. P. COMYN, A. J. BELL. (2008b). Leakage mechanisms in bismuth ferrite-lead titanate thin films on Pt/Si substrates. *Appl. Phys. Lett*. **92**(7), pp.072908.

KHAN, M. A. (2008c). *Preparation and properties of bismuth ferrite lead titanate thin films prepared by pulsed laser deposition*. PhD thesis, University of Leeds.

KIM, M-C., J-W. CHOI, S-J. YOON, K-H. YOON, H-J. KIM. (2002). Thickness dependence of $Pb(Zr_{0.52}Ti_{0.48})O_3$ Films Prepared by pulsed laser deposition. *Jpn. J. Appl. Phys.* **41**(6A), pp.3817-3821

KIM, S. T., H.H. KIM, M.Y. LEE, W.J. LEE. (1997). Investigation of Pt/Ti bottom electrodes for Pb(Zr,Ti)O3 films. *Jpn. J. Appl. Phys.* **36**(1A), pp.294-300

LEE, E. G., D.J. WOUTERS, G. WILLEMS, H.E. MAES. (1996). Voltage shift and deformation in the hysteresis loop of $Pb(Zr,Ti)O_3$ thin film by defects. *Appl. Phys. Lett.* **69** (9), pp.1223-1226

LIAN, L., R. SOTTOS. (2000). Effects of thickness on the piezoelectric and dielectric properties of lead zirconate titanate thin films. *J. Appl. Phys.* **87**(8), pp.3941-3949

NAIK, I. K., L.E. SANCHEZ, S.Y. WU, B.P. MADERIC. (1992). Improved switching endurance of lead zirconate-titanate capacitors for nonvolatile memory applications. *Integrat. Ferroelectr*. **2**(1-4), pp.133

NAGARAJAN, V., I. G. JENKINS, S. P. ALPAY et al. (1999). Thiockness dependence of structural and electrical properties in epitaxial lead zirconate titanate films. *J. Appl. Phys*. **86**(1), pp.595-602

NIWA, K., Y. KOTAKA, M. TOMOTANI, H. ASHIDA, Y GOTO, S. OTANI. (2000). Interface between electrode and PZT memory device. *Acta. Mater.* **48**(18-19), pp.47755-4762

OKAMOTO, H. (1991). The Bi-Pt (Bismuth-Platinum) System. *J. Phase. Equilib.* **12**(2), pp.207-210

SAI SUNDER, V. V. S. S., D. HALLIYAL, A. M. UMARJI. (1995). Investigation of tetragonal distortion in the BiFeO3 – PbTiO3 system by high temperature X-ray diffraction. *J. Mater. Res*. **10**(5), pp. 1301-1306.

SEONG, N. J., C. H. YANG, W. C. SHIN, S. G. YOON. (1998). Oxide interfacial phases and the electrical properties of SrBi2Ta2O9 thin films

prepared by plasma-enhanced metalorganic chemical vapor deposition. *Appl. Phys. Lett.* 72(11), pp.1374-1376

SINGH, V. R., S. KAR, A. GARG. (2008). Synthesis and characterization of solution processed $BiFeO_3$-$PbTiO_3$ thin films. *Indian J Eng Mater Sci.* **15**, pp.104-106

SREENIVAS, K., I. REANEY, T. MAEDER, N. SETTER, C. JAGADISH, R. G. ELLIMAN. (1994). Investigation of Pt/Ti bilayer metallization on silicon for ferroelectric thin film integration. *J. Appl. Phys.* **75**(1), pp.232-239

TYHOLDT, F., S. JORGENSEN, H FJELLVAG, A. E. GUNNAES. (2005). Synthesis of oriented $BiFeO_3$ thin films by chemical solution deposition: Phase, texture, and microstructural development. *J. Mater. Res.* **20**(8), pp.2127-2139.

VILQUIN, B., G. LE RHUN, R. BOUREGBA, G. POULLAIN, H. MURRAY. (1994). Effect of in situ Pt bottom electrode deposition and of Pt top electrode preparation on PZT thin films properties. *Appl. Surf. Sci. Mater.* **195**(1-4), pp.63-73

YAKOVLEV, S., J. ZEKONYTE, C-H. SOLTERBECK, M. ES-SOUNI. (2005). Interfacial effects on the electrical properties of multiferroic $BiFeO_3$/Pt/Si thin film hetrostructures. *Thin. Solid. Films.* **493**(1-2), pp.24-29

YUN, K. Y., D. KANASHIMA, M. NODA, M. OKUYAMA. (2004). Giant ferroelectric polarization beyond 150 μC/cm^2 in $BiFeO_3$ Thin Film. *Jpn. J. Appl. Phys.* **43**(5A), pp.L647-L648.

ZHONG, Z., Y. SUGIYAMA, H. ISHIWARA. (2008). Thickness dependences of Polarization Characteristics in Mn-substituted $BiFeO_3$ Films on Pt Electrodes. *Jpn. J. Appl. Phys.* **47**(8), pp.6448-6451

ZHU, X., D. WU, A. LI, Z. LIU, N. MING. (2008). Transmission Electron Microscopy Observations on the Interfacial Structures of the Pt/$SrBi_2Ta_2O_9$/Pt Thin-Film Capacitors Prepared by Metallo-Organic Decomposition. *J. Am. Ceram. Soc.* **91**(3), pp.979-985

Chapter 6

$SrRuO_3$ Interdiffusion Barrier Layer

This chapter starts by reporting on the pulsed laser deposition processing conditions of strontium ruthenate ($SrRuO_3$) buffer layers, which are commonly used in ferroelectric thin film structures. These reported conditions have been used to produce a strontium ruthenate buffer layer which was deposited on a $Pt/TiO_x/SiO_2/Si$ substrate prior to the pulsed laser deposition of a $BiFeO_3$ - $PbTiO_3$ film.

The later part of this chapter looks at the use of the strontium ruthenate buffer layer to prevent the interdiffusion that occurs at the substrate - film interface of $BiFeO_3$ - $PbTiO_3$ films on $Pt/TiO_x/SiO_2/Si$ substrates. The topography of the buffer layer also appears to affect the growth mechanism of the $BiFeO_3$ - $PbTiO_3$ film which is also discussed.

6.1. Background

A diffusion barrier layer is a material that is situated between a substrate and the deposited material in a thin film structure. It is used to prevent the occurrence of interdiffusion of specific elements within a substrate and thin film material.

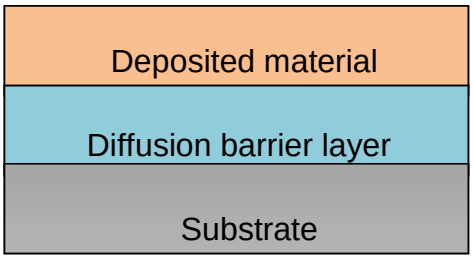

Figure. 6.1. Schematic of a thin film structure with an interdiffusion barrier layer.

However a suitable diffusion barrier layer is often selected not only on its ability to prevent interdiffusion between the substrate and thin film material but its structural capability, thermal stability and electrical properties between the two adjacent materials. A diffusion barrier layer that takes advantage of more than just its ability to prevent interdiffusion is often referred to as a *buffer layer* (Matsui, 2007), (Choi, 2007).

It is well reported that strontium ruthenate ($SrRuO_3$) is one of the good candidates for a diffusion barrier layer between bismuth and/or lead based materials and the underlying substrate where interdiffusion may occur (Choi, 2007), (Wu, 2004). As well as preventing interdiffusion $SrRuO_3$ is known to be one of the most suitable conductive oxides used as a bottom electrode for many ferroelectric (Gautreau, 2007) thin film structures. In addition $SrRuO_3$ exhibits several useful properties such as good electrical conductivity and thermal stability and is therefore often used as a buffer layer in ferroelectric thin films (Jiang, 1998), (Wu, 2004).

It is possible to control properties of $BiFeO_3$-$PbTiO_3$ films deposited on $Pt/TiO_x/SiO_2/Si$ substrates (discussed in chapter 5) using varying film thickness as well as the selection of orientated substrates that would

facilitate hetroepitaxial growth, whereby the interatomic spacing of the $BiFeO_3$-$PbTiO_3$ aligns with the underlying substrate structure. Therefore if control of a films structure is required the interatomic spacing of the buffer layer must be similar to the films which it is deposited on (Pintilie, 2009).

6.1.1. $SrRuO_3$ Structure

$SrRuO_3$ is a pseudo-cubic crystalline structure a = 3.930 Å calculated from the orthorhombic lattice parameters a = 5.567 Å, b = 5.530 Å, c = 7.845 Å (Jones 1989), (Bensch, 1990).

When $BiFeO_3$ - $PbTiO_3$ is deposited on $Pt/TiO_x/SiO_2/Si$ substrates the lattice parameters are able to accommodate the strain required to structurally align with the underlying platinum and produce preferentially orientated films (as shown in Chapter 5). As a result the lattice parameters of bulk $BiFeO_3$ - $PbTiO_3$ vary to those seen in thin films (Table. 6.1.).

Table. 6.1. Lattice Parameters of $BiFeO_3$ - $PbTiO_3$ in the bulk and thin film form.

	Bulk Lattice Parameters (Å)	120 nm thin film on $Pt/TiO_x/SiO_2/Si$ substrates (Å)
$0.6BiFeO_3$ - $0.4PbTiO_3$	a_{Tet} = 3.84 Å c_{Tet} = 4.44 Å	a_{Tet} = 3.90 Å c_{Tet} = 4.14 Å
$0.7BiFeO_3$ - $0.3PbTiO_3$	a_{Tet} = 3.82 Å c_{Tet} = 4.53 Å	a_{Tet} = 3.94 Å c_{Tet} = 4.13 Å

$BiFeO_3$ - $PbTiO_3$ is able to accommodate the strain required to produce preferentially orientated films by growing hetroepitaxialy on the underlying platinum structure. Therefore it is likely that the structure of the films can also be controlled when deposited on a $SrRuO_3$ buffer layer, as the lattice

parameters of $SrRuO_3$ are closer to bulk $BiFeO_3$ - $PbTiO_3$ than they are to platinum.

6.1.2. Pulsed Laser Deposition Conditions of $SrRuO_3$

The pulsed laser deposition conditions of $SrRuO_3$ as a buffer layer have been well reported by several research groups (Wu, 2004), (Lui, 1999), (Maria, 1998), (Son, 2007). Gautreau (2007) reported on a range of pulsed laser deposition conditions for $SrRuO_3$ where films deposited between 400 – 600 °C were amorphous and those deposited between 700 – 800 °C were highly dense crystalline films. However the films deposited at 800 °C produced extra peaks in the x-ray diffraction traces which were indexed as intermetallic phases. Films deposited at 700 °C produced high density single phase $SrRuO_3$ buffer layers with the lowest values of root mean squared surface roughness. Choi (2007) reported the optimum pulsed laser deposition conditions of $SrRuO_3$ buffer layers to be; 150 mTorr oxygen partial pressure, a laser frequency of 5Hz and a substrate temperature of 700 °C. These conditions produced single phase $SrRuO_3$ with the lowest root mean squared roughness of 14.08 nm.

These reported pulsed laser deposition conditions were used to produce the $SrRuO_3$ buffer layer on $Pt/TiO_x/SiO_2/Si$ substrates discussed in this chapter.

6.2. $SrRuO_3$ Buffer Layer on $Pt/TiO_x/SiO_2/Si$

The $SrRuO_3$ buffer layer was grown on $Pt/TiO_x/SiO_2/Si$ polycrystalline substrates by pulsed laser deposition (PLD) using a KrF Excimer Laser operated at a laser pulse frequency of 5 Hz. The laser fluence (energy density) on the $SrRuO_3$ target material was ~ 2 J cm^{-2}. The $Pt/TiO_x/SiO_2/Si$ substrate was placed parallel to the $SrRuO_3$ target at a fixed distance of 5 cm. A substrate temperature of 680 °C and oxygen partial pressure of 150 mTorr were chosen as the optimum processing conditions. Post deposition, the films were annealed for 10 minutes at 700 °C with an oxygen partial pressure of 250 mTorr and then cooled to room temperature at 15 °Cmin^{-1}.

The $SrRuO_3$ buffer layer thickness was measure at ~ 130 nm using cross sectional (fracture surface) scanning electron microscopy analysis (refer to Section. 3.2.4.2).

6.2.1. Buffer Layer - Structure and Morphology

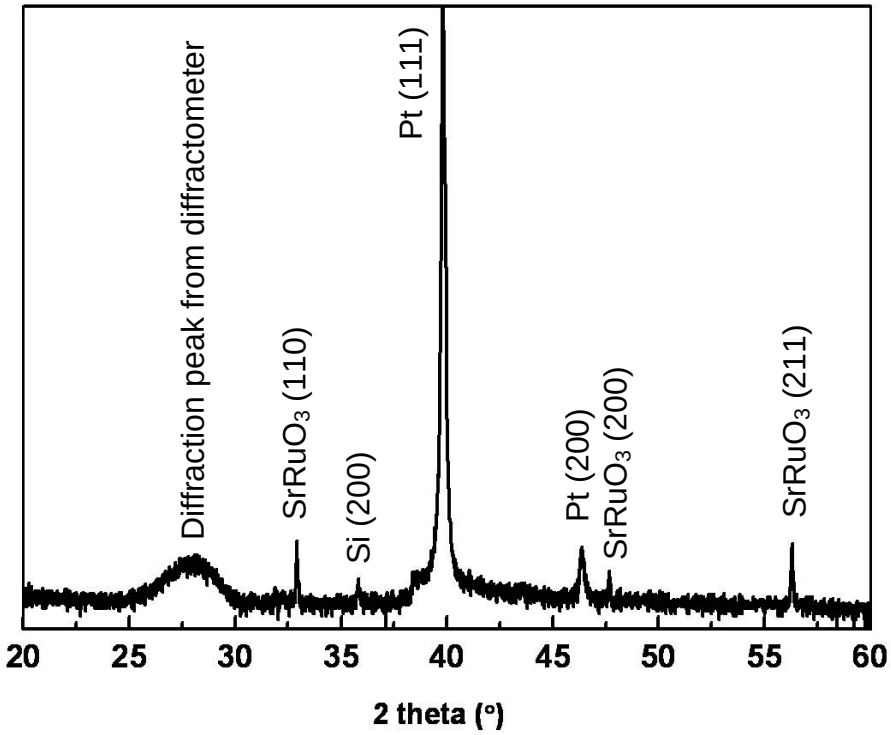

Figure. 6.2. XRD trace for ~ 130 nm $SrRuO_3$ buffer layer on a polycrystalline $Pt/TiO_x/SiO_2/Si$ substrate.

Figure. 6.2 shows a XRD θ-2θ scan for the $SrRuO_3$ buffer layer on a $Pt/TiO_x/SiO_2/Si$ substrate. The scans show low intensity peaks indicating the (110), (200) and (211) $SrRuO_3$ film reflections. The reflections of the $SrRuO_3$ buffer layer are properly indexed in the perovskite lattice (pseudo-cubic) with a = 0.393 nm) (Bensch, 1990). The buffer layer surface produces a polycrystalline XRD trace with the relative peak intensities being similar to that seen in powder diffraction and therefore there is no clear evidence of preferentially orientation within the buffer layer structure. There is no evidence of any secondary phases in the buffer layer or the presence of orthorhombic phase, which would have produced splitting of the (110)

pseudo-cubic reflection into three reflections (020), (112) and (200) (Jones 1989).

As the $BiFeO_3$ - $PbTiO_3$ film will be deposited on top of the $SrRuO_3$ buffer layer, the structure and morphology of the buffer layer's surface will influence the structure of the $BiFeO_3$ - $PbTiO_3$ deposited film. Therefore the root mean squared (RMS) roughness and surface morphology of the $SrRuO_3$ buffer layer needs to be investigated.

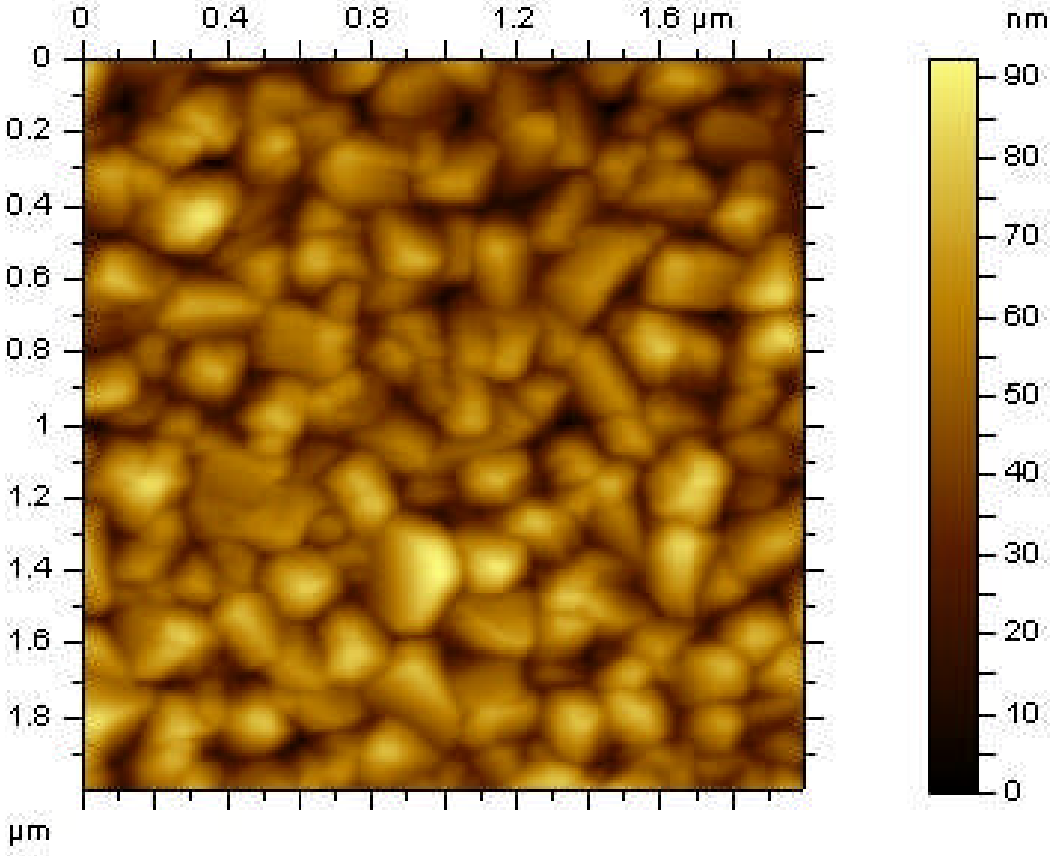

Figure. 6.3. 2D AFM 2 x 2 µm image of the surface of a ~ 130 nm $SrRuO_3$ buffer layer on a polycrystalline $Pt/TiO_x/SiO_2/Si$ substrate.

Figure. 6.3. shows the surface morphology and roughness of the $SrRuO_3$ buffer layer using atomic force microscopy (AFM). Figure. 6.4. shows the $SrRuO_3$ layer has a root mean square (RMS) roughness of 9.39 nm over a 2 µm x 2 µm scan area, which is higher than that seen in the $Pt/TiO_x/SiO_2/Si$ substrates. The surface topography profile indicates that the deposited buffer

layer has grown to form a crystalline columnar structure which is similar to that seen in $BiFeO_3$ - $PbTiO_3$ films on $Pt/TiO_x/SiO_2/Si$ substrates. The structure in the AFM image is also in agreement with the peak reflections identified in the XRD trace shown in Figure. 6.2.

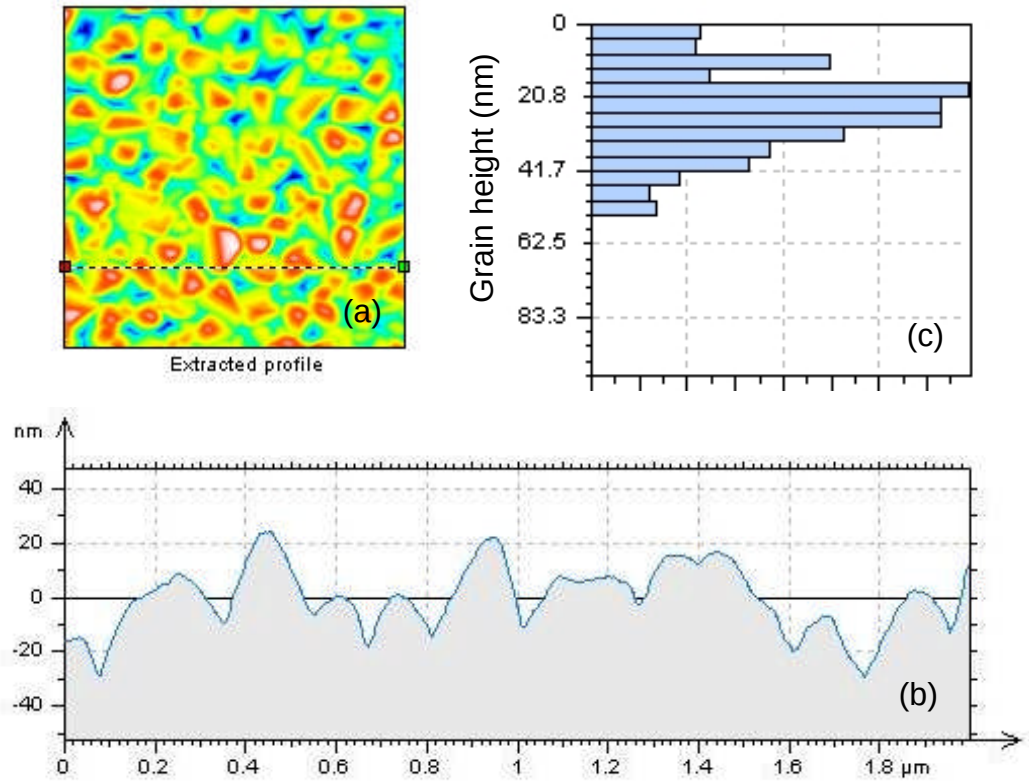

Figure. 6.4. (a) 2D AFM 2 x 2 µm image of the surface of a ~ 130 nm $SrRuO_3$ buffer layer on a polycrystalline $Pt/TiO_x/SiO_2/Si$ substrate (shown in Figure. 6.3) with a (b) profile plot of surface topography and (c) a histogram of the peak height distribution.

This crystalline columnar structure is similar to that seen in $BiFeO_3$ – $PbTiO_3$ thin films on $Pt/TiO_x/SiO_2/Si$ substrates (Chapter 5) and therefore it is likely that the columnar-like growth of $BiFeO_3$ - $PbTiO_3$ film should not be effected. Figure 6.4(c) shows the average peak height ~ 24 nm is smaller than that seen in $BiFeO_3$ - $PbTiO_3$ with a narrower distribution range (0 – 54 nm). These structural properties of the $SrRuO_3$ buffer layer should facilitate similar

growth conditions and structure of the $BiFeO_3$ - $PbTiO_3$ film to that seen on $Pt/TiO_x/SiO_2/Si$ substrates.

6.3. $BiFeO_3$ – $PbTiO_3$ Thin Film on $SrRuO_3$ – $Pt/TiO_x/SiO_2/Si$

A $0.7BiFeO_3 – 0.3PbTiO_3$ thin film was grown on top of the $SrRuO_3$ buffer layer by pulsed laser deposition (PLD) using a KrF Excimer Laser operated at the laser pulse frequency of 5 KHz. The laser fluence (energy density) on the target material was ~2 Jcm^{-2}. The substrate and buffer layer were placed parallel to the $0.7BiFeO_3 – 0.3PbTiO_3$ target material at a fixed distance of 5 cm. The optimum processing conditions for $0.7BiFeO_3 – 0.3PbTiO_3$ thin films (determined in Chapter 5) were used in this deposition process which include; a substrate temperature of 565 °C and oxygen partial pressure of 150 mTorr. The post deposition anneal temperature of 600 °C for 30 minutes was also carried out.

6.3.1. $BiFeO_3$ – $PbTiO_3$ Thin Film – Structure and Morphology

Figure. 6.5. shows a XRD θ - 2θ scan for $0.7BiFeO_3 – 0.3PbTiO_3$ thin film on a $SrRuO_3$ buffer layer on a polycrystalline $Pt/TiO_x/SiO_2/Si$ substrate. The scan shows low intensity peaks indicating (110) and (211) $SrRuO_3$ pseudo-cubic peak reflections. However the $SrRuO_3$ (200) peak reflection is not present in the XRD trace. As the $SrRuO_3$ (200) peak reflection had the lowest intensity of all the $SrRuO_3$ peak reflections (Figure. 6.2), it is not unexpected that it is not present in the $0.7BiFeO_3 – 0.3PbTiO_3$ XRD trace (Figure. 6.5) as only a limited intensity from the x-ray beam will reach the $SrRuO_3$ buffer layer through the deposited thin film.

The most intense peak for the $0.7BiFeO_3 – 0.3PbTiO_3$ powder diffraction is the (110) however Figure. 6.5. shows that (100) and (111) peaks are more intense than (110). The (111) peak reflection is the most intense of all the $0.7BiFeO_3 – 0.3PbTiO_3$ peaks, which indicated that the deposited film is preferentially (111) orientated with some (100) texture present within the deposited film. There is no evidence in the XRD trace (Figure. 6.5) of the (100) and (001) tetragonal peak reflections, only a single peak reflecting at ~ 22.4 2θ which is expected in the rhombohedral phase. The single peak reflection for the (111) also indicated the absence of the tetragonal phase.

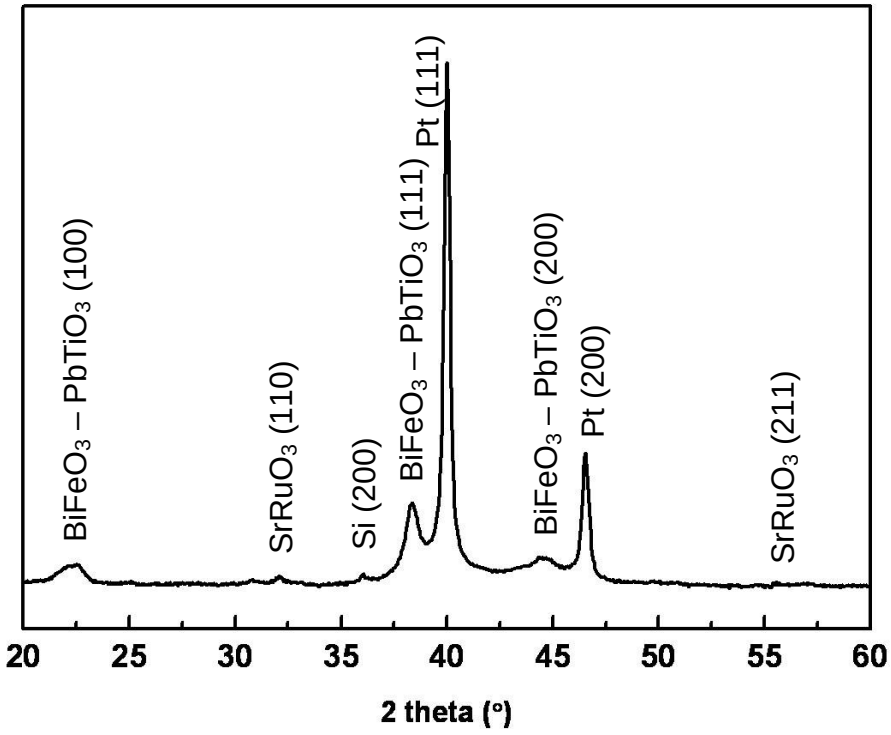

Figure. 6.5. XRD θ - 2θ scan for $0.7BiFeO_3 – 0.3PbTiO_3$ thin film on a $SrRuO_3$ buffer layer on a polycrystalline $Pt/TiO_x/SiO_2/Si$ substrate.

In Chapter 5 the $0.7BiFeO_3 – 0.3PbTiO_3$ films were preferentially (100) orientated with both the tetragonal and rhombohedral phase present due to hetroepiatxial growth on the (200) of the platinum. As the film thickness was increased the structure relaxed and the rhombohedral phase dominated, with the (111) orientation increasing in intensity. In this case the deposited film cannot grow hetroepitaxialy to the platinum substrate, instead it sits on the columnar $SrRuO_3$ structure and therefore the film takes the rhombohedral phase, which is most thermodynamically favorable at this composition and grows with a (111) preferentially oriented columnar structure influenced by the underlying buffer layer.

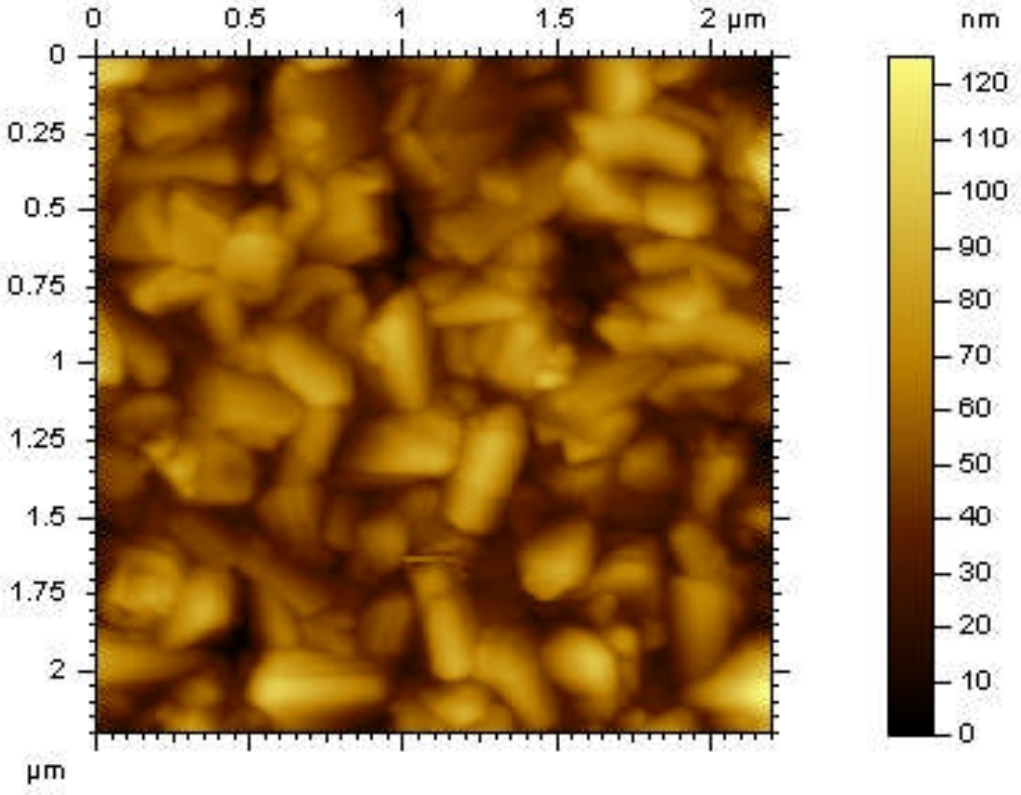

Figure. 6.6. 2D AFM 2 x 2 µm image of the surface of a $0.7BiFeO_3$ – $0.3PbTiO_3$ thin film on a $SrRuO_3$ buffer layer on a polycrystalline $Pt/TiO_x/SiO_2/Si$ substrate.

Figure. 6.6 shows the surface morphology and roughness of the $0.7BiFeO_3$ – $0.3PbTiO_3$ deposited film using atomic force microscopy (AFM). Figure 6.7 shows that the $0.7BiFeO_3$ – $0.3PbTiO_3$ film has grown to form a columnar (111) oriented structure with a RMS roughness of 13.9 nm over a 2µm x 2µm scan area. This is less than that seen in $0.7BiFeO_3$ – $0.3PbTiO_3$ on $Pt/TiO_x/SiO_2/Si$ substrates (refer to Chapter 5) which may be due to the underlying $SrRuO_3$ buffer layer morphology. Chapter 5 describes the deposited films growth mechanism as the Volmer-Weber island formation (Section. 4.2.1.) whereby an island forms and as further material is deposited it nucleates between the islands, resulting in a reduced peak-to-trough distance and lower RMS roughness.

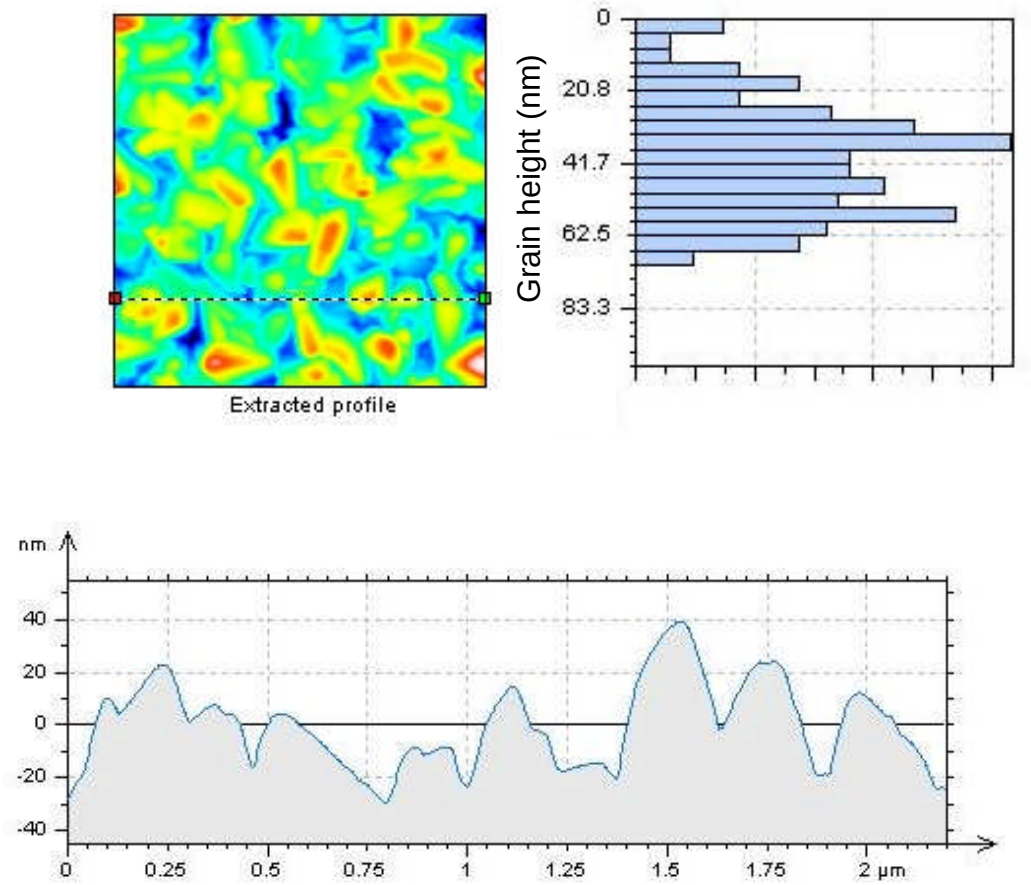

Figure. 6.7. (a) 2D AFM 2 x 2 µm image of the surface of $0.7BiFeO_3$ – $0.3PbTiO_3$ thin film on a $SrRuO_3$ buffer layer on a polycrystalline $Pt/TiO_x/SiO_2/Si$ substrate (shown in Figure. 6.6) with a (b) profile plot of surface topography and (c) a histogram of the peak height distribution.

The grain size shown in Figure. 6.7. is similar to that seen in $0.7BiFeO_3$ – $0.3PbTiO_3$ thin film on $Pt/TiO_x/SiO_2/Si$ however the grain height distribution is much narrower.

It is interesting to note that this reduction in the RMS roughness of the $0.7BiFeO_3$ – $0.3PbTiO_3$ thin film results in a resistive thin film material for at ~130 nm film thickness. In $0.7BiFeO_3$ – $0.3PbTiO_3$ thin films on $Pt/TiO_x/SiO_2/Si$ substrates (Chapter 5) the films were only resistive when the film thickness was above 290 nm. This is likely to be due to the influence of the underlying $SrRuO_3$ buffer layer's structure and morphology and its effect on the $0.7BiFeO_3$ – $0.3PbTiO_3$ deposited thin film.

6.3.2. TEM Analysis of Interdiffusion

To investigate whether the strontium ruthenate buffer layer prevents the interdiffusion that occurs at the substrate - film interface of $BiFeO_3$ - $PbTiO_3$ films on $Pt/TiO_x/SiO_2/Si$ substrates, cross sectional DF-TEM EDX mapping has been carried. Figure. 6.8. and 6.9 show the EDX elemental map on a DF-TEM image of $0.7BiFeO_3 – 0.3PbTiO_3$ thin film on a $SrRuO_3$ buffer layer on a polycrystalline $Pt/TiO_x/SiO_2/Si$ substrate cross section. Colours have been assigned to the different elements; red = titanium, blue = strontium and yellow = platinum. The figures show that the $SrRuO_3$ buffer layer has prevented the bismuth within the deposited film from moving through the platinum bottom electrode and therefore the electrode has remained crystalline with no porosity.

As can be seen from Figure. 6.8, although the $SrRuO_3$ has prevented the bismuth from moving through the platinum bottom electrode, local diffusion appears to have occurred within the $0.7BiFeO_3 – 0.3PbTiO_3$ deposited film. To analysis this local diffusion in further detail DF-TEM imaging was carried out at higher magnification on cross sections of the $SrRuO_3$ and $0.7BiFeO_3 – 0.3PbTiO_3$ deposited film (Figure. 6.10 and 6.11.)

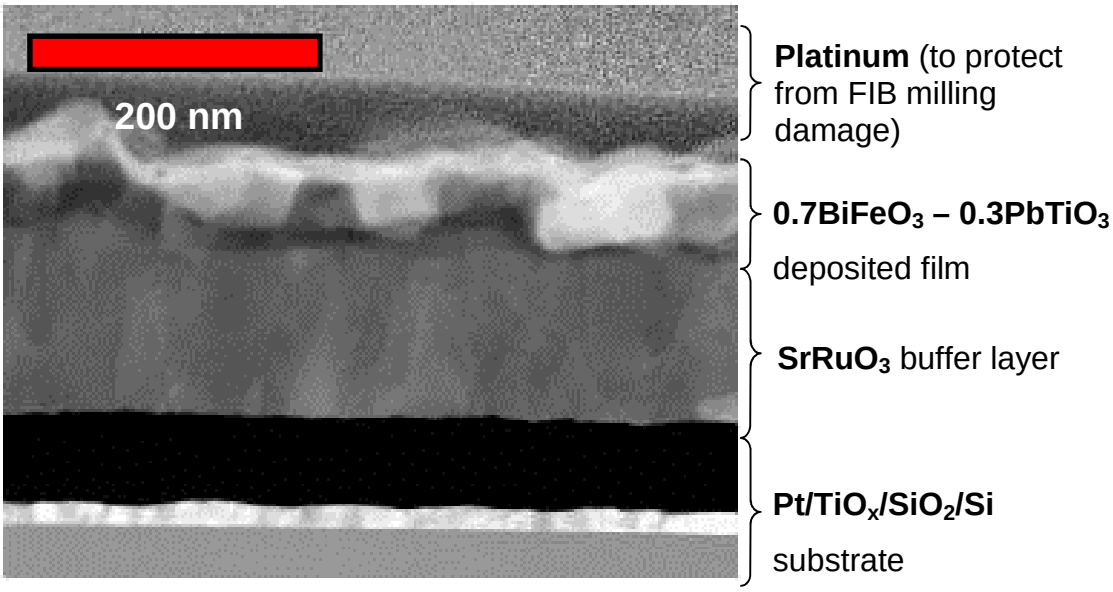

Figure. 6.8. DF-TEM image of 0.7$BiFeO_3$ – 0.3$PbTiO_3$ thin film on a $SrRuO_3$ buffer layer on a polycrystalline Pt/TiO_x/SiO_2/Si substrate cross section.

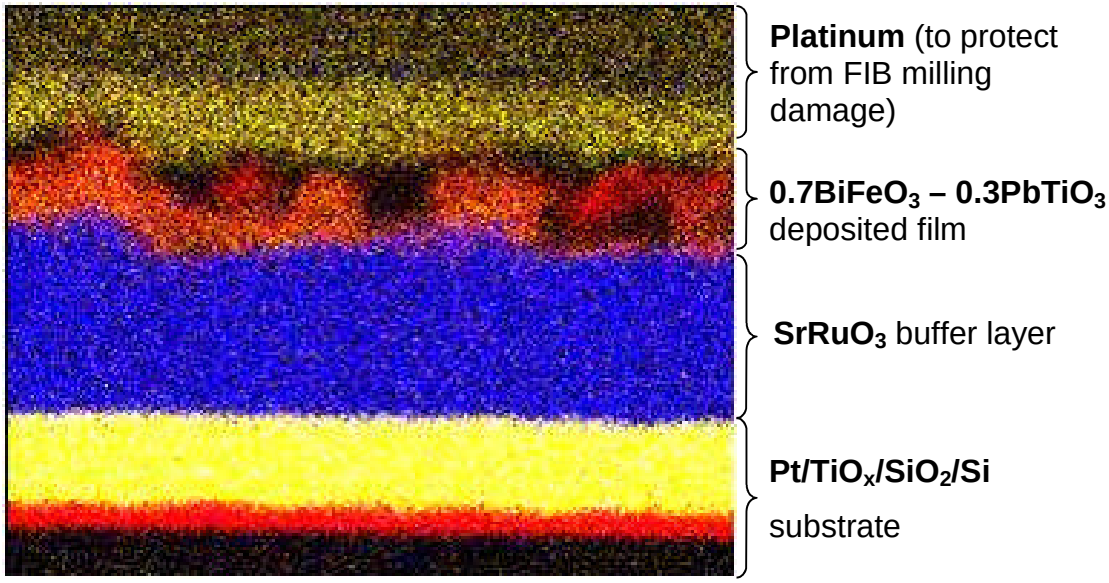

Figure. 6.9. EDX elemental map on a DF-TEM image of 0.7$BiFeO_3$ – 0.3$PbTiO_3$ thin film on a $SrRuO_3$ buffer layer on a polycrystalline Pt/TiO_x/SiO_2/Si substrate cross section (red = titanium, blue = strontium and yellow = platinum).

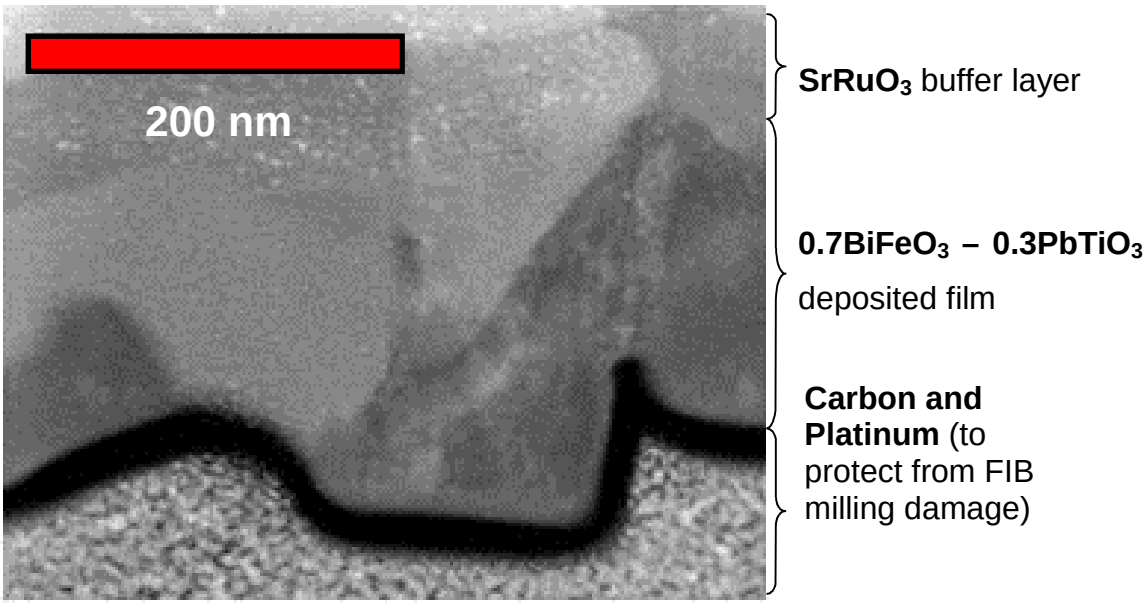

Figure. 6.10. Higher magnification DF-TEM image of $0.7BiFeO_3 – 0.3PbTiO_3$ thin film on a $SrRuO_3$ buffer layer on a polycrystalline $Pt/TiO_x/SiO_2/Si$ substrate cross section.

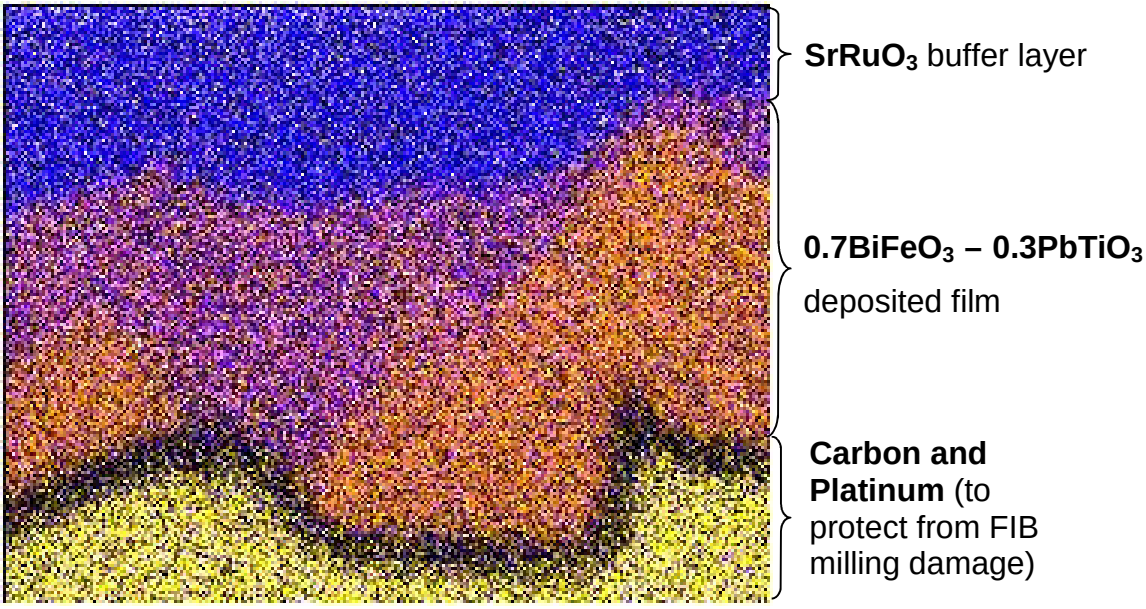

Figure. 6.11. Higher magnification EDX elemental map on a DF-TEM image of $0.7BiFeO_3 – 0.3PbTiO_3$ thin film on a $SrRuO_3$ buffer layer on a polycrystalline $Pt/TiO_x/SiO_2/Si$ substrate cross section (purple = bismuth, orange = iron, blue = strontium and yellow = platinum).

Figure. 6.10. and 6.11. show bismuth rich regions (purple colour on Figure. 6.11) have formed close to the $SrRuO_3$ buffer layer and iron rich regions (orange colour on Figure. 6.11) have formed at the top of the deposited film. Therefore local interdiffusion within the deposited $0.7BiFeO_3 – 0.3PbTiO_3$ thin film has occurred, whereby the bismuth has moved towards the platinum but not reacted with it due to the presence of the $SrRuO_3$ buffer layer.

6.4. Conclusion

A ~ 130 nm $SrRuO_3$ buffer layer was grown on a $Pt/TiO_x/SiO_2/Si$ substrate using pulsed laser deposition (PLD). The buffer layer formed a crystalline columnar structure with a RMS roughness of 9.39 nm over a 2 µm x 2 µm area and an average peak height of ~ 24nm. The structure was indexed as a perovskite pseudo-cubic. The structure and morphology of the $SrRuO_3$ buffer layer appears to allow the PLD deposited $0.7BiFeO_3 – 0.3PbTiO_3$ thin film to grow in the Volmer-Weber island formation between the columnar $SrRuO_3$ grains. Once the $SrRuO_3$ troughs were filled with $0.7BiFeO_3 – 0.3PbTiO_3$ deposited material, any further deposited material begins to form its own columnar structure with no exposed underlying $SrRuO_3$. This results in the growth of a resistive film at ~ 130 nm thickness (much lower than the ~290 nm required to form a resistive film of $0.7BiFeO_3 – 0.3PbTiO_3$ on $Pt/TiO_x/SiO_2/Si$ substrates).

To investigate whether the $SrRuO_3$ buffer layer prevents the interdiffusion that occurs at the substrate – film interface of $0.7BiFeO_3 – 0.3PbTiO_3$ thin films on $Pt/TiO_x/SiO_2/Si$ substrates, cross sectional TEM EDX mapping was carried out. The maps confirm that the presence of the $SrRuO_3$ buffer layer prevents interdiffusion of the bismuth (from the deposited film) and platinum (from the bottom electrode). However the maps describe local diffusion of the bismuth towards the $SrRuO_3$ buffer layer and iron rich regions at the surface of the deposited film. Therefore although the $SrRuO_3$ buffer layer does prevent interdiffusion between the substrate and the film, the bismuth still appears to readily segregate from the other elements in the film towards the substrate.

6.5. References

BENSCH, W., H. W. SCHMALLE, A. RELLER. (1990). Structure and thermochemical reactivity of $CaRuO_3$ and $SrRuO_3$. *Solid. State. Ionics.* **43**, pp. 171

CHOI, M. R., W. JO, Y. S. OH, K. H. KIM, Y. M. KANG, et al. (2007). Structural and electrical properties of $SrRuO_3$ thin films for buffer layers of coated conductors. *Physica D.* **463-465**, pp. 584-588.

DUVAL, F. F. C., R. A. DOREY, R. H. HAIGH, R. W. WHATMORE. (2003). Stable TiO_2/Pt electrode structure for lead containing ferroelectric thick films on silicon MEMS structures. *Thin Solid Films.* **444**, pp. 235-240.

GAUTREAU, O., C. HARNAGEA, F. NORMANDIN, T. VERES, A. PIGNOLET. (2007) Structural and electrical properties of room temperature pulsed laser deposited and post-annealed thin $SrRuO_3$ films. *Thin. Film. Solids.* **515**, pp. 4580-4587.

JIANG, J. C., X. Q. PAN, C. L. CHEN. (1998). Microstructure of epitaxial $SrRuO_3$ thin films on (001) $SrRuO_3$. *Appl. Phys. Letts.* **72**(8), pp. 909-911.

JONES, C.W., P. D. BATTLE, P. LIGHTFOOT, W. T. A. HARRISON. (1989). The structure of $SrRuO_3$ by time-of-flight neutron powder diffraction. *Acta. Crystallogr. C.* **45**, pp. 365

LUI, K. S., Y. J. CHEN, G. JAMN. (1999). $(Pb_{1-x}\ La_x)(Zr_{1-y}\ Ti_y)O_3$ patterns on Pt-coated silicon prepared by pulsed laser deposition. *Appl.Phy. Lett.* **75**(17), pp. 2647-2649.

MARIA, J. P., S. TROLLIER-MCKINSTRY, D. G. SCHLOM. (1998). The influence of energetic bombardment on the structure and properties of epitaxial $SrRuO_3$ thin film grown by pulsed laser deposition. *J. Appl. Phys.* **83**(3), pp. 4373-4379.

MATSUI, Y., K. TORII, K. KUSHIDA, H. MIHI, Y. FUJISAKI. (1997). Highly Oxidation-Resistant TiN Barrier Layers for Ferroelectric Capacitors. *Jap. J. Appl. Phys.* **36**, pp. 1586-1588.

PINTILIE, L., C. DRAGOI, Y. H. CHU, L. W. MARTIN, R. RAMESH, M. ALEXE. (2009). Orientation-dependent potential barriers in case of epitaxial Pt-$BiFeO_3$-$SrRuO_3$ capacitors. *Appl. Phys. Lett.* **94**, pp. 2329021-2329023.

SON, J. Y., B. G. KIM, J. H. CHO. (2007). Thin film growth of epitaxial, polycrystalline and amorphous $SrRuO_3$. *Thin Solid Films.* **515**, pp. 7086-7090.

WU, T. J., D. S. TSAI. (2004). Structure and properties of PZT thin films on strontium ruthenate and calcium ruthenate electrodes. *Materials Chemistry and Physics.* **85**, pp. 88-95.

Chapter 7

Summary and Conclusions

In this work a structural study was carried out of $xBiFeO_3 – (1-x)PbTiO_3$ thin films deposited by pulsed laser deposition around the morphotropic phase boundary (MPB). The effect of substrate orientation, changing composition and varying film thickness were described as well as the growth mechanisms and interactions at the film – substrate interface.

The optimisation of pulsed laser deposition (PLD) conditions for $BiFeO_3 – PbTiO_3$ thin films on $Pt/TiO_x/SiO_2/Si$ substrates was carried out. Good quality, pure phase $BiFeO_3 – PbTiO_3$ thin films were produced using a KrF Excimer Laser with the following processing conditions; a pulse frequency of 5 Hz, substrate temperature of 565 °C, substrate – target distance of 5 cm, laser fluency of 2.3 Jcm^{-2}, oxygen partial pressure of 75 mTorr and post deposition anneal temperature of 600 °C for 30 minutes.

The structural properties of $xBiFeO_3 – (1-x)PbTiO_3$ thin films as a function of thickness, composition and substrate orientation were analysed for two compositions either side of the nominal MPB, where x = 0.6 and 0.7. The $0.6BiFeO_3 – 0.4PbTiO_3$ thin films on polycrystalline $Pt/TiO_x/SiO_2/Si$ substrates were all tetragonal with (001) preferential orientation due to the close matching lattice parameters with the underlying substrate at room temperature. The mis-fit strain that partially arrives from the varying thermal expansion coefficients of the deposited film and substrate was compensated for by the development of (100) orientated grains. With increasing thickness the contribution from the (100) increases although the (001) remains the preferred orientation. The $0.7BiFeO_3 – 0.3PbTiO_3$ films on polycrystalline $Pt/TiO_x/SiO_2/Si$ substrates were not orientated in one direction however the structure was still substrate influenced, displaying tetragonal (100) and (111) preferential orientation. The identification of an extra peak in the x-ray traces suggested the films are tetragonal - rhombohedral mixed phase. The rhombohedral phase (100) became the most dominant phase at increased thickness as the film was unable to accommodate the strain at the substrate film interface. $0.7BiFeO_3 – 0.3PbTiO_3$ thin films on (111) orientated

$Pt/TiO_x/SiO_2/Si$ substrates show (111) preferred orientation in the thinner films however the films lattice parameters are closely matched to the relaxed bulk $0.7BiFeO_3 – 0.3PbTiO_3$ lattice parameters. This indicated that the films are unable to withstand the high strain required to grow hetroepitaxialy to the (111) of the platinum substrate and take on a more relaxed tetragonal phase even at the lower thicknesses. As the thickness is increased the films exhibit an enhanced (100) and (110) texture. This suggests that the development of the (111) orientation in thinner films is nucleation controlled whilst the formation of the (100) and (110) orientation in thicker films is growth controlled. Unlike the $0.7BiFeO_3$ - $0.3PbTiO_3$ films on polycrystalline $Pt/TiO_x/SiO_2/Si$ substrates, there is no evidence of a rhombohedral phase being present. As the films arrange in a relaxed polycrystalline state, there is no need for the rhombohedral phase to be present to accommodate the strain.

At ~290 nm both the $0.7BiFeO_3$ - $0.3PbTiO_3$ and $0.6BiFeO_3$ - $0.4PbTiO_3$ films go from being conductive (7 Ω) to resistive (~ 10 MΩ). This is due to the topography of the the films structure whereby the peak-to-trough distance of some grains can be equal to the thickness of the film. The Volmer-Weber island growth mechanism allows the $0.7BiFeO_3$ - $0.3PbTiO_3$ films to develop a columnar polycrystalline structure and the $0.6BiFeO_3$ - $0.4PbTiO_3$ films develop a plate like polycrystalline structure with large peak-to-trough distances. This structure leaves the platinum bottom electrode exposed and results in a short circuit. Once the film thickness exceeds 290 nm additional ablated material from the laser plume fills any remaining holes between the grains therefore covering the platinum bottom electrode. Theoretically at a film thickness < 290 nm the films should be able to sustain a PE loop once the platinum bottom electrode is no longer exposed, however TEM EDX analysis confirms the occurrence of interdiffusion between bismuth from the $0.7BiFeO_3 – 0.3PbTiO_3$ deposited film and platinum from the bottom electrode, therefore exposing a non-piezoelectric secondary phase at the substrate-film. The damage to the platinum bottom electrode by interdiffusion with the bismuth prevents it acting as a bottom electrode and therefore a

polarization – electric field hysteresis loop cannot be achieved even at increased thicknesses. It is only when the critical film thickness of 290 nm is exceeded that the bismuth present on the top surface of the deposited film no longer interacts with the platinum and leaves a pure perovskite $BiFeO_3$ - $PbTiO_3$ structure exposed at the film surface. It is this $BiFeO_3$ - $PbTiO_3$ perovskite structure that induces a piezoelectric response in films above 290 nm. The piezoelectric nature of the film was been confirmed by PFM measurements.

In an attempt to prevent the interdiffusion between bismuth and platinum, a ~ 130 nm $SrRuO_3$ buffer layer was grown on a $Pt/TiO_x/SiO_2/Si$ substrate using pulsed laser deposition (PLD). The buffer layer formed a crystalline columnar which was indexed as a perovskite pseudo-cubic. The structure and morphology of the $SrRuO_3$ buffer layer appears to allow the PLD deposited $0.7BiFeO_3 – 0.3PbTiO_3$ thin film to grow in the Volmer-Weber island formation between the columnar $SrRuO_3$ grains. Once the $SrRuO_3$ troughs were filled with $0.7BiFeO_3 – 0.3PbTiO_3$ deposited material, any further deposited material begins to form its own columnar structure with no exposed underlying $SrRuO_3$. This results in the growth of a resistive film at ~ 130 nm thickness (much lower than the ~290 nm required to form a resistive film of $0.7BiFeO_3 – PbTiO_3$ on $Pt/TiO_x/SiO_2/Si$ substrates).

To investigate whether the $SrRuO_3$ buffer layer prevents the interdiffusion that occurs at the substrate – film interface of $0.7BiFeO_3 – 0.3PbTiO_3$ on $Pt/TiO_x/SiO_2/Si$ substrates, cross sectional TEM EDX mapping was carried out. The maps confirmed that the presence of the $SrRuO_3$ buffer layer prevents interdiffusion of the bismuth (from the deposited film) and platinum (from the bottom electrode). However the maps describe local diffusion of the bismuth towards the $SrRuO_3$ buffer layer and iron rich regions at the surface of the deposited film. Therefore although the $SrRuO_3$ buffer layer does prevent interdiffusion between the substrate and the film, the bismuth still appears to readily segregate from the other elements in the film towards the substrate.

This thesis has addressed all the aims and objectives laid out in Section. 1.2. providing a detailed structural study of $xBiFeO_3 – (1-x)PbTiO_3$ thin films on

$Pt/TiO_x/SiO_2/Si$ substrates as a function of thickness, composition and substrate orientation. Therefore this work presents a platform for future work to be carried out which would exploit $xBiFeO_3 – (1-x)PbTiO_3$ thin films in applications for scalable high density memory devices as well as multiferroics.

Chapter 8

Future Work

This work reports on the pulsed laser deposition of $xBiFeO_3 – (1-x)PbTiO_3$ (x = 0.6 and 0.7) thin films either side of the morphotropic phase boundary (MPB) on $Pt/TiO_x/SiO_2/Si$ substrates. This work confirms how a deposited film's structural properties can be tailored using varying film thickness, changing composition as well as substrate orientation and resulting mis-fit strain. These findings coupled with existing literature reporting multiferroic properties in the bulk counterparts (Stevenson, 2010) (Fedulov, 1964) and high switchable polarization in weakly textured films (Khan, 2007), highlight the potential of $xBiFeO_3 – (1-x)PbTiO_3$ films for a number of research directions.

8.1. Research Directions

There are several research directions that can be explored as a result of this work. Some of the key research directions are described below. Although one of the future research directions is the analysis of any possible leakage currents and electrical properties of the films, this is secondary to the work that would need to be carried out in the first instance relating to understanding an optimising the growth conditions of polycrystalline and epitaxial films. The desire to investigate the electrical or magnetic properties of the films is subject to the potential application which the films are designed for.

1) *Polycrystalline Films*

   To evaluate and optimize the electrical properties of polycrystalline $BiFeO_3 – PbTiO_3$ thin films as a function of thickness, composition and substrate orientation. Over the past decade materials that offer a high switchable polarization compared to the commercially used PZT have received interest due to their potential use as a scalable high density memory device. This proposed work would allow the electrical properties to be tailored through controlled structure with a view to their potential use as a competitive scalable high density memory device.

2) *Leakage Currents in Polycrystalline Films*

$BiFeO_3$ based materials suffer from low resistivity and high electric coercive field, with the low resistivity of $BiFeO_3$ making the observation of the ferroelectric polarization – electric field hysteresis loop difficult (Cheng, 2003) (Cheng, 2003b). Further work is required to evaluate the levels of leakage currents in polycrystalline $BiFeO_3$ – $PbTiO_3$ thin films, especially around the critical thickness (290 nm) where no shorts are present as a result of the columnar structure. In attempt to solve the leakage current problems in $BiFeO_3$, doping with various ions on both the A and B-site of the $BiFeO_3$ structure has been employed. Further work is therefore required to evaluate the effect of various dopants (e.g. Ti, Mn, Nb) on the ferroelectric properties of the films (Qi, 2005). The aim of this work would be to improve the overall electrical properties of the polycrystalline $BiFeO_3$ – $PbTiO_3$ thin films with emphasis on reducing the leakage currents.

3) *Epitaxial Films and Multiferroics*

To evaluate and optimize the epitaxial growth of the $BiFeO_3$ – $PbTiO_3$ thin films on various substrates ($SrTiO_3$, $LaAlO_3$) deposited by pulsed laser deposition. This proposed work will help establish the relationship between choice of substrate and orientation in films as a function of mis-fit strain around the MPB. The work carried out in this thesis confirms the presence of both the tetragonal and rhombohedral phase in various polycrystalline $BiFeO_3$ – $PbTiO_3$ thin films. The overall aim of this proposed work would be to deposit epitaxial films of one orientation and phase on the edge of the tetragonal – rhombohedral structural instability. The application of an electric field to such films should readily allow switching between the rhombohedral and tetragonal phase. Switching across the MPB is of relevant interest as it offers the opportunity to exploit three different order parameters, with the rhombohedral form being antiferromagnetic, the tetragonal form being paramagnetic and both forms ferroelectric at room temperature. This would lead to developments in spintronic devices for sensing, data storage and signal processing.

8.2. References

CHENG, J., N. LI, L .E. CROSS. (2003). Structural and dielectric properties of Ga-modified BiFeO3 – PbTiO3 crystalline solutions. *J. Appl. Phys*. **94**(8), pp. 5153-5157.

CHENG, J., L .E. CROSS. (2003b). Effects of La substitution on ferroelectric rhombohedral/tetragonal morphotropic phase boundary in (1-x)(Bi,La)($Ga_{0.05}Fe_{0.95}$)O_3 – x$PbTiO_3$ piezoelectric ceramics. *J. Appl. Phys*. **94**(8), pp. 5188-5191.

KHAN, M. A., T. P. COMYN, A. J. BELL. (2007). Large remanent polarization in ferroelectric $BiFeO_3$-$PbTiO_3$ thin films on Pt/Si substrates. *Appl. Phys. Lett.* **91**(3), pp.032901.

STEVENSON, T. J. (2010). *Magnetic and electric properties of bismuth ferrite lead titanate ceramics*. PhD thesis, University of Leeds, (White Rose eThesis).

QI, X. J. DHO, R. TOMOV, M. G. BLAMIRE, J. L. MACMANUS-DRISCOLL. (2005). Greatly reduced leakage current and conduction mechanism in aliovalent-ion-doped $BiFeO_3$. *Appl. Phys. Lett.* **86**(6), pp.062903-1.

Chapter 9

Appendices

9.1. Summary Tables

The tables below summarize the phases present, lattice parameters and film orientation of each deposited film discussed throughout this thesis as a function of film thickness, substrate orientation, and $xBiFeO_3$ – $(1-x)PbTiO_3$ film compositions.

9.1.1. Effect of Film Composition and Thickness

Table 9.1. compares two different $BiFeO_3$ – $PbTiO_3$ film compositions over a range of film thicknesses to summarize the effect on lattice parameters, phases present and film orientation.

Table. 9.1. The lattice parameters, phase and film orientation of $0.6BiFeO_3 – 0.4PbTiO_3$ and $0.7BiFeO_3 – 0.3PbTiO_3$ films on preferentially orientated platinum substrates as a function of film thickness.

		Tetragonal		Rhombohedral		
	Film Thickness (nm)	**a-axis (Å)**	**c-axis (Å)**	**a-axis (Å)**	**Phase**	**Film Orientation**
$0.6BiFeO_3 – 0.4PbTiO_3$	110	4.14	4.50	-	Polycrystalline / Tetragonal	preferentially (001)
	150	4.15	4.54	-	Polycrystalline / Tetragonal	preferentially (001)
	460	4.13	4.55	-	Polycrystalline / Tetragonal	preferentially (001)
	620	4.13	4.53	-	Polycrystalline / Tetragonal	preferentially (001)
	1360	4.13	4.53	-	Polycrystalline / Tetragonal	preferentially (001)
$0.7BiFeO_3 – 0.3PbTiO_3$	110	3.94	4.50	4.03	Polycrystalline / Tetragonal & Rhombohedral	preferentially $(001)_T$ and $(001)_R$
	150	3.93	4.13	4.03	Polycrystalline / Tetragonal & Rhombohedral	preferentially $(001)_T$ and $(001)_R$
	290	3.93	4.14	4.02	Polycrystalline / Tetragonal & Rhombohedral	preferentially $(001)_T$ and $(001)_R$
	460	3.93	4.14	4.02	Polycrystalline / Tetragonal & Rhombohedral	preferentially $(001)_T$ and $(001)_R$
	620	3.90	4.11	4.00	Polycrystalline / Tetragonal & Rhombohedral	preferentially $(001)_T$ and $(001)_R$
	1120	3.93	4.10	4.02	Polycrystalline / Tetragonal & Rhombohedral	preferentially $(001)_T$ and $(001)_R$
	1360	3.94	4.12	4.02	Polycrystalline / Tetragonal & Rhombohedral	preferentially $(001)_T$ and $(001)_R$

Increasing $(001)_T$ orientation

Increasing $(001)_T$ and $(001)_R$ film orientation

NOTE: When T or R are written as subscript they represent: T = tetragonal unit cell structure and R = rhombohedral unit cell structure.

9.1.2. Effect of Substrate Orientation

Table 9.2 summarizes the effect on lattice parameters, phases present and film orientation for films with $0.7BiFeO_3 – 0.3PbTiO_3$ composition on (111) orientated platinum substrates. This can be compared to Table. 9.1with the only variable between the two being the substrate orientation.

Table. 9.2. The lattice parameters, phase and film orientation of $0.7BiFeO_3 – 0.3PbTiO_3$ films on (111) orientated platinum substrates as a function of film thickness.

		Tetragonal		Rhombohedral		
	Film Thickness (nm)	**a-axis (Á)**	**c-axis (Á)**	**a-axis (Á)**	**Phase**	**Film Orientation**
$0.7BiFeO_3 – 0.3PbTiO_3$	110	3.93	4.56	-	Polycrystalline / Tetragonal & secondary phase	Preferentially (111)
	150	3.93	4.56	-	Polycrystalline / Tetragonal & secondary phase	Preferentially (111)
	290	3.93	4.55	-	Polycrystalline / Tetragonal & secondary phase	Preferentially (111)
	460	3.99	4.55	-	Polycrystalline / Tetragonal & secondary phase	Preferentially (111)
	620	3.93	4.51	-	Polycrystalline / Tetragonal & secondary phase	Polycrystalline
	1120	3.93	4.52	-	Polycrystalline / Tetragonal & secondary phase	Polycrystalline
	1360	3.93	4.55	-	Polycrystalline / Tetragonal & secondary phase	Polycrystalline

Increasing (111) film orientation

9.1.3. Effect of Post Anneal Deposition Temperature

Table. 9.3. The phase and film orientation of $0.7BiFeO_3 – 0.3PbTiO_3$ films on preferentially orientated platinum substrates as a function of post deposition anneal temperature.

Post Anneal Temperature (°C)	**Phase**	**Film Orientation**
500	Tetragonal	Polycrystalline / preferentially $\{100\}_T$ orientated
550	Tetragonal	Polycrystalline / preferentially $\{100\}_T$ orientated
600	Tetragonal & Rhombohedral	Polycrystalline / preferentially $\{100\}_T$ and $(100)_R$ orientated
650	Tetragonal & Rhombohedral with secondary phase	Polycrystalline / preferentially $\{100\}_T$ and $(100)_R$ orientated
700	Tetragonal & Rhombohedral with secondary phase	Polycrystalline / preferentially $\{100\}_T$ and $(100)_R$ orientated